UNIVERSITÀ DEGLI STUDI DI MILANO BICOCCA

SCUOLA DI DOTTORATO
UNIVERSITÀ DEGLI STUDI DI MILANO-BICOCCA

Department of Materials Science

PhD program in Materials Science and Nanotechnology
Cycle XXXIII

Bandgap and Intrinsic Electric Field Engineering in Nitrides: Towards Efficient Red LEDs

Stefano VICHI

Registration number: 761785

Supervisor: Prof. Stefano SANGUINETTI

Coordinator: Prof. Marco BERNASCONI

ACADEMIC YEAR 2020-2021

"Human progress has always been driven
by a sense of adventure and unconventional thinking"
Andre Geim

Contents

Introduction **1**

1 Properties of Nitrides Semiconductors **3**
1.1 Nitrides Structure 3
1.2 Substrates for GaN Epitaxy 6
1.3 Photoluminescence Properties of GaN 7
1.4 InGaN-based Light Emitting Diode 8
1.5 Quantum Wells 10
1.6 QCSE 11
1.7 Green Gap 13
1.8 AlGaN Capping Layer 14

2 Growth Techniques **17**
2.1 Metalorganic Vapour-Phase Epitaxy 17
2.1.1 MOVPE Setup 17
2.1.2 Metalorganic Precursors and Carrier Gases 20
2.1.3 MOVPE Growth of InGaN 23
2.2 Molecular Beam Epitaxy 26
2.2.1 MBE Setup 26
2.3 MBE Growth Kinetics 30
2.4 MBE Growth of GaN 31

3 Characterization Techniques **35**
3.1 Reflection High-Energy Electron Diffraction 35
3.2 Reflectance 35
3.3 Transmission Electron Microscopy 37
3.4 Atomic Force Micrscopy 37
3.5 Photoluminescence 38
3.6 X-Ray Diffraction 41
3.7 Simulations 45

4 MOVPE Growth Optimization **51**
4.1 GaN on Sapphire Template Growth 51
4.2 Growth of the Quantum Structures 52
4.2.1 InGaN Quantum Well Optimization 54
4.2.2 AlGaN Capping Layer and GaN Barrier Optimization 59
4.2.3 Is it Red? 64

5 MBE Growth Optimization **67**
5.1 GaN Buffer Layer Optimization 67

6 Simulations **73**
6.1 AlGaN composition change 75
6.2 AlGaN thickness change 79

7 Results and Discussion **85**
7.1 Intensity analysis 85
7.2 Power and temperature analysis 90

8 Conclusions and Future Prospects **93**

Introduction

At present times, the world's attention on energy saving technologies is continuously rising due to the increased awareness of the negative impact of our lifestyle on the planet. Lighting is one of the most important aspects which falls within this framework. In 2017 the U.S. Department of Energy reported a consumption of approximately 1.7 PWh for lighting. A fairly small part of this amount (approximately 19%) comes from light emitting diodes (LEDs), a novel solid state lighting source with a much higher energy efficiency than traditional sources. Based on the estimations, the energy saved thanks to LED usage is about 0.3 PWh (i.e. 15% reduction in total consumption) despite the limited diffusion. LEDs have already overcome traditional sources in every aspect (energy saving, lifetime, versatility, color quality) and also pricing is becoming more competitive. Due to these advantages, LEDs are expected to grow and become the leading technology with 84% of all unit installations by 2035. This would lead to cumulative energy savings between 18 PWh and 23 PWh (roughly corresponding to $ 890 billion) from 2017 to 2035.

The basis for modern LEDs was put in 1993 when the Nobel prize awarded Hiroshi Amano, Isamu Akasaki and Shuji Nakamura demonstrated the first high-brightness blue LED based on Mg doped GaN. White light was then obtained by using phosphors able to convert blue light into a broad yellow emission, which combined with the remaining blue portion is perceived as white light by the human eye. Even nowadays, phosphor-based LEDs are the most efficient sources for general lighting and their use is rapidly increasing. Another field that is being revolutionized by the use of LEDs is the market of displays. High-resolution displays require a small pixel size and a fast response. On top of that, RGB emitters are needed in order to reproduce the visible gamut. Nowadays, the vast majority of commercial displays are liquid crystal displays (LCD) in which the white backlight is produced by phosphor covered blue LEDs. Red and green color are then obtained by colored layers, while blue comes from the GaN-based LED emission. However, since the emitted light has a strong yellow component, pure red and green can not be obtained and as a consequence the resulting color gamut is reduced. More recent solutions are based on the use of individual RGB LEDs. In this case, blue and green light are emitted by GaN or InGaN based LEDs while red LEDs are made of AlInGaP. This permits to reduce power consumption and to increase color accuracy. However, the possibility to scale down the size of these pixels is hindered by the large carrier diffusion length in phosphide materials ($\sim$ 100 times larger compared to GaN [1]), which limits the minimum size of each pixel to hundreds of μm. As an example, this means that the minimum size for an 8K LED monitor (7680 x 4320 pixels) is $\sim$ 52". It is clear that the scalability limit of this technology has been reached and a new technology is required to obtain small size and high definition displays (e.g. mobile display, virtual reality headset).

The future of display technology has been identified in micro LEDs (μLEDs), which promise a reduction in pixel size of two orders of magnitude. Other significant advantages are the increase in brightness, lifetime and response time, a substantial reduction in produc-

tion costs and the possibility to scale the size of a display with no difference in production cost. One of the most important materials suitable for this application are InGaN alloys, which can emit in the whole visible spectrum. This allows for a monolithic integration of ultra small blue, green and red pixels, a key feature required for micro LEDs. At present times there are still some limits which have to be overcome to make this possible and one of them is the low quantum efficiency of red InGaN LEDs [2, 3]. Many researchers are trying to overcome this obstacle and one of the most promising approaches to mitigate this problem is to use an AlGaN capping layer on top of the commonly used InGaN quantum wells [4, 5].

The aim of this work is to improve the understanding of the AlGaN capping layer and its effects on emission properties and to obtain a sample with red emission. In order to do this, I have studied the influence of various growth parameters on the emission properties (i.e. peak wavelength, emission line width and intensity) and optimized them to obtain a long-wavelength emission. Moreover, using theoretical simulations I have studied the effect of AlGaN thickness and composition on emission wavelength and recombination probability. Based on these results, I proposed a new explanation on the effectiveness of the AlGaN capping layer.

This thesis work is organized as follows. The first chapter contains a general introduction on the properties of nitrides semiconductors, in particular of (Al,In,Ga)N alloys. The following discussion is centered on the substrates typically used for the growth of GaN and its luminescence properties. Next, InGaN quantum wells are introduced and their properties are discussed. Lastly, the low efficiency at long wavelengths and some state-of-the-art approaches to mitigate this problem are discussed. In the second chapter there is an in depth discussion on the growth techniques used in this work. A brief introduction of the setup is followed by a discussion on the growth and the processes involved. The third chapter consists of the description of the characterization techniques used in this work. In the fourth chapter is shown the optimization process of the MOVPE growth done to obtain a sample with red emission. The chapter is then concluded by a discussion on the perceived color of the best sample obtained. In the fifth chapter is reported the MBE growth optimization to obtain a smooth buffer layer required for the subsequent growth of quantum wells. The sixth chapter contains the discussion on the simulations performed on GaN/InGaN/GaN and GaN/InGaN/AlGaN QWs. The effect of capping thickness and aluminum content on the emission properties are discussed. In the seventh chapter are shown further experimental results on the best sample obtained and these results are combined with the simulations to give an explanation of the effects on the emission properties of the AlGaN capping layer. Finally, in the last chapter a brief discussion on the future prospects of this research is presented.

1

Properties of Nitrides Semiconductors

1.1 Nitrides Structure

Nitrides are a class of III-V materials where a group three metal (i.e. B, Al, Ga, In) is bound to nitrogen with a mixed ionic-covalent bond. The most stable crystal structure under typical growth conditions is the wurtzite (WZ), however also the zincblende (ZB) structure can be obtained with proper conditions. The wurtzite structure, shown in the top-left part of figure 1.1, is made of two hexagonal closed packed sublattices shifted by 5/8 of the cell height along the [0001] direction with a stacking order AaBb. The unit cell is hexagonal and it is characterized by two lattice parameters, the basal plane lattice parameter a and the axial lattice parameter c. It is usually given also the nearest neighbor distance (u) divided by the lattice parameter c, which in an ideal wurtzite structure is 0.375. In table 1.1 are reported the experimental lattice parameters of wurtzite GaN, AlN and InN obtained from powder diffraction [6–8].

	GaN	AlN	InN
a (Å)	3.1893	3.1130	3.538
c (Å)	5.1851	4.9816	5.703
u	0.377	0.382	0.379

Table 1.1: Measured lattice parameters of wurtzite GaN, AlN and InN [6–8].

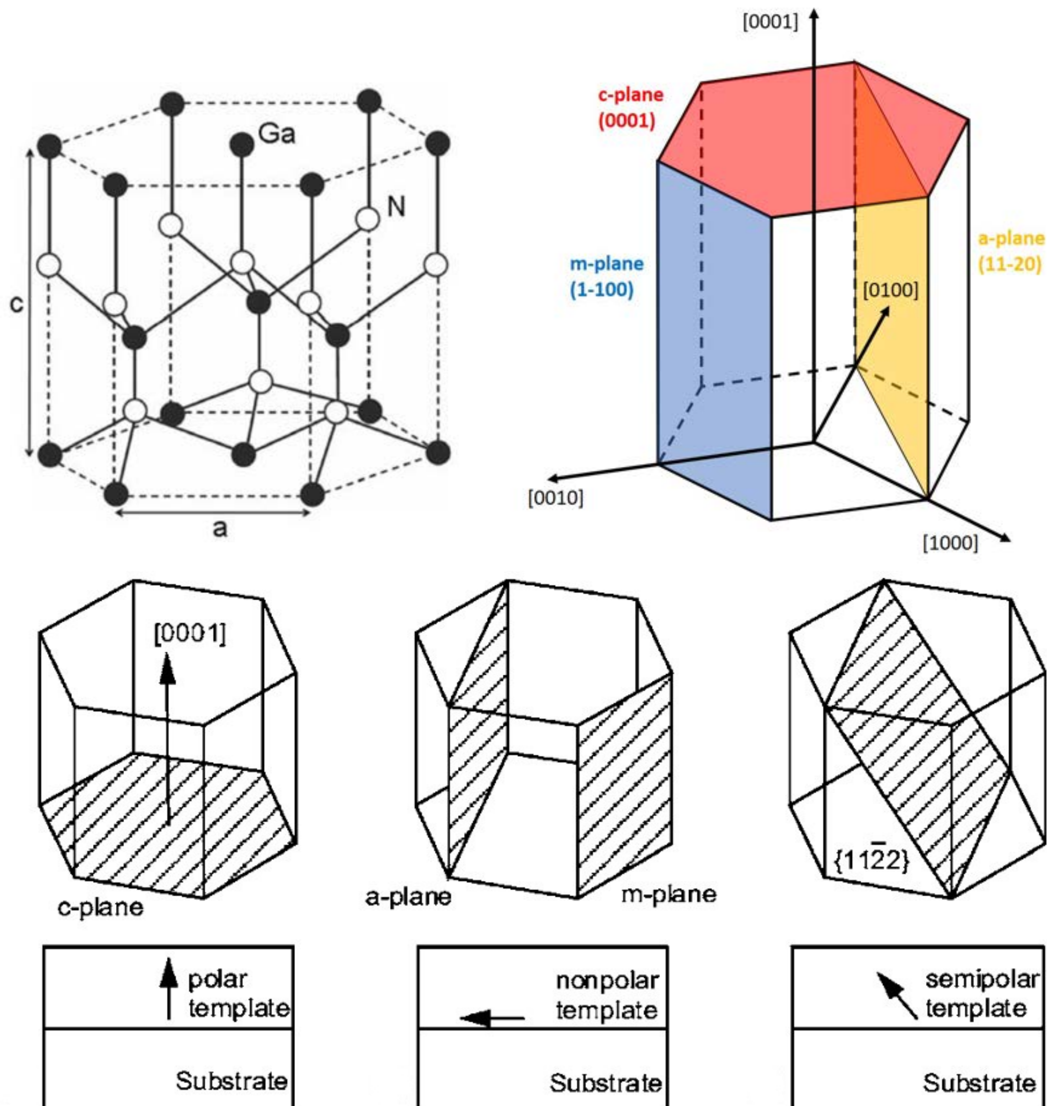

Figure 1.1: Top-left) Wurtzite crystal of GaN where are shown the lattice parameters a and c. Gallium and nitrogen atoms are represented as black and white dots respectively. (Top-right) Schematic representation of c-, a- and m-planes. (Bottom) Schematics of the spontaneous polarization field along the growth direction depending on the crystal orientation. From [9].

The lack of an inversion symmetry-plane perpendicular to the vertical direction implies that III-Ns have a polar axis which can have a metal polarity ((0001) or +c) or nitrogen polarity ((000$\bar{1}$) or -c) depending on the terminating atoms. The symmetry of the crystal structure is affected by its orientation, which in turn affects the polarization properties, as shown by Romanov et al. [9]. The dependency of the polarization field on the inclination angle with respect to the c-direction has attracted the interest of researchers on less conventional crystal planes, thanks to the possibility to engineer the electric field of the structure. The typical crystal planes of interest, which are shown in the top-right and bottom panels of figure 1.1, are the polar c-plane (0001), the non polar a-plane (11$\bar{2}$0) and m-plane (1$\bar{1}$00) and various semi-polar planes. Currently, the most used crystal orientation for III-N opto-

electronic devices is the c-plane, thanks to better performance and higher growth quality as well as a more established knowledge.

Nitride semiconductors are particularly interesting for optical applications since they have all a direct gap and by alloying them it can be changed from UV (AlN, E_g=6.25 eV at 0 K, and GaN, E_g=3.51 eV at 0 K) to IR (InN, E_g=0.78 eV at 0 K), as can be seen from figure 1.2. Interestingly, for long time the exact band gap of InN was unknown. Indeed, before early 2000 several experiments resulted in an estimation of the room temperature InN band gap of ∼1.9 eV, which is much different from the ∼0.7 eV reported now [10]. This misleading result was caused by the Moss-Burstein effect. This effect consists of the shift of the absorption edge towards higher energies when the lower energy states are already populated, making the transitions to those states inaccessible. In case of InN, a large background oxygen doping was present due to the poor growth process, which resulted in an extremely large occupation of CB states due to the favored n-type behavior of impurities [11]. Moreover, at the surface of InN there is an electron accumulation layer due to the Fermi level positioned below the conduction band [12]. The low growth quality resulted in a grained morphology with a large surface area, resulting in an extremely large free-electron density. Since the energy gap was extracted from the absorption edge, the apparent value was largely overestimated. However, when the quality of the InN growth process increased with a decrease in unintentional doping and a smoothening of the surface, the measured band gap decreased from ∼1.9 eV to ∼0.7 eV [13]. After the true band gap of InN was discovered, it became clear the potential application of InGaN as a red, green and blue emitter depending on its composition. Also the AlGaN alloys are interesting for optical applications, as they can emit in the UVA (400-315 nm), UVB (315-280 nm) and UVC (280-100 nm) spectral ranges.

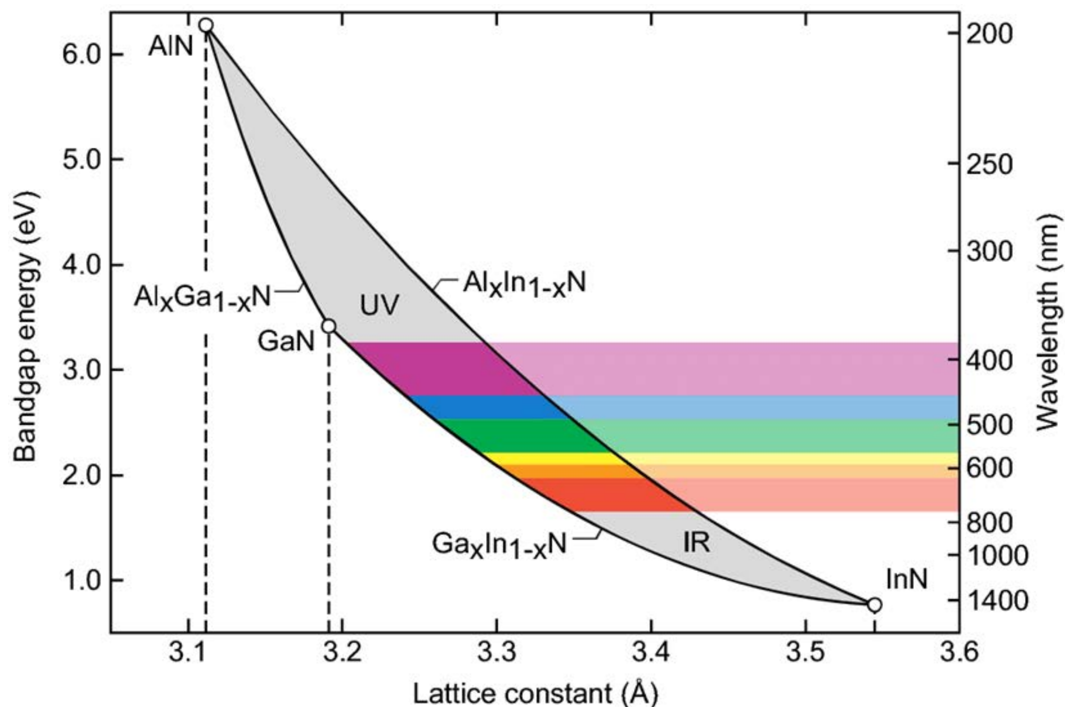

Figure 1.2: Energy gap and lattice constant of GaN, AlN, InN and their alloys.

1.2 Substrates for GaN Epitaxy

One critical aspect regarding the growth of III-Ns is the choice of the substrate. As can be seen from table 1.1 the in-plane lattice constant of GaN is 3.1893 Å, which is not matched with any conventional substrate. The lack of a low-cost native substrate forces to grow nitrides on lattice mismatched substrates. The most used of which are Si(111), sapphire, 4H-SiC and 6H-SiC, which have an in plane lattice parameter of 3.828 Å, 4.758 Å, 3.073 Å and 3.0817 Å respectively. The large lattice mismatch results primarily in a high threading dislocation density (typically from 10^8 to 10^{10} cm^{-2}) which deteriorates the optical and electrical properties of the grown layers. Nevertheless, the most used substrate for InGaN LEDs is the c-plane sapphire. The calculated lattice mismatch between GaN and sapphire is 33%, which is by far the largest mismatch of the list. However, the crystal structure of sapphire (Al_2O_3) is made of oxygen ions in an hexagonal close package arrangement and aluminum ions which occupy the octahedral sites. The outer plane of O atoms are inclined by 30° with respect to the basal plane, resulting in an effective lattice parameter of $a_{sapph}/\sqrt{3}$. This reduces the lattice mismatch from 33% to 16%, which however is still extremely high. This however results in coincident lattices, where six times the bond length of GaN correspond to seven times the bond length of sapphire. Despite the large mismatch, a high emission efficiency was obtained for InGaN-based blue LEDs grown on sapphire despite a TTD of 10^9 cm^{-2}. The explanation for this unexpected results is still debated in literature. However, most of the proposed interpretations are based on a screening mechanism of indium which prevents carrier from reaching dislocations [14–16]. The large polarization field due to strain or alloy nonuniformities acts as a sort of barrier, preventing carriers to reach the dislocations where they would recombine non-radiatively. As a result, the luminescence efficiency of InGaN-based LEDs is almost insensitive to TDD in the 10^6 to mid 10^8 cm^{-2} range.

The challenges of growing a high quality material on a substrate with such large lattice mismatch prevented the widespread of nitrides semiconductors until the late 1980s. In 1986 Amano et al. [17] successfully grown a crack free GaN layer on top of sapphire using a thin ($\sim$ 50 nm) AlN buffer layer grown at low temperatures (LT). This approach was followed by Nakamura who obtained similar results using a LT-GaN buffer layer instead of AlN [18]. This growth procedure, known as the "nucleation layer", opened the path for the development of GaN-based optoelectronic devices on sapphire substrates and is currently employed to obtain high quality GaN layers. More into details, this technique is based on a three step growth under different conditions, as schematically shown in the left panel of figure 1.3. The initial layer is grown at low temperature ($\sim$ 500 °C) and has a very poor crystal quality as it is made of a high density of small crystals with different orientations and crystal structures and even amorphous structures. Indeed, the adatoms on the surface have a very low surface diffusion length due to the low temperature, nucleating close to the impinging site. As a result, there is a low chance for the adatoms to reach an ideal nucleation site with the consequent poor crystal quality and low homogeneity. However, this step allows the GaN grains to adapt to the sapphire substrate and form the coincidence lattice. Without this, the strain in the structure would be so large that it will crack the sample after few layers. The second step consists of a selection of the most stable crystal structure after a thermal annealing. In this step, the growth is interrupted and the temperature is increased up to the growth temperature ($\sim$ 1000 °C) without supplying any material. During

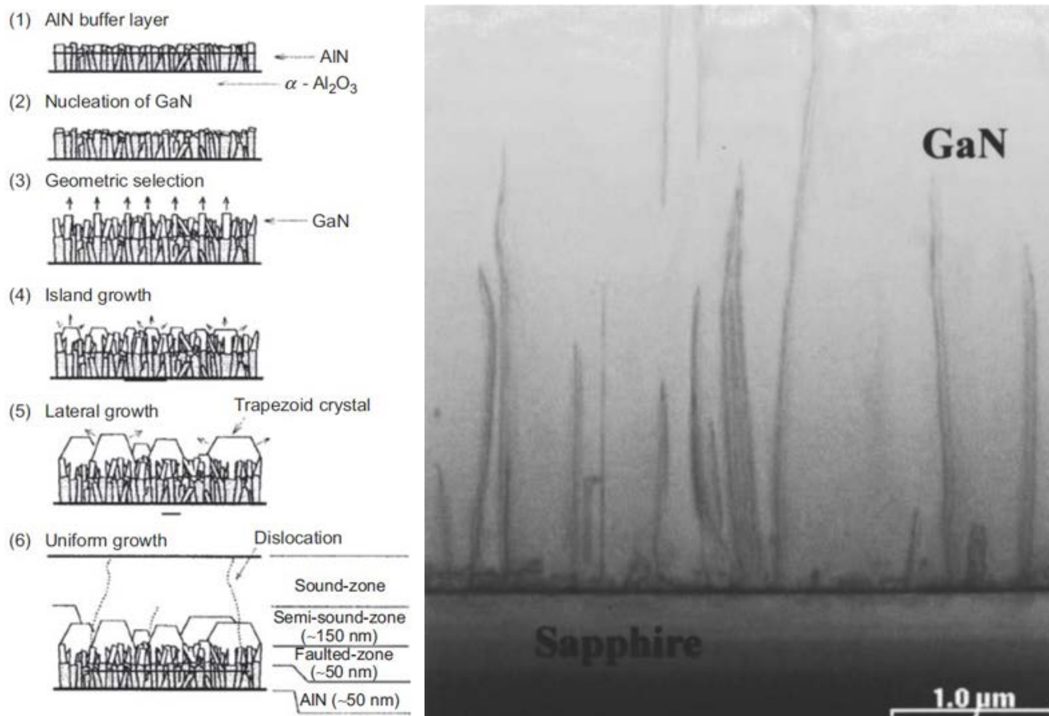

Figure 1.3: (Left) Schematics of the growth steps of GaN on sapphire using an LT nucleation layer. From [20] (Right) TEM image of a typical GaN on sapphire template grown using a LT-GaN nucleation layer. From [21].

this period, the metastable structures are converted into (0001) seeds, which are epitaxially related to the substrate. Finally, the HT-GaN is grown. Initially, the growth starts on the seeds of the nucleation layer and proceeds by forming trapezoidal island oriented along the c direction. The lateral overgrowth of these structures is favored and these island coalesce into a compact layer [19]. Although the interface between the LT-buffer and the HT-GaN is very defective, as can be seen in the right panel of figure 1.3, the overgrown layer has a high crystal quality.

1.3 Photoluminescence Properties of GaN

During the growth of epitaxial layers point defects are introduced in the lattice as a consequence of the growth process. These defects are typically recombination centers which can be radiative or non-radiative, depending on whether the process involves the emission of a photon or not. Even if these defects do not effect the morphological properties, they have an impact on the electrical and optical properties of the device. Therefore, studying the presence of these defects can give important information on the quality of the sample. In case of GaN, many important defects are radiative, therefore they can be easily studied with luminescence experiments. The two most important defects-related luminescence bands in undoped GaN, reported by Reshchikov et al. [22], are the blue (BL) and the yellow (YL) luminescence bands. In figure 1.4 are shown the temperature dependencies of the BL, YL and exciton band emission [23].

Despite being present in most of the GaN samples, the origin of the yellow luminescence band is still debated. Typically, the YL is a broad band with its maximum at 2.20-2.25 eV and a line width of 350-450 meV. Based on ab-initio calculations [24], the transition energy is compatible with several gallium vacancies (V_{Ga}), as confirmed also by some experimental results [25]. As initially found by Ogino et al [26] and confirmed by others, carbon is most probably the impurity that binds with the V_{Ga} to form the complex responsible for this transition. However, the exact mechanism of the transition and whether it originates from surface or bulk defects is still unclear and debated [22]. As can be seen from figure 1.4, the yellow luminescence does not quench at room temperature, which means that the defects involved in the transition are probably deep states. The increase of quantum efficiency observed between 200 and 260 K is related to the quenching of the blue luminescence. Indeed, due to the high thermal energy, the carriers trapped in the shallow impurities responsible for the blue luminescence can escape and contribute to the yellow luminescnece and exciton recombination [22].

The other well known GaN luminescence band is the blue luminescence, peaking at 2.9 eV. It is typically observed in undoped, Zn doped and Mg doped GaN. In the following discussion it will be described only the blue luminescence in undoped GaN, as it is more strictly related to this thesis work. This broad band is due to a transition from the conduction band or a shallow donor (depending on the temperature) to a deep acceptor with an activation energy of 0.34-0.4 eV [22]. The impurities involved in the transition are thought to be a $V_{Ga}O_N$ complex [23, 27]. The temperature dependence of the quantum efficiency is shown in figure 1.4. As can be seen, at low temperature is the most intense transition. However, above 200 K it quenches rapidly and at 300 K its intensity is almost two orders of magnitude lower than the yellow luminescence but still larger than the exciton recombination.

Since the typical operation temperature of LEDs is 300 K, the effect of the yellow luminescence on the emission properties is more severe compared to the blue luminescence. Therefore, it is necessary to carefully optimize the growth conditions in order to avoid carbon contamination as much as possible.

1.4 InGaN-based Light Emitting Diode

A light emitting diode is a device made of an n-p junction in which most of the injected carriers recombine radiatively, emitting photons. In these devices the built-in electric field creates a depletion region in the central part of the device. When the junction is forward biased (i.e. positive voltage applied to the p-side), the built-in potential is lowered and carriers are injected in the depletion region and the current flows through the device. As a consequence, free electrons and holes locate in the same spatial region and recombine. The recombination process may occur by emitting a photon (radiative recombination), by emitting a phonon (non radiative recombination) or with more complicated mechanism involving multiple particles. The energy of the emitted radiation corresponds in first approximation to the energy gap of the material in which the radiative recombination takes place.

Even if GaN was known since early 1960s [28, 29], the development of the first nitride-based devices required three decades. At that time, researchers were struggling to obtain p-type doping due to the passivation properties of hydrogen. During the growth, the hydrogen atoms in the atmosphere immediately bind to the Mg atoms, passivating the missing bond and inhibiting the acceptor behavior. This obstacle was first overcome by Akasaki

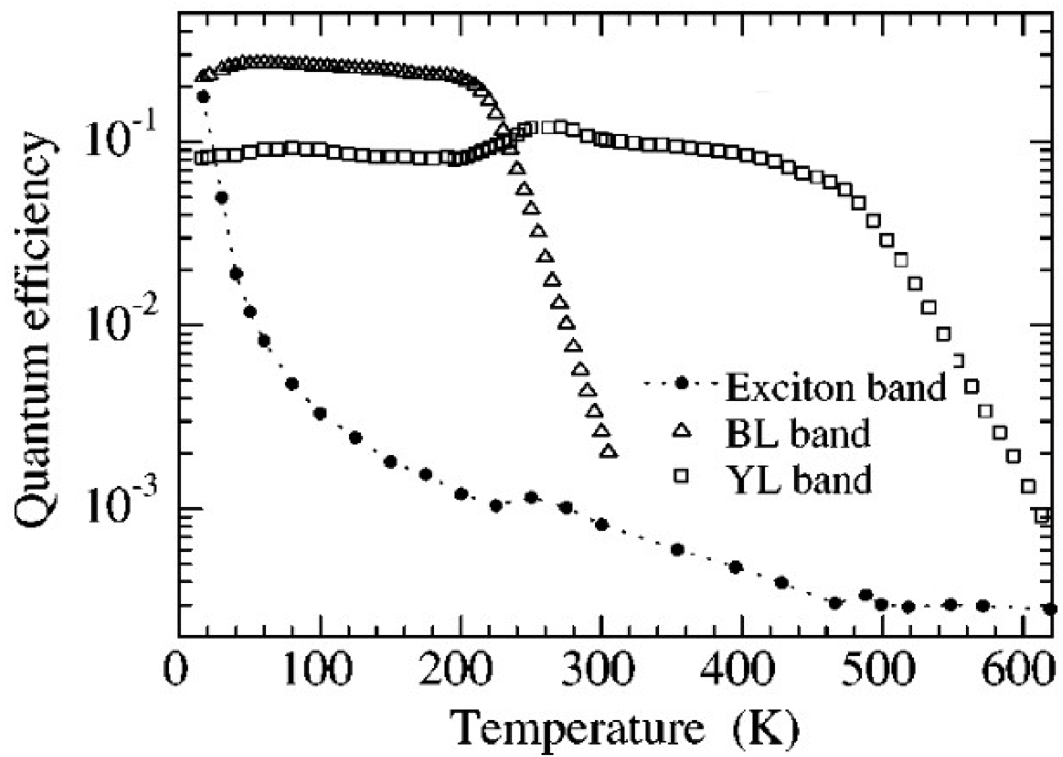

Figure 1.4: Quantum efficiency of the blue luminescence (BL), yellow luminescence (YL) and exciton band as a function of temperature. From [23].

and Amano who achieved the p-type conductivity by using low-energy electron beam irradiation on Mg doped GaN, achieving blue luminescence from a GaN p-n junction [30]. The same result was then obtained by Nakamura using a thermal annealing instead of the electron irradiation [31, 32]. These post-growth techniques were able to break the Mg-H bond, restoring the acceptor-like behavior of magnesium. These results finally opened the path for GaN-based optoelectronic devices.

However, it is immediately clear that in order to have a high recombination efficiency a large density of both carriers is required in the region where the recombination takes place. As a consequence, optical recombination in bulk materials is not particularly efficient, since the carriers flow through the entire volume without accumulating in the active region. Therefore, to improve the recombination efficiency, modern LEDs make use of nanostructures such as quantum dots (QDs) or quantum wells (QWs) placed in the active region. These structures are made of a lower gap material which is included in a higher gap barrier, forming a type I heterostructure (see section 1.5), as shown in figure 1.5. From the figure it is visually clear that this type of structures permits to have a high density of carriers in a narrow region, thus increasing recombination probability. In particular QWs are currently used in commercial LEDs due to their simpler growth process and larger uniformity compared to QDs, which results in better device properties.

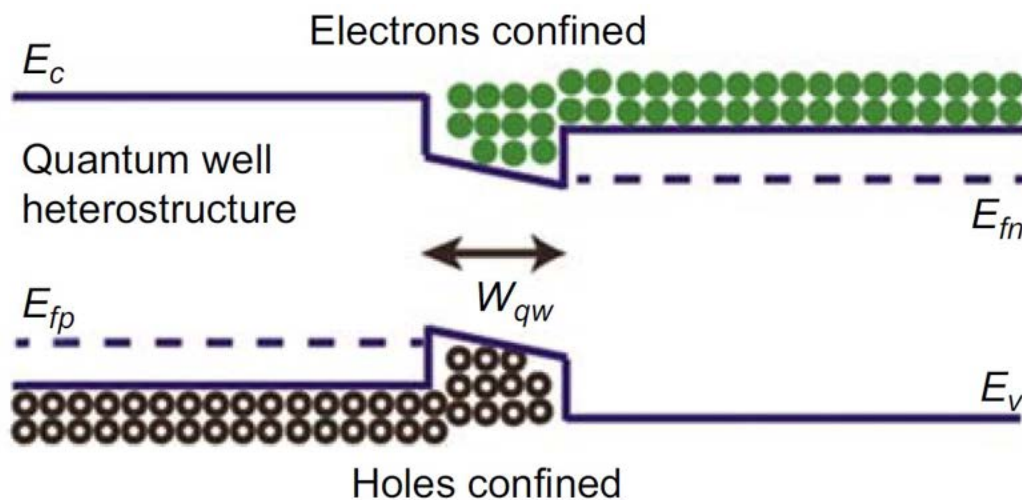

Figure 1.5: Schematics of a type I heterostructure. From [20]

1.5 Quantum Wells

In this section, a general and qualitative overview on quantum wells properties is given. An accurate and in depth discussion on the mathematical approach to the computation of confined states in QWs will be given in section 3.7

As discussed above, in order to improve recombination efficiency commercial LEDs make use of nanostructures and in particular of quantum wells. A quantum well is formed when in a single direction a sufficiently thin material with a lower band gap is included in a different one with a larger band gap, resulting in a potential well in both the conduction and the valence band. This particular band alignment is called type I heterostructure. In

order to have quantum confinement, the size of the potential well must be of the order of nanometers. To have the confining potential well for both carriers, the energy bands of the two materials need to be properly aligned with respect to the vacuum level. This value is defined as the energy of a free stationary electron outside the material and it is typically used to compute the band alignment in an heterojunction. If this type of confinement is achieved in two directions, the nanostructure is called quantum wire and if the confinement is present in three directions it is called quantum dot. Since the state of the art technology is based on QWs, the following discussion will be focused only on this type of nanostructures.

The materials used to form the heterostructures for nitrides-based visible LEDs are GaN and InGaN. GaN is typically used as the barrier material with its large room temperature band gap of 3.42 eV in which InGaN, with its lower band gap, is sandwiched to form the type I heterostructure. Since the energy gap of InGaN can be modified by changing the indium composition (see figure 1.2), this will also affect the potential barrier of the heterostructure. The possibility to control the energy properties of the nanostructure by changing both thickness and composition of the InGaN QW make these materials very versatile and appealing for visible lighting sources. From a theoretical point of view, the change of material (and energy gap) of an heterostructure breaks the symmetry of the perfect crystal and introduces a perturbation in the crystal potential. As a result, the Bloch waves do not represent the correct eigenfunctions of the new heterostructure Hamiltonian and therefore the energy levels are different from the continuum states. The consequence is that only particular states in the quantum well are allowed, which are called confined states. In a simplified model (e.g. infinite potential well), these states corresponds to the stationary waves which can be formed in the QW. In this particular case, the energy of these states is proportional to L^{-2}, where L is the thickness of the QW. It is clear that changing the thickness of the quantum well (the InGaN region in this specific case) has profound effects on the allowed energies. In particular, the larger is the QW the lower is the energy of the confined states. In the limit of an infinite thick QW, the confined states coincide with the continuum states of the bulk material. It is important to understand which is the maximum size at which quantum properties start to arise. The reference length is the electron de Broglie wavelength in the material, which is typically of the order of 10 nm. In order to exhibit quantum properties, the size of the heterojunction must be lower than this value.

1.6 Polarization Field and Quantum Confined Stark Effect

However, not only structural properties affect the confined states but also other perturbations such as the electric potential do modify the QW Hamiltonian. As introduced before, the most stable nitrides crystal structure is the wurtzite. Due to the lack of inversion symmetry perpendicular to the (0001) direction, this structure is characterized by a spontaneous polarization field. Moreover, another type of polarization field (piezoelectric) is present in strained materials. This originates from the asymmetrical stretching of atomic bonds under elastic forces, which results in the formation of electric dipoles due to the unbalanced charges. The combination of these effects give rise to an electric field which can be of the order of several MV/cm in GaN/InGaN/GaN QWs. In this case, the piezoelectric component is the dominant contribution to the electric field. More details on the mathematical description of polarization field can be found in section 3.7. However, for the following discussion it is sufficient to remember that in nitrides semiconductors (and in specific in

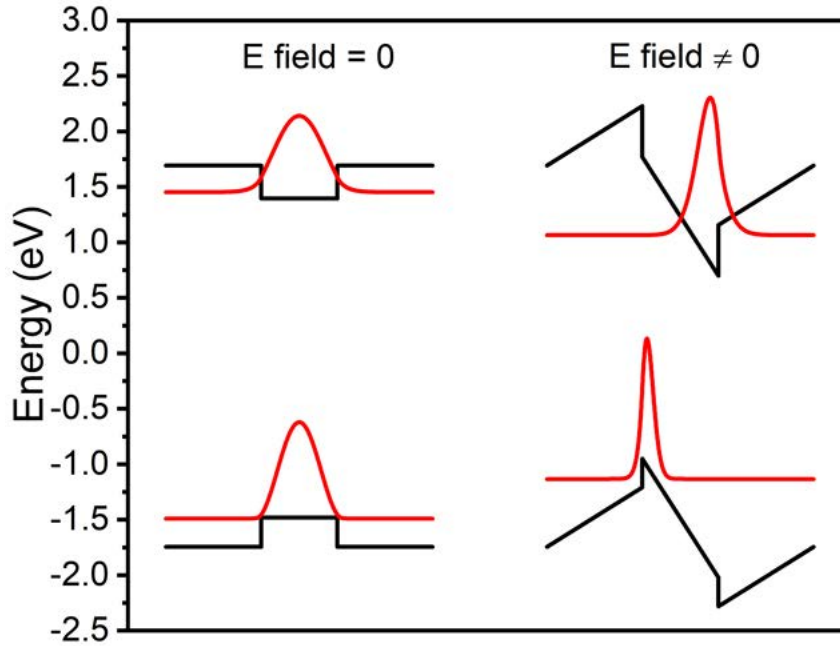

Figure 1.6: Comparison between GaN/InGaN/GaN QW with and without electric field to show its effect on the quantum properties of nanostructures.

GaN/InGaN/GaN QWs) there is a strong electric field and it has profound effects on the confined states.

The effect of an electric field on the energy bands is to add a linear potential term -eFz to the electronic Hamiltonian, where e is the elementary charge, F is the intensity of the electric field and z is the spatial coordinate along the growth direction. If the electric field intensity is small, this additional term in the Hamiltonian can be computed by using the perturbation theory. To the first order, the change in ground state energy can be written as:

$$\Delta E_{GS}^{(1)} = \langle \psi_1 | V' | \psi_1 \rangle \tag{1.1}$$

Where ψ_1 is the ground state wave function and V' is the perturbing potential -eFz. For a symmetric quantum well, this correction term is zero due to symmetry reasons. In the second-order perturbation theory this correction gives $\Delta E^{(2)} \propto -F^2$, which therefore reduces/increases the energy of the confined state of an electron/hole. The change in the confined energy levels caused by the electric field is known as quantum confined Stark effect (QCSE). The second effect of QCSE is to reduce the wave function overlap. Due to the different polarity of electrons and holes, they react in an opposite way to the electric field. As a result, electrons and holes tend to localize at the opposite interfaces of the QW, decreasing their overlap. The effect of QCSE on the confined states can be seen from figure 1.6 where it is shown the comparison between a GaN/InGaN/GaN QW with and without electric field.

As discussed above, the polarization field can be distinguished into spontaneous and piezoelectric. The major contribution to the total electric field in GaN/InGaN/GaN QWs comes from the second one. Its intensity increases with increasing lattice mismatch between GaN and InGaN (i.e. with increasing indium content). As a result, the influence of QCSE

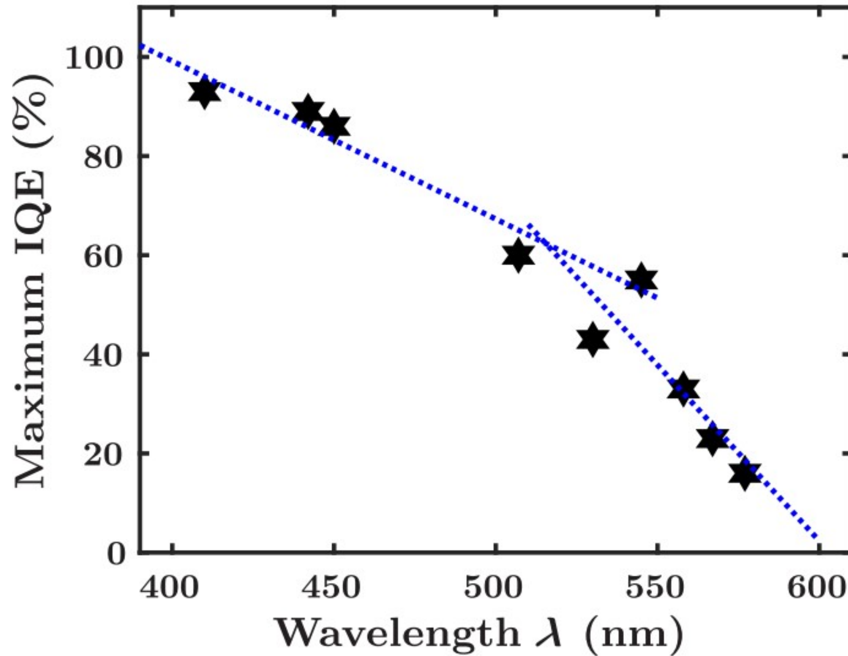

Figure 1.7: Maximum value of IQE as a function of emission wavelength for GaN/InGaN/GaN QWs. From [33]

on the quantum properties of the QWs becomes more relevant for long-wavelength LEDs, where the indium concentration is large.

1.7 Green Gap

As discussed before, one of the most interesting aspects of InGaN is that the emission wavelength can cover all the visible spectrum depending on In composition. However, the emission efficiency is not constant for all the wavelengths. As can be seen from figure 1.7, the internal quantum efficiency (IQE) is close to 100% for short wavelengths and it rapidly decreases when moving toward red. This behavior of the IQE, which is defined as the ratio between the radiative recombination rate and the recombination rate of all the processes, is typically addressed as the green gap of nitrides.

Despite being a well known phenomenon, the origin of this behavior is still unclear. The low efficiency of high-In-content InGaN is attributed to many factors, the most discussed among them being low wave function overlap due to strong piezoelectric fields, localization issues due to alloy fluctuations [34], and the high number of point defects due to low growth temperatures [35]. Both the first and the second explanation are based on the negative effect of the QCSE which separates wave function overlap. On the other hand, the point defects explanation is based on structural problems which are caused by the growth process. Recently, David et al. [36] showed that defect-assisted non-radiative recombination can be a serious candidate for explaining the low recombination efficiency at high indium contents. In this non-radiative process, Auger electrons are scattered to a trap where they recombine by the Shockley-Read-Hall (SRH) process. This explanation leaves point defects as the main suspect for the green gap. Lately, other works highlighted the role of point defects in

the reduction of quantum efficiency [33, 37].

Moreover, recent works of Haller at al. [38, 39] have shown that there might be point defects which are originated from the high-temperature growth of GaN. These defects segregate at the surface and are incorporated only in indium-containing layers. When they incorporate, they bind strongly to indium to form complexes which become non-radiative recombination centers. Although the origin of these defects and incorporation mechanism are still unclear, it was observed that the formation energy is close to the dissociation energy of GaN ($\sim$3.6 eV) [39]. It was proposed that due to the GaN dissociation, N_2 molecules are formed causing a shortage of nitrogen leading to the formation of nitrogen vacancies or divacancies on the growth front [40]. Those vacancies are then incorporated in indium-containing layers due to a decrease in their formation energy in InGaN [41]. Therefore, to mitigate this problem typically an In-containing underlayer is grown before the quantum wells in order to incorporate these defects far from the active layer [38, 42].

It is clear that the high defectivity of InGaN is strongly affecting the performances of long-wavelength LEDs and is one of the major contributors to the green gap. Many effort is put in trying to reduce this problem either by growing on pseudo substrates with reduced lattice mismatch with GaN or by reducing the elastic energy in the system with strain-compensating layers. In particular, very promising results have been achieved by using an AlGaN capping layer on top of the InGaN QWs, which is expected to compensate for the compresssive strain in the QWs. The discussion on this approach and its effects on recombination properties are the main focus of this thesis and will be discussed extensively from the experimental and theoretical point of view.

1.8 AlGaN Capping Layer

The first group to report the use of an AlGaN capping layer was the one of Shioda et al. [4] who in 2012 demonstrated that with this approach it was possible to improve the emission intensity of green LEDs compared to standard GaN/InGaN/GaN LEDs. Later, the same group reported an improved efficiency even at longer wavelengths [2, 43]. By using an AlGaN capping layer instead of GaN, the polarization field in the InGaN QW increases due to the larger interface charge density. Based on the discussion of section 1.6, the increased field results in a larger QCSE which in turn is expected to reduce the transition energy but at the same time also the wave function overlap decreases. However, the reported results clearly show an unexpected increase in recombination efficiency. Although this increase in intensity is known since many years, a unique explanation for the observed phenomenon is still lacking in the literature. One of the more common explanations given in literature is related to the strain compensation effect of AlGaN. As can be seen from figure 1.2, InGaN is compressed when grown pseudomorphic on GaN while AlGaN is tensile strained. Therefore, the total elastic energy stored in a stack of GaN/InGaN/AlGaN is lower compared to the one of GaN/InGaN/GaN structure. The expected result is a reduction in strain-related defects which acts as non-radiative recombination centers. As a consequence, in the GaN/InGaN/AlGaN QW the IQE is expected to be higher compared to the typical GaN/InGaN/GaN QWs. This effect should be noticeable with the increasing number of the stacks, especially when the structure is thick enough that a degradation of the GaN/InGaN/GaN QWs can be observed.

Another explanation is related to the higher growth temperature that can be used while

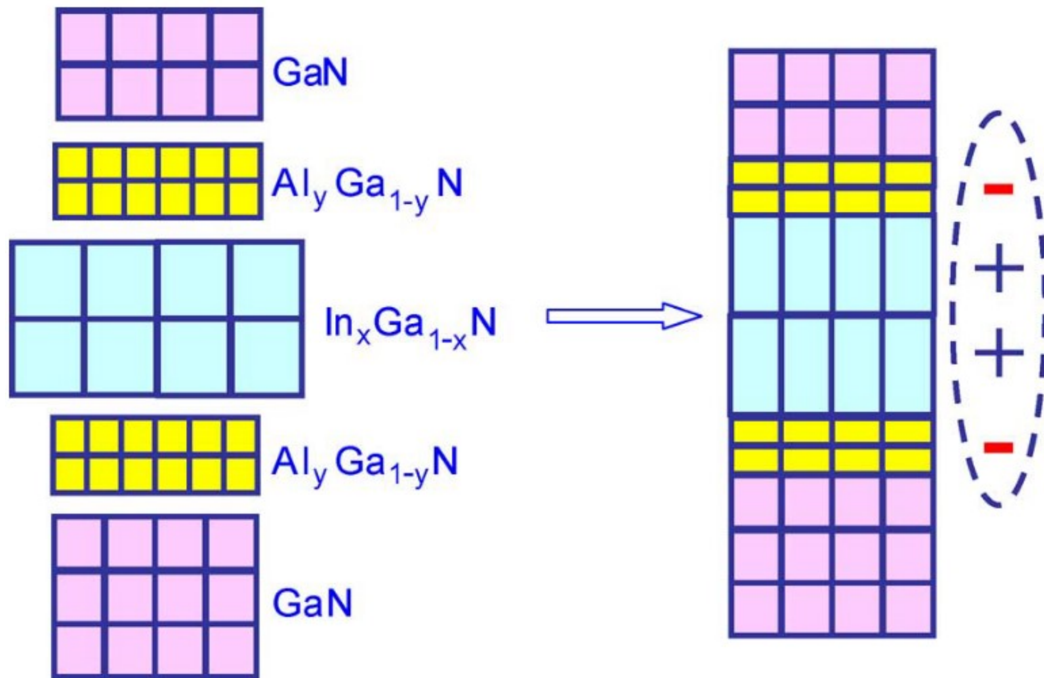

Figure 1.8: Schematics of the strain-compensation effect of the AlGaN capping layer. The compressive strain of InGaN is balanced by the tensile strain of AlGaN, reducing the total elastic energy stored in the material. From [44]

keeping the same emission wavelength. As explained before, the InGaN/AlGaN interface has a larger polarization charge density compared to InGaN/GaN. The larger electric field in the QW increases the QCSE, with a redshift of the emission wavelength. Therefore, even if the InGaN thickness and composition are the same, the GaN/InGaN/AlGaN QW will emit at longer wavelengths compared to the GaN/InGaN/GaN. As a consequence, the same emission wavelength between the two structures can be obtained by reducing the In composition and therefore being able to grow at higher temperatures the GaN/InGaN/AlGaN QW . This results in a reduced point-defects density due to the more favorable growth conditions [35], which in turn permits to have a higher IQE.

2

Growth Techniques

2.1 Metalorganic Vapour-Phase Epitaxy

Metalorganic vapour-phase epitaxy (MOVPE) is a growth technique developed initially for the epitaxy of Gallium-V semiconductors by Manasevit in the 1960s [45]. The high purity achievable, the versatility and suitability for large-scale production of virtually any II/VI and III/V compound have led MOVPE to be one of the most used techniques for the production of LEDs, laser diodes, solar cells and transistors [20]. In the last decades, it has become the leading technique for the growth of high-purity III-nitrides semiconductors, in particular for (Al,In,Ga)N alloys, which are the topic of this work.

2.1.1 MOVPE Setup

Typically, a MOVPE system is made of three parts, the gas mixing system with bubblers and and run/vent valves, the reactor chamber and the exhaust system to handle the dangerous gases originated from the process. The liquid metalorganic (MO) precursors are stored in stainless-steel containers (bubblers) and are delivered to the reactor chamber by ultrapure lines under the laminar flow regime. This is fundamental in order to have an homogeneous and reproducible supply of reactants to the surface. The purpose of the gas mixing system is to deliver a stable partial pressure of reactants to the reactor within 1/10th of a second. This is achieved by a complex arrangement of tubes where the gas flows are diverted without interruptions. This task is done by the switching (run/vent) valves which either bypass the arriving flow directly to the pumps or deliver it to the reactor. The ways in which the precursors are delivered to the reactor have profound effects on the growth dynamics. The most used systems are the horizontal flow (planetary) reactors, the close-coupled showerheads reactors and turbodisc reactors. The setup used in this work is a 3x2” close-coupled showerhead reactor from EpiQuest and I will refer implicitly to this geometry in the following discussions.

In figure 2.1 it is shown the scheme of a typical MOVPE with a gas mixing system, which is similar to the one used in this work. To control the partial pressure of the gases delivered to the reactor one only needs to know the gas flow relative to the total flow and the reactor pressure. However, many of the precursors (especially the metals) are in the liquid phase under typical conditions, making this process more complicated. Indeed, the

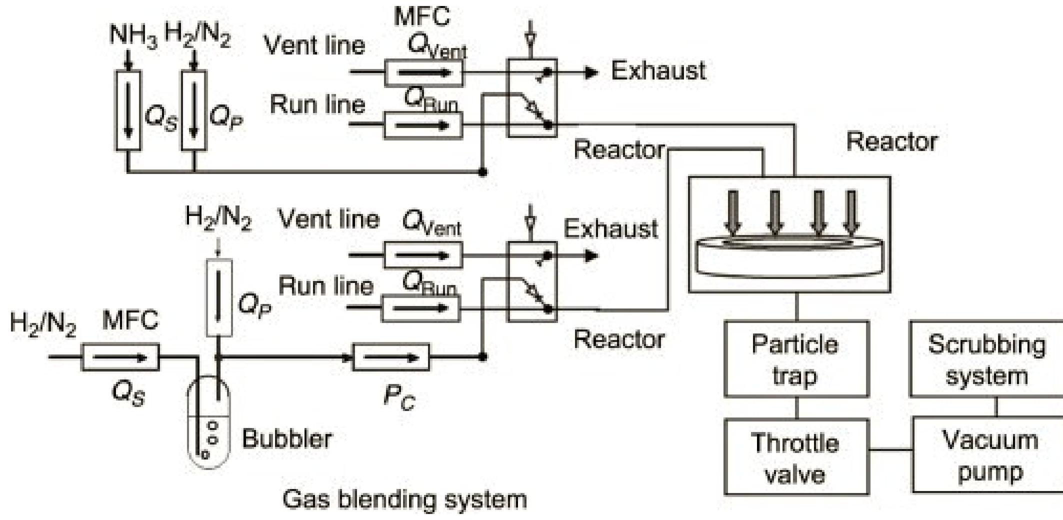

Figure 2.1: Scheme of the flow path in a typical MOVPE reactor with a gas mixing system. From [20].

liquid MO precursors, which are sealed in the bubblers and immersed in a thermal bath, are conveyed into vapor and pushed to the reactor by a carrier gas, typically N_2 or H_2. At the equilibrium, the amount of extracted precursor (i.e. molar flow rate X_{MO}) depends on the precursor's vapor pressure P_{MO} (which is determined by the thermal bath temperature), the bubbler pressure P_C and the carrier gas flow Q_S through the equation [20]:

$$X_{MO}[mol/min] = \frac{Q_S[sccm]}{22400[scc/mol]} * \frac{P_{MO}}{P_C - P_{MO}} \tag{2.1}$$

Once the desired amount of precursor has been taken from the bubbler, it can be delivered to the growth chamber through the run line or exhausted through the vent line. This additional path is important in order to minimize precursor fluctuations after switching on the carrier gas flow. Usually the precursor line is opened in advance and sent to the vent line before switching to run line in order to avoid the initial non equilibrium transient in which equation 2.1 does not hold.

Once the precursors are delivered to the reactor chamber, the growth takes place. In figure 2.2 it is shown the simplified growth mechanism of GaN, where it is possible to distinguish three different regions: gas phase, boundary layer and surface. The diffusion of the MO precursors to the growth surface is determined by the boundary layer. This region is characterized by a gradient in metalorganic concentration, which contributes to the diffusion of metallic precursors from the gas phase towards the surface. The stronger is the concentration difference, the higher is the growth rate. Moreover, also the substrate temperature has an influence on the growth rate and growth regime. At low temperatures ($\sim 500°C$), the slow surface reaction rate is the limiting factor of the growth, while having higher temperatures increases surface reaction rate up to a point where the limiting factor becomes the diffusion of the precursors from the gas phase (i.e. transportation limited regime). Under this regime, typically used for the growth of III-N semiconductors, the growth rate is determined by the relation [20]:

$$R_g \sim \rho D(Y_{max} - Y_{surf})\delta^{-1} \tag{2.2}$$

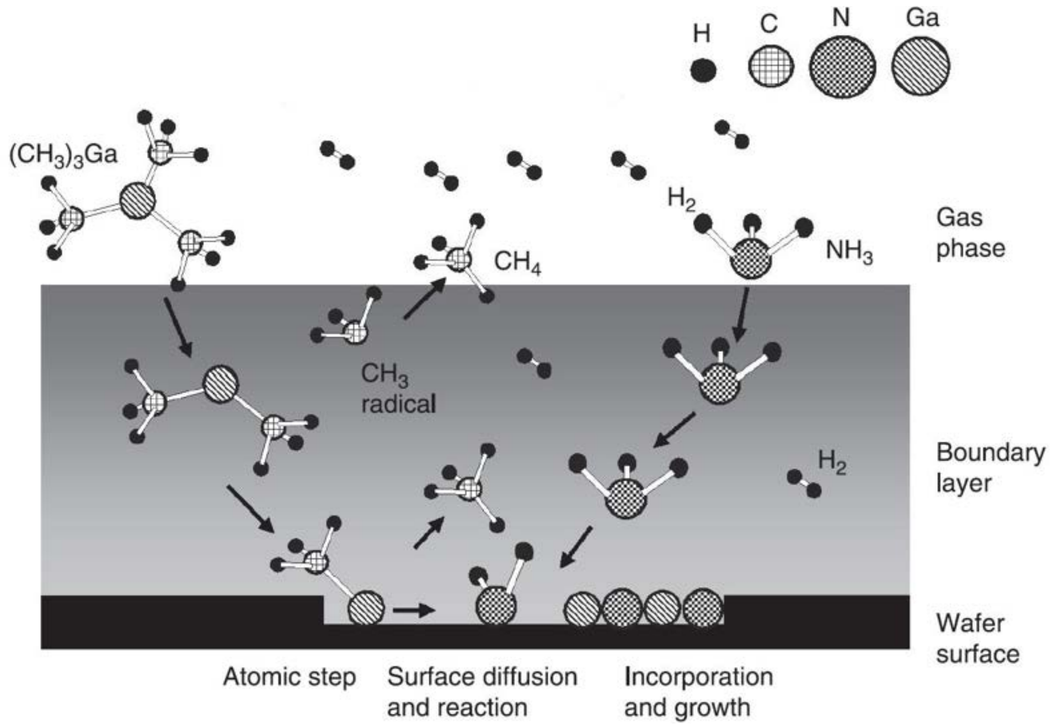

Figure 2.2: Simplified growth mechanism of GaN by MOVPE. It is possible to distinguish three regions: gas phase, boundary layer and surface. From [20].

$$\rho \sim PT^{-1} \tag{2.3}$$

$$D \sim T^{1.7}P^{-1} \tag{2.4}$$

where ρ is the gas density, D is the diffusion coefficient of the MO species, Y_{max} and Y_{surf} are the MO concentration in the gas phase and on the surface respectively, δ is the thickness of the boundary layer, P is the reactor pressure and T is the substrate temperature. By combining the above equations it is possible to demonstrate that the growth rate should not depend on reactor pressure [50]. However, there are several groups reporting a change in growth rate or incorporation with reactor pressure [46–51]. This highlights an issue related to MOVPE growth, which is the pre-reaction in the gas phase. This mechanism takes place when different active species react in the gas phase to form stable nanoparticles. This unwanted reaction reduces the effective amount of precursors that reaches the surface and contributes to the growth. A typical MOVPE growth is carried out at a reactor pressure between 50 and 1000 mbar, therefore the interaction between different species in the gas phase is unavoidable due to the collisional regime. For example, one of the most known pre-reaction is the one between metalorganic precursors and ammonia [48]. Understanding and minimizing the impact of these reactions is of fundamental importance in order to avoid quality degradation of the growing sample.

Partly in the gas phase and once the precursors reach the heated sample, they undergo pyrolysis and separate into active species and byproducts. The active species are the one incorporated in the growing film, while the reaction byproducts are expelled through the vacuum pump. It is clear that each precursor behaves differently due to the different chemical composition and it has to be chosen properly in order to optimize the crystal quality of

the grown material. For instance, one of the most important issues connected especially to low temperature growth of III-N materials is the incorporation of carbon and oxygen defects due to reaction byproducts [22, 52, 53].

In the next section, a more detailed discussion on MO precursor and carrier gases will be presented together with their most important characteristics.

2.1.2 Metalorganic Precursors and Carrier Gases

The most used MO precursors for the growth of (Al,In,Ga)N alloys are trimethylgallium (TMGa), triethylgallium (TEGa), trimethylindium (TMIn) and trimethylaluminum (TMAl). Nitrogen is most commonly supplied as ammonia (NH_3) while the precursors for n-type and p-type dopants are respectively silane (SiH_4) and bis-ethyl-cyclopentadienyl magnesium (Cp_2Mg). In table 2.1 are reported the vapor pressures as a function of temperature and the chemical formulas of the MO precursors used in this work, as well as the used bubbler temperatures and pressures and the resulting molar flow rates per unit flow calculated using equation 2.1 [54].

Metalorganic Precursor	Chemical Formula	Vapor Pressure (P in Torr, T in K)	Bubbler T (°C)	Bubbler P (Torr)	Molar flow rate (mol/min)
TMAl	$(CH_3)_3Al$	Log(P) = 8.224-2134.83/T	20	757	4.87e-7
TMGa	$(CH_3)_3Ga$	Log(P) = 8.07-1703/T	3	757	5.22e-6
TEGa	$(C_2H_5)_3Ga$	Log(P) = 8.083-2162/T	20	757	2.82e-7
TMIn	$(CH_3)_3In$	Log(P) = 10.52-3014/T	20	757	9.33e-8

Table 2.1: Vapor pressure as a function of temperature for the precursors used in this works. Bubbler temperatures and pressures and the resulting molar flow rates per unit flow are also reported.

As shown in formula 2.1, the MO flow rate can be controlled by changing the precursor vapor pressure, which is defined as the pressure exerted by a vapor in thermodynamic equilibrium with its condensed phase (typically liquid for MO precursors) at a given temperature in a closed system (i.e. the bubbler). The vapor pressure is strictly related to the evaporation rate and depends on the molecular weight of the compound: heavier compounds tend to have larger vapor pressures. In figure 2.3 it is shown the dependence of vapor pressure on temperature taken from table 2.1, the circles indicate the selected temperatures and vapor pressure of each precursor used. It is clear from the figure that TMGa has a much higher vapor pressure compared to the other precursors and this has to be taken into account when choosing how to perform the growth. Using precursors with similar vapor pressures is particularly important when growing alloys, in order to have similar MO flow rate with comparable carrier gas flows and therefore avoids unwanted turbulences. Based on this requirements it is clear that using only TMGa as gallium precursor is not the best solution. As an example, the precursors which can be used to grow InGaN are TMIn for indium and TMGa or TEGa for gallium. Since at room temperature TMGa has a vapor pressure two orders of magnitude larger than TMIn, it is difficult to have similar amount of metalorganic molecules using a reasonable carrier gas flow. This can be avoided by decreasing the bubbler temperature below 0°C or to use a dilution line. On the other hand, TEGa has a much closer vapor pressure to TMIn, making it easier to have 1:1 MO ratio. For these reasons, historically the precursors used to grow InGaN were TMIn and TEGa.

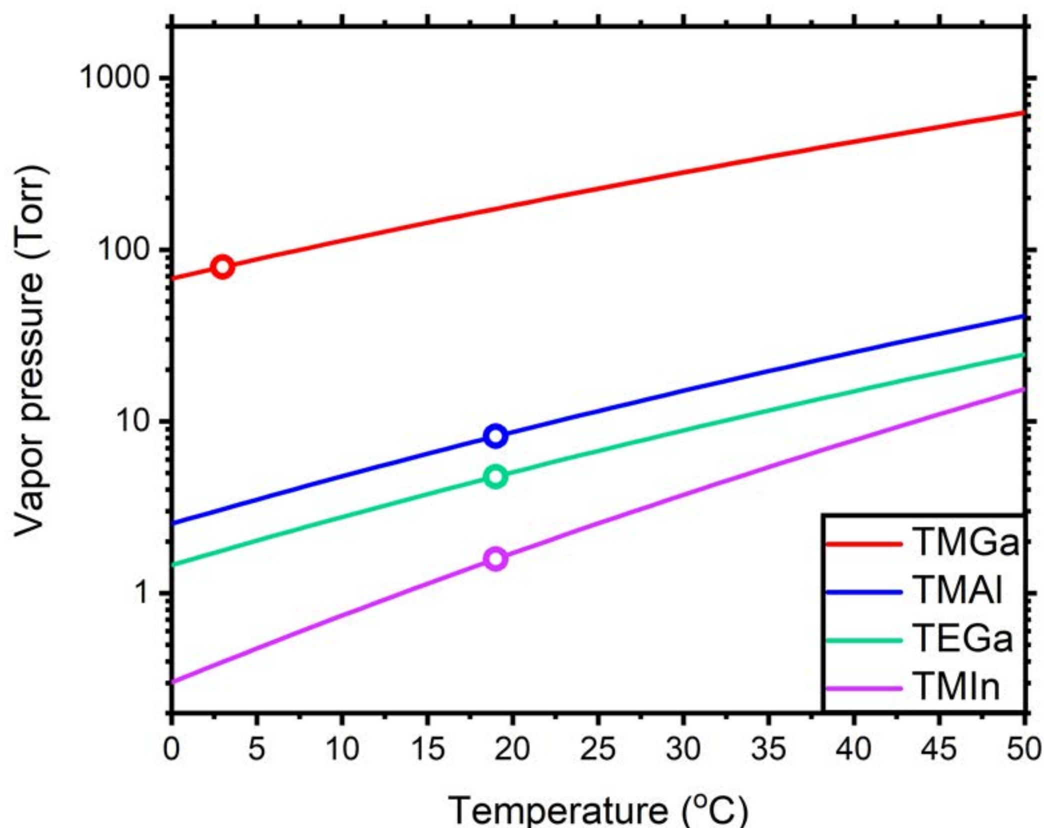

Figure 2.3: Vapor pressure of the used MO precursors as a function of temperature. Circles indicate the resulting precursor pressure based on each bubbler temperature.

Another aspect which depends on the used precursors are parasitic reactions. As introduced before, parasitic reaction between MO precursors and NH_3 is a phenomenon that takes place in the gas phase and has a strong impact on the growth on III-N materials [55]. Although these chemical processes are not yet fully understood, Creighton et al. developed a widely accepted model to describe the parasitic chemistry that takes place during MOVPE growth [48]. They studied the formation of nanoparticles in the gas phase which results in a reduction of the growth rate [50] and metal incorporation in the growing film [46,49,56]. In literature are described two different reaction paths with very different activation energies. The low energy one, followed by TMGa [55], TEGa and TMIn, does not have a severe impact on growth performance. The second one, which requires high temperatures to overcome the large activation energy, is followed by TMAl [55, 57] and has to be avoided in order to increase aluminum incorporation and reduce surface roughening [49, 56]. Some strategies to reduce the impact of parasitic reactions are the optimization of growth pressure [46, 49], the choice of carrier gas [58, 59] and V/III ratio [50, 56, 60].

Other critical aspects related to the chemistry of MOVPE growth are pyrolysis efficiency and byproduct formation and in particular the production of CH_3 radicals [61]. It is generally believed that by decomposing on the surface, those radicals introduce carbon impurities in the growing layer by the formation of highly reactive species [62, 63]. One solution to avoid this problem can be the usage of precursors with larger radicals such as

TEGa instead of TMGa, where the methyl radical is replaced by the ethyl. In this case the reaction path is different [64] and this usually leads to a lower carbon incorporation in the growing film [65, 66], at least at low growth temperatures. Indeed, it was observed that using TEGa at high growth temperatures results in a much larger C incorporation compared to TMGa [67]. Moreover, due to its synthesis process, TEGa contains a large density of Si and O impurities which can be incorporated in the growing film as point defects. Another solution is to minimize carbon doping levels by optimizing the growth parameters such as temperature, pressure and precursor flow rates [68]. In a recent work, Danielsson et al. studied carbon incorporation from TMGa by combining experimental measurements and computational fluid dynamics coupled with a chemical kinetic model [63]. The most interesting result shows that carbon incorporation is strongly affected by the growth temperature, showing that it can be reduced from 1×10^{20} at 800°C to 3×10^{16} at 1050°C. Since Ga atoms reach the surface via $GaCH_3$, this suggests the presence of a mechanism that removes the methyl radicals before they are incorporated in the crystal [8]. Although this topic is still under discussion, experimental results clearly show that low carbon incorporation can be obtained using TMGa by growing at high temperatures.

Nitrogen is an inert gas in its stable form N_2, therefore it has to be modified in order to become reactive. One possibility is to generate a nitrogen plasma by ionizing the gas particles, another one is to create nitrogen compounds with lower dissociation energy. The use of a plasma cell is mostly used in molecular beam epitaxy, while nitrogen compounds are typically used in MOVPE. In the latter case, the most used nitrogen source for III-N growth is ammonia (NH_3). Upon reaching the heated surface, the gas thermally decomposes releasing the active nitrogen species. Some alternatives such as hydrazine and its derivatives were developed but never became popular due to inferior properties. However, despite being widely used, ammonia is far from being an efficient source of nitrogen. First of all, its decomposition efficiency is very low even at high temperatures. Therefore, in order to have enough active nitrogen very high flows are required (typically V/III ratio are close to 1000:1). Consequently, the waste of gas is one of the most important disadvantages of ammonia, together with the required high temperatures for thermal cracking and the pre-reactions with MO precursors (in particular TMAl).

Due to the high density of incorporated defects (Si, O and C), III-N materials usually show a background n-type conductivity. In order to intentionally dope the material it has been shown that Si [69] and Mg [70] are the most effective n-type and p-type dopants respectively. Typically, silicon is supplied as silane (SiH_4), which after thermal decomposition releases Si atoms on the surface. However, it was observed that for doping concentrations above $\sim 2\times10^{19}cm^{-3}$ surface roughening occurs [71,72]. This limits the maximum doping level achievable using MOVPE. Even more critical is the situation related to p-type doping. In this case, the commonly used sources for Mg are metalorganic precursors (CpMg and derivatives). In GaN, magnesium forms a deep acceptor state with activation energies between 155 meV and 230 meV [73], which lead to a low ionization efficiency (around 1% at room temperature). Moreover, activation energy increases with increasing band gap, making even more difficult to have a significant hole concentration in AlN and AlGaN. One of the most severe problems related to Mg doping is the passivation caused by hydrogen. As discussed in section 1.4, during the growth hydrogen binds to the Mg atoms inhibiting the acceptor behavior. Another problem strictly related to the Mg passivation is its self compensation mechanism [74, 75]. When an impurity has an amphoteric behavior (i.e. it can

act both as a donor or acceptor) it may happen that the number of sites in which it acts as a donor equals the number of sites in which it acts as an acceptor. As a result, despite having a large number of impurities there is no net doping. It was shown that in order to prevent self compensation of Mg due to its amphoteric behavior it has to be passivated during the growth by supplying hydrogen [76]. Finally, in order to activate the Mg acceptors (i.e. breaking the Mg-H bond) a thermal treatment is required to remove hydrogen terminations [30, 31]. Due to low efficiency, p-type doping is still a challenging task for III-N semiconductors, with doping concentrations that rarely exceed few $1 \times 10^{18} cm^{-3}$ [77].

Due to different chemical interactions, the choice of carrier gas can have profound effects on growth properties. For the growth of III-N compounds, the most used carrier gases are H_2, N_2 or a combination of the two. Koukitu et al [78] studied the thermodynamical effect of H_2 on the deposition process of AlN, GaN, InN and InGaN. The results showed that the presence of hydrogen has a deleterious effect especially when using indium. Their explanation is related to the hydrogen partial pressure, which makes the growth reaction (e.g. $In(g) + NH_3(g) = InN(s) + 3/2H_2(g)$) less favorable. Indeed, if the concentration of hydrogen in the atmosphere is too large, the inverse reaction is favored with a negative impact on the growth. It is important to note that also hydrogen generated by the growth reaction has the same effect of increasing the H concentration in the atmosphere. Although this mechanism is present in the growth of all III-N semiconductors, InN alloys are the one most affected due to the smaller equilibrium constants compared to GaN or AlN. This inhibition effect is well known and reported by many other groups [79–81]. Using N_2 instead does not have any chemical impact on the growth reaction, since the energy required to make it reactive is too large and therefore it behaves as an inert gas. Based on this results, the growth of InGaN has to be performed under pure N_2 gas, while for GaN and AlGaN there are no restrictions, or even H_2 is preferable [59].

2.1.3 MOVPE Growth of InGaN

At present times, the cheapest substrate which allows to obtain the highest GaN quality is sapphire. As described in section 1.2, a high quality GaN layer can be achieved by using a two-temperature approach, with the low temperature nucleation layer followed by a high temperature annealing and subsequent growth. The result of this growth process is an atomically smooth surface (see figure 4.1), which can be used as a template for the growth of the QW structures.

As discussed above, the growth temperature has a strong impact on the defects incorporation. A higher growth temperature typically results in a lower defects incorporation and a higher crystal quality. However, it is not possible to increase the temperature above some limits without degrading (or even destroying) the material. As a rule of thumb, the ideal growth temperature for a compound is between 1/2 and 2/3 of the melting temperature of the specific material [82]. This becomes problematic when growing ternary alloys, where the melting temperature is different for each compound. Taking InGaN as an example, the melting point of GaN is 2500°C, while the one of InN is only 1373°C. This large difference demonstrates the difficulty of growing a high quality InGaN, since the choice of the growth temperature has a critical impact on the quality of the material and the indium incorporation. In figure 2.4 it is shown the In content as a function of the growth temperature for different TMIn flows, as reported in ref. [60]. The results shown in the figure demonstrate that the growth temperature has a severe impact on indium incorporation. In the figure is

also indicated a region where phase separation occurs. Here, the two components of the alloy separate and In-rich clusters form in the material, degrading the electrical and optical properties.

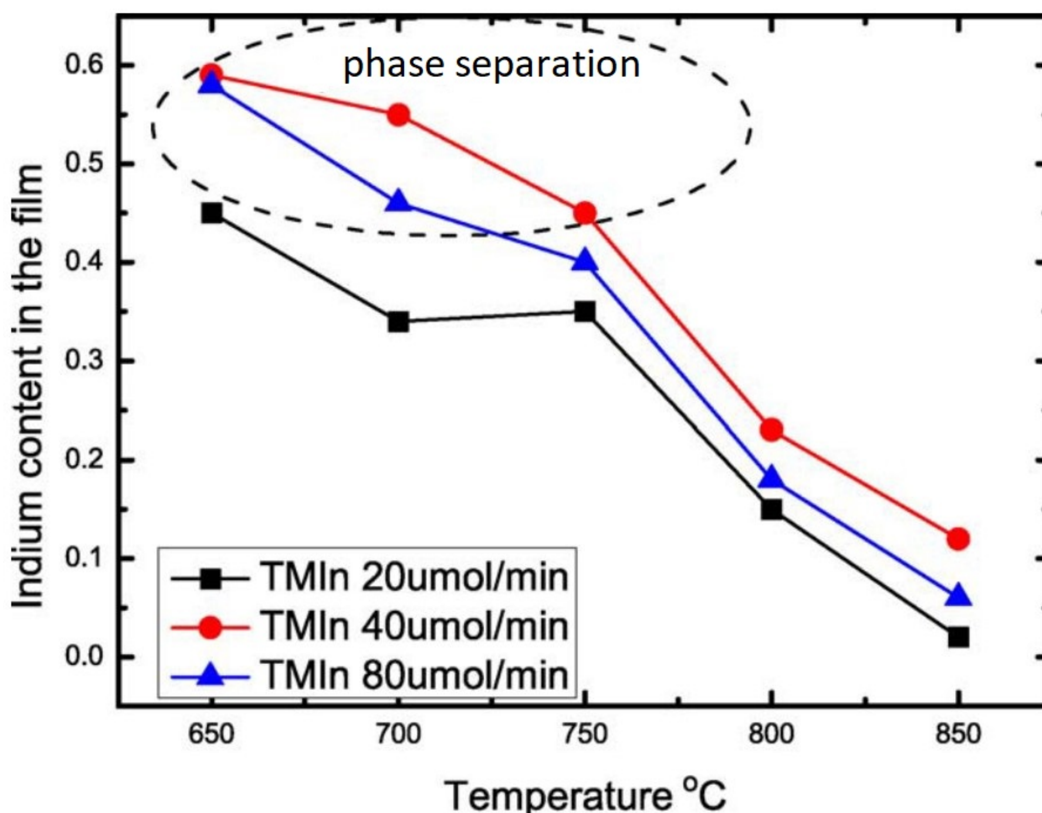

Figure 2.4: Dependence of indium incorporation on the growth temperature for different TMIn flows. From [60].

This phenomenon can be explained by looking at the phase diagram of a coherently strained InGaN layer where the binodal and spinodal curves are indicated, as shown in figure 2.5. These curves help to identify the unstable and metastable phases of a compound with respect to the formation temperature (i.e. the growth temperature). These curves are obtained by imposing the condition that the first derivative (binodal) and second derivative (spinodal) of the Gibbs free energy is zero [83]. The region under the spinodal curve is energetically unstable and it is called the miscibility gap, while the region between the two curves indicates that the compound is metastable. In this second region, if the conditions are properly tuned it is possible to obtain a single-phase compound. As can be seen from figure 2.5, also the strain has an impact on the miscibility gap and the metastable region, especially at high temperatures. Due to the very different properties of InN and GaN, the growth conditions of InGaN have to be carefully controlled in order to obtain a high-quality single-phase crystal.

Typically, the growth temperatures used to obtain InGaN with an In concentration of $\sim$20% are between 700 °C and 800 °C. However, keeping the same low temperature to grow the GaN barrier results in a high defects incorporation (see section 2.1.2). Therefore, the best approach would be to raise the temperature before growing the barrier without

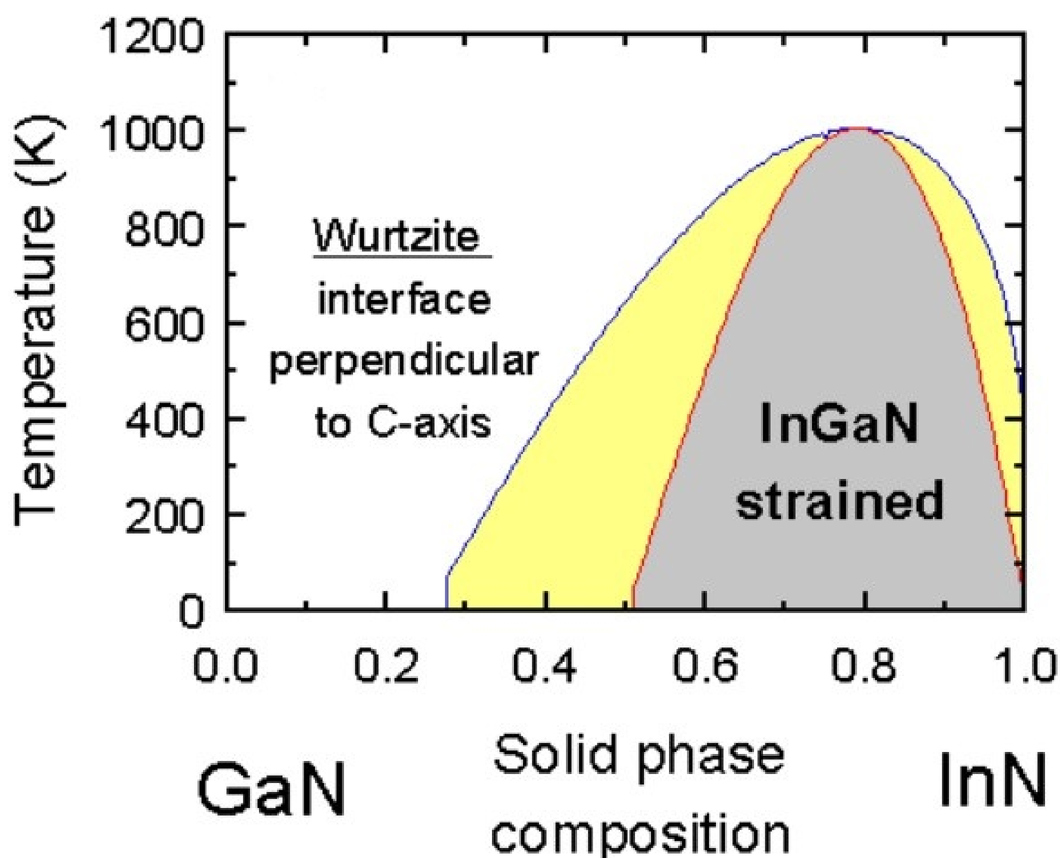

Figure 2.5: Calculated indium composition as a function of temperature for a coherently strained InGaN layer. The blue lines represent the binodal curves, the red lines represent the spinodal curves. From [84].

destroying the quantum well. Indeed, even if the InGaN QW is already grown, raising the temperature too much breaks the In-N bond and results in the formation of In clusters in the material.

Moreover, the interface sharpness is another key factor for optical devices. A rough interface can introduce point defects as well as reducing the local confining potential, resulting in a broader and weaker emission line. The influence of different growth sequences on the interface sharpness was studied by the group of Massabuau et al. [86]. In figure 2.6 are shown the high-angle annular dark field scanning transmission electron microscopy (STEM-HAADF) images taken along the $\langle 11\bar{2}0\rangle$ zone axis of the different GaN/InGaN/GaN MQW samples grown in their work. As can be seen from the image, the best result was obtained using the "Q2T" growth sequence, which stands for "Quasi 2 Temperature". This method consists of growing at low temperature both the QW and the initial part of the top GaN barrier ($\sim$1 nm). After the initial layer is grown, the growth is interrupted and the temperature is increased and finally the last part of the barrier is grown at high temperature. In order to avoid InGaN dissociation, the difference in growth temperature between the QW and the barrier was kept at $\sim$100°C. In figure 2.7 it is reported the measured indium concentration along the growth direction of the QW grown using the Q2T method. This result was obtained by averaging the InGaN composition obtained by the analysis of several high

resolution transmission electron spectroscopy (HRTEM) images (see section 3.3). As can be seen, despite showing a very sharp interface in figure 2.6, the actual indium concentration is quite disuniform. In particular, it is evident the indium tail in the top barrier. This phenomenon was already observed in literature [87, 88] and was attributed to the indium segregation occurring at the surface [89]. The effect of this tail is to reduce the confining potential and therefore modifying locally the transition energies, resulting in a broader emission line width.

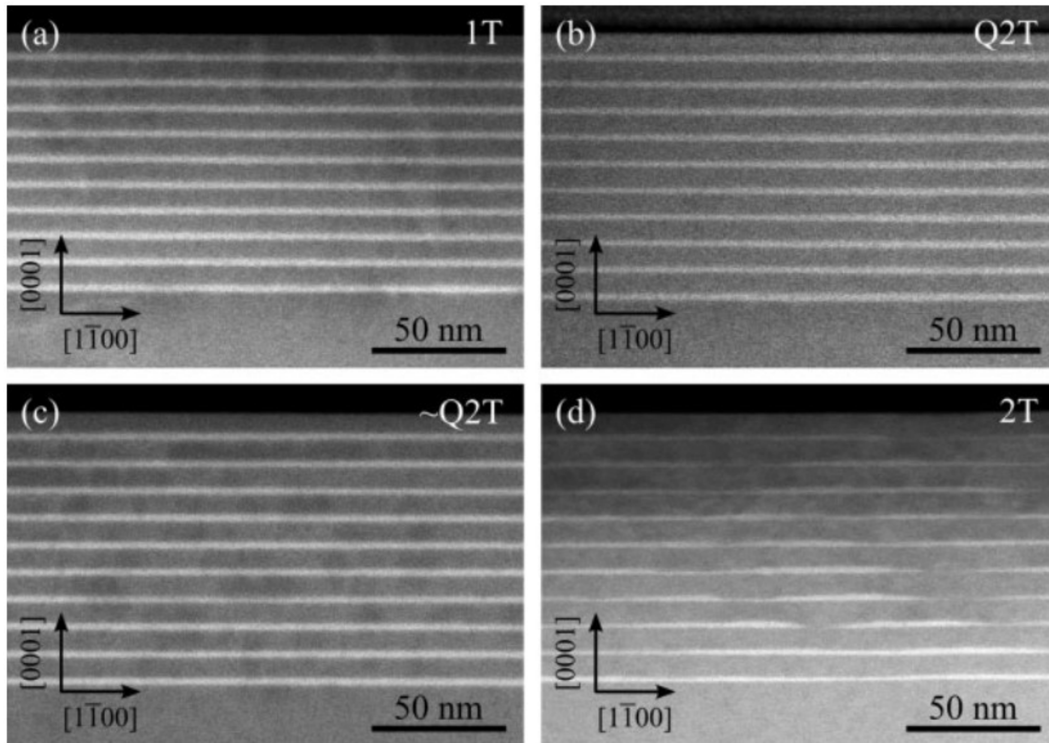

Figure 2.6: STEM-HAADF images taken along the $\langle 11\bar{2}0 \rangle$ zone axis of several GaN//GaN MWQ samples grown using different growth sequences. From [86].

2.2 Molecular Beam Epitaxy

Molecular Beam Epitaxy (MBE) is a thin film growth technique developed by Arthur and LePore in the late 1960s [90]. It was initially developed for the epitaxial growth of Gallium-V compounds but nowadays its usage is much wider. Unlike MOVPE, MBE has typically lower growth rates and it is mostly used in research applications rather than industrial production. Nevertheless, the high control over the growth process makes this technique an interesting alternative to MOVPE, especially for low temperature processes.

2.2.1 MBE Setup

The typical MBE setup is made of three separate chambers: an introduction chamber, a buffer chamber and a main chamber. Since MBE growth is carried out under high vacuum (HV) or ultra-high vacuum (UHV) condition (typically in the range between 10^{-8} and

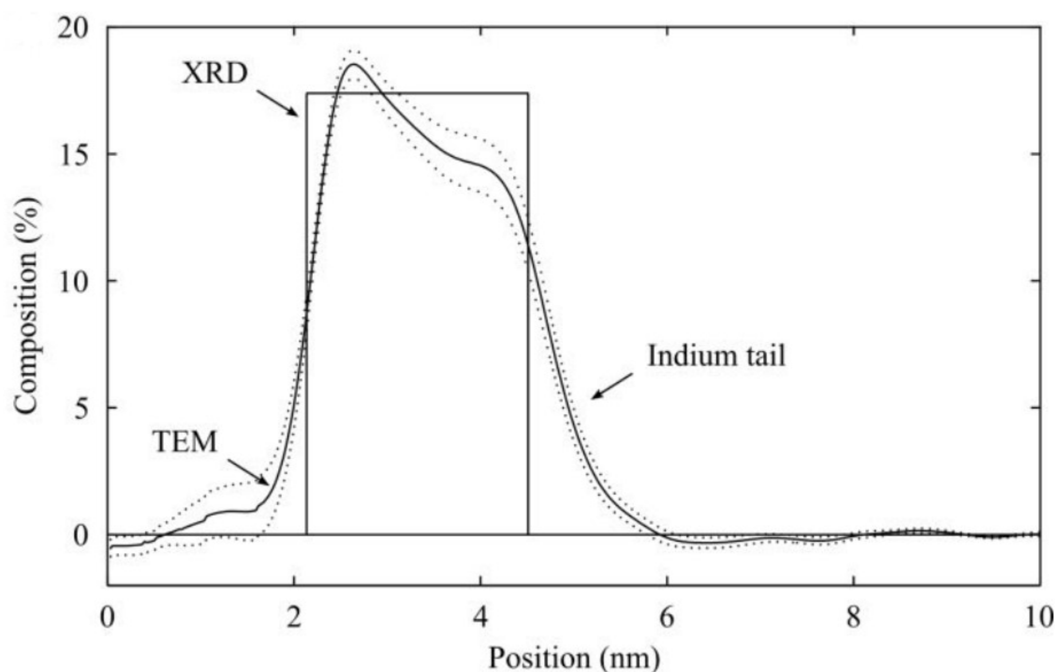

Figure 2.7: Composition profile along the growth direction of the Q2T sample as obtained by HRTEM images. The straight line indicates the average value of several measurements, the dotted lines indicates the standard deviation and the square profile represents the thickness and composition of the QW as obtained from the fitting of XRD measurements. From [86].

10^{-12} Torr), the three-chamber setup is required in order to reduce the contamination from the external environment as much as possible. The MBE used in this work was a modified version of the Riber 32 using a 2” sample holder of which a schematic image is shown in figure 2.8.

Due to the different pressure ranges at which the chambers operates, each of them is equipped with different types of vacuum pumps. The intro chamber is the dirtiest one as it is where the sample is taken in and out and therefore it is in direct contact with the external environment. Since the operation pressure range of this chamber is between atmospheric pressure and HV, it requires a combination of a rough pump (in this work a rotary pump was used) and a turbomolecular pump. The purpose of the rough pump is to produce an initial vacuum of approximately 0.1 Torr which is required by the turbomolecular pump to work properly. In our setup, the intro chamber was also used to perform an initial bake out of the sample in order to remove water contamination from the atmosphere. This process was done by heating the sample at 180°C for several hours. The sample is then moved to the buffer chamber, in which the samples can be stored in a clean environment. The other fundamental importance of the buffer chamber is to isolate the clean growth chamber from the dirtier intro chamber. Since the pressure in this chamber has to be kept constant in the HV regime, it is usually equipped only with an ion pump. Finally, the main chamber is where the growth takes place. It is the cleanest chamber and it is constantly kept in UVH. For the growth of nitrides, this chamber is usually equipped with a rough pump and a turbomolecular pump. This equipment is necessary since during the growth a large nitrogen flux is supplied and therefore a pump able to remove efficiently a large amount of gas is

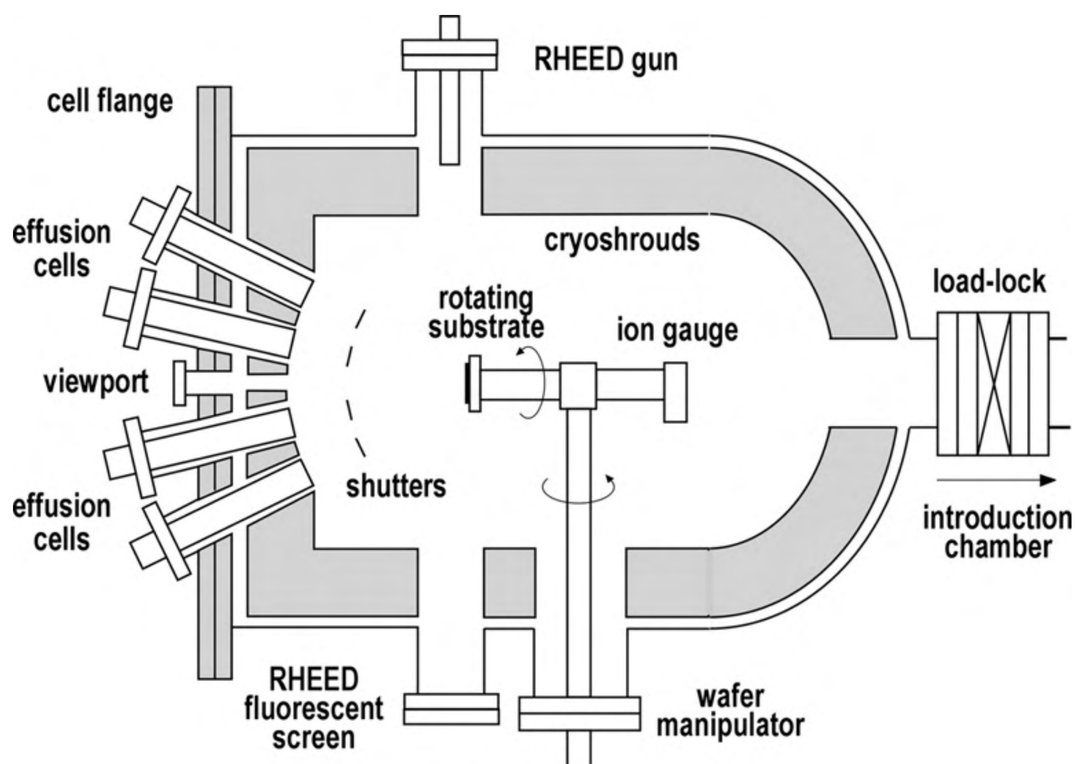

Figure 2.8: Schematics of the growth chamber of a Riber 32 machine.

required to maintain the non-collisional regime.

A great advantage of MBE is the compatibility with in-situ characterization techniques. Of particular interest is the reflection high-energy electron diffraction (RHEED), which gives information on the surface morphology in real-time. A detailed description of this characterization technique is given in section 3.1.

The metal sources used for the growth are stored in specific evaporators called Knudsen cells, which are directly attached to the main chamber in a symmetrical shape with respect to the sample position. This geometry is studied in order to have homogeneous fluxes reaching the sample from all the cells. The molecular fluxes are obtained by heating up the Knudsen cells due to the Joule effect. Typically the molecular flux is expressed in terms of the beam equivalent pressure (BEP), which can measured by a pressure gauge placed in the same position of the sample. This value is proportional to the impinging flux on the surface. In figure 2.9 are reported the measured BEP of gallium and indium as a function of temperature. The dashed lines represent the linear fit of the data for which $P \propto 10^{-1/T}$. It is important to notice that the BEP depends not only on temperature, but also on the crucible aperture, the molecular mass and the distance between the source and the substrate position.

Since nitrogen is a gas, it can't be supplied in the same way as the group III metals with the Knudsen cells. As anticipated in the previous section, the two most common methods of supplying nitrogen are using ammonia or by generating a nitrogen plasma. The supply of nitrogen in an ammonia MBE is extremely similar to the MOVPE system. Ammonia gas is supplied in the growth chamber through a dedicated line and the active nitrogen species are generated on the surface as a consequence of the thermal decomposition. The high tem-

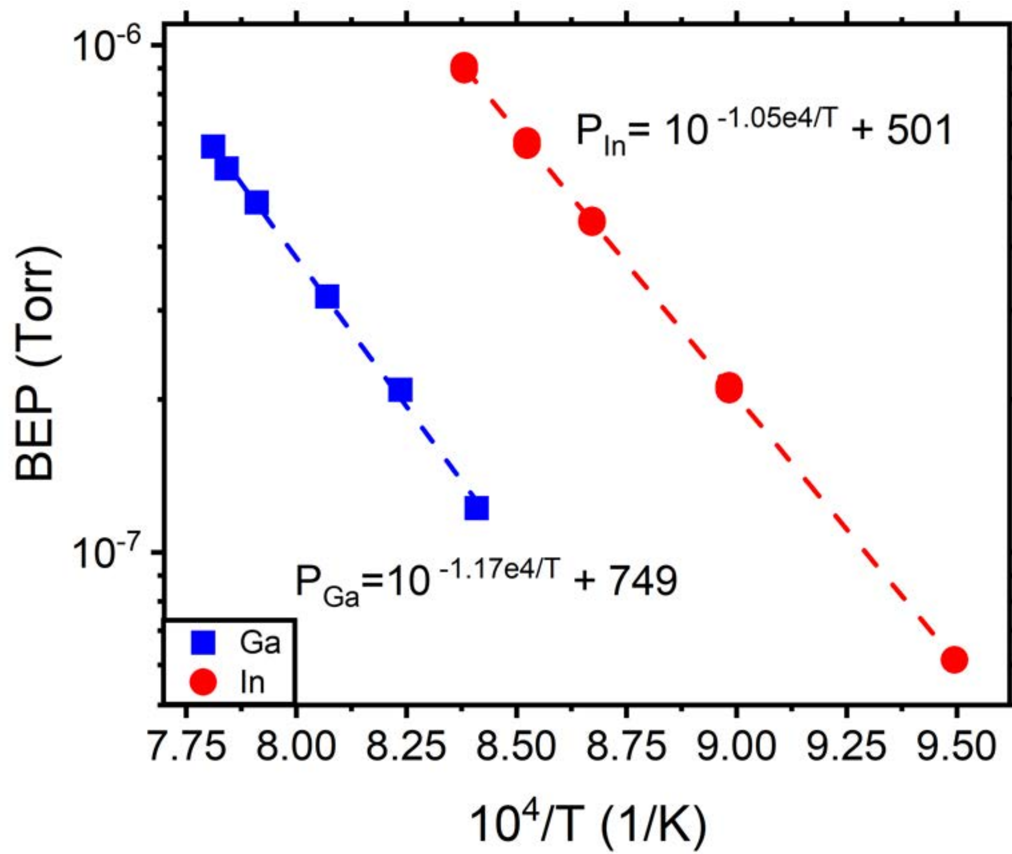

Figure 2.9: Beam equivalent pressure of Ga and In measured as a function of temperatures in the used MBE. The dashed line represent the linear fit of the data.

peratures required to have an efficient decomposition are hardly reached in MBE compared to MOVPE. As a consequence, the usage of ammonia is limited mostly to high-temperature growths. More commonly in MBE the nitrogen is supplied as a plasma by a special plasma source. This system is commonly called plasma assisted MBE (PA-MBE). In this case, the source of nitrogen is an ultrapure N_2 gas which is sent to the plasma cell and finally in the growth chamber. The flux is controlled by means of a mass flow controller and it is typically kept in the range of few sccm (i.e. standard cubic centimeter per minute) in order to maintain the non-collisional regime. The gas flowing into the plasma cell is transformed to a nitrogen plasma by an alternated current flowing in an electric circuit. The type of circuit used to induce the plasma has a strong influence on its properties. The most commonly used plasma sources are the capacitively coupled (CCP) and inductively coupled (ICP) plasma sources. In a CCP system a radio frequency (13.56 MHz) power supply is connected to an electrode while the other one is grounded, forming a capacitor-like circuit. An initial electric discharge ignites the nitrogen gas, ionizing part of it. Then, the alternated current provided by the RF power supply induces an oscillating electric field between the electrodes which is followed by the ionized electrons. This high-energy electrons oscillate and ionize other atoms on collision. If the field is sufficiently strong it will induce an electron avalanche, ionizing all the gas and transforming it into a nitrogen plasma. The difference between ICP and CCP systems is the mechanism to generate the oscillating field. In the case of ICP, the alternated current flows through an inductive coil to induce an oscillating magnetic field. This in turn generates an oscillating electric field which is followed by the ionized electrons as happens in CCP systems. The different generation methods affects the properties of the plasma. In particular, the density of ionized electrons in CCP is $\approx 10^9$-10^{10} cm^{-3} while in the case of ICP the electron density reaches 10^{12} cm^{-3}. However, CCP is able to generate more energetic ions compared to ICP [91].

The plasma source used in this work is a patented system which is an hybrid between ICP and CCP. This high-density radical source (HDRS) is able to produce both a high-density and high-energy plasma by combining the two methods described above. In particular, this plasma source is able to produce a N radical density on the order of 10^{11} cm^{-3} with the cell parameters used in this work. The radical density is mostly affected by the N_2 flow, with an increase of more than two times going from 1 sccm to 3 sccm. On the other hand, the input power does not have a profound effect on radical density, increasing it by $\sim$40% from 300 W to 600 W.

2.3 MBE Growth Kinetics

Compared to MOVPE, the growth mechanism taking place in MBE is extremely different. First of all, the use of pure molecular sources permits to avoid the complicated chemical reaction required to supply the metal atoms. This permits to avoid the pre-reaction problem and contamination due to the unefficient thermal dissociation of precursors. Second, due to the UHV environment and non-collisional regime the atoms follow a straight path after the evaporation and therefore only the ones with the correct trajectory can impinge on the sample surface. Moreover, the incorporation and desorption process are only related to surface kinetics and do not depend on the density of atoms in the gas phase. As a result, the MBE growth process can be understood by studying the surface dynamics in a kinetic approach.

When an atom impinges on the surface it can adsorbe, diffuse and desorbe or bind and be incorporated in the growing layer. The absorption process can be classified into physisorption or chemisorption depending on the bond strength. Physisorbed atoms, as the name suggests, are only weakly bound to the surface due to the large bond length and there is no chemical interaction between the atoms. The chemisorption process instead involves a chemical bond with the surface atoms to form a compound. In this case the bond strength is much higher compared to the physisorption case. The processes of diffusion and desorption depend on substrate temperature through the exponential law $e^{-\frac{\Delta E}{KT}}$ with ΔE as the activation energy. Having a large diffusion length is important to have a high crystal quality since the atoms have a larger probability to find a good nucleation sites. However, a high temperature increases the probability of desorption as well, reducing the total number of atoms contributing to the growth and the residence time on the surface as well. In extreme cases a temperature too high may also cause the dissociation of bound atoms, leading to a roughening of the surface. In III-V growths the surface dynamics of the atoms of the two groups is profoundly different. At the typical growth temperatures, the group V elements are generally found in the gas phase while group III elements are liquid. This difference is found also in the activation energies of the surface processes which are quite different. In particular, the diffusivity of group V elements is negligible compared to group III atoms. As a consequence, the residence time of the metal atoms on the surface is much higher and surface dynamics is mostly determined by the kinetics of group III atoms. However, the density of group V elements on the surface has a strong impact on the diffusion properties of the metal atoms as it affects the probability of binding to form a stable compound.

2.4 MBE Growth of GaN

As discussed above, MBE growth is affected by the substrate temperature and the flux of the sources. However, the total amount of impinging atoms on the surface of each specie does not have an impact on the growth regime. Instead, the flux difference between group III and group V elements determines if the growth is carried out under N or Ga rich environment, with important consequences on the growth quality. Therefore, the two most important parameters which control the growth process are the substrate temperature and the flux difference between Ga and N. Based on these parameters it is possible to define a growth diagram to describe the expected growth conditions and results, as shown in figure 2.10.

It is immediately clear from figure 2.10 that the temperatures used in MBE growth of GaN are much lower compared to MOVPE. A too high growth temperature results in a large GaN dissociation and desorption which has to be balanced by a large flux of gallium and nitrogen. Since this possibility is limited by the obtainable evaporation rates and the non-collisional regime which must be preserved, the GaN growth temperatures with MBE are intrinsically lower than MOVPE. As a consequence the typical MBE growth conditions are very different from MOVPE. Indeed, as discussed in 2.1.2, MOVPE growth is carried out in a very nitrogen rich environment with typical V/III ratios of 1000:1. On the other hand, the best MBE growth condition is obtained under a slightly Ga-rich condition. By looking at figure 2.10, it is possible to distinguish five different growth regimes depending on substrate temperature and III/V ratio. As mentioned before, the best results are obtained in the so called intermediate regime, under a slight excess of Ga and in particular when a thin layer of liquid Ga (between $\sim$2.4 ML and 1 ML) is present on the surface. The reason for this is

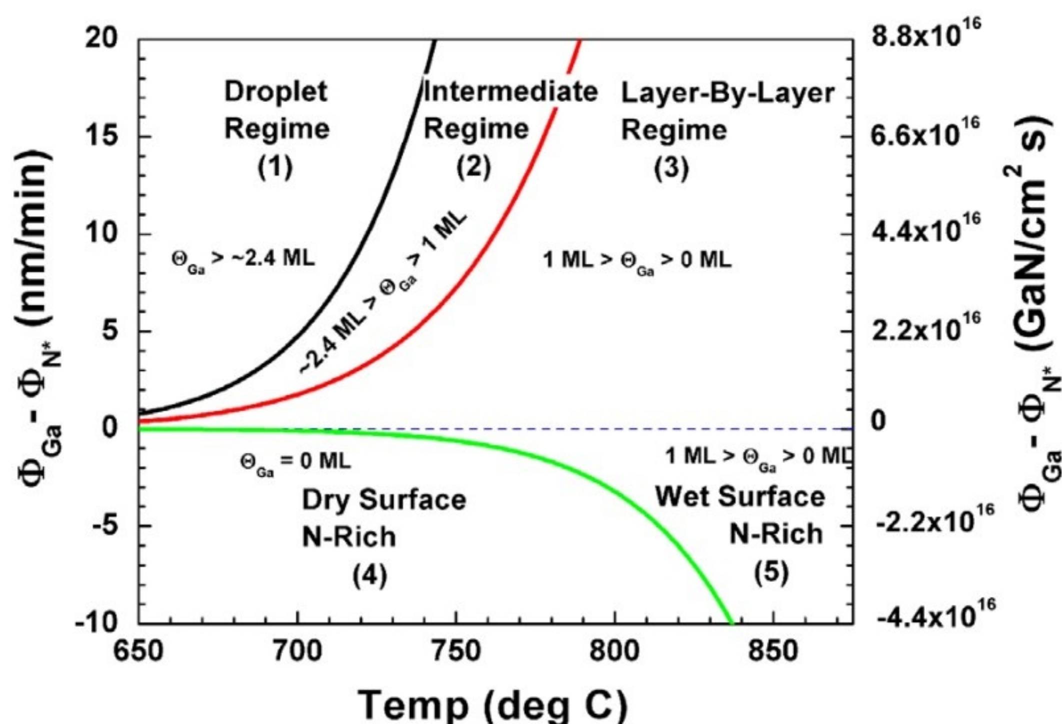

Figure 2.10: MBE growth diagram of GaN, where it is possible to distinguish five different growth regimes. The fluxes are given in units of nm/min, calibrated for temperatures with negligible thermal decomposition. From [92]

related to surface kinetics of Ga and N adatoms. Typically the diffusion mechanisms have a large activation energy which require a high growth temperature (typically between 1/2 and 2/3 of the melting temperature of the material) to enable a smooth surface. However, Neugebauer et al. discovered a diffusion mechanism with a much lower activation temperature. This mechanism, which they called adlayer enhanced lateral diffusion (AELD), is thought to be responsible for the high quality obtained in the intermediate regime [93, 94]. They have shown that both a Ga bilayer or an In adlayer act as surfactants, decreasing the activation energy of the diffusion process and therefore enhancing adatoms mobility. Their calculations showed a reduction in the diffusion barrier of Ga adatoms from 0.7 eV to 0.12 eV without modifications to the adsorption sites and diffusion paths. Nitrogen atoms instead penetrate below the metallic layer and bound strongly with the underlying Ga, while the bond with the atoms in the metallic layer is much weaker. As a consequence, gallium diffusion is greatly enhanced and the metallic adlayer does not bind with nitrogen, resulting in a high quality growth even at relatively low temperatures. The Ga bilayer in the intermediate regime is stable, which means that the amount of liquid gallium does not increase with growth time. However, if the net metal flux is too large or the growth temperature is too low, Ga start to accumulate and forms droplets. On the other hand, a smooth surface can be obtained even when the metal coverage is below 1 ML. In this case however a larger growth temperature is required to compensate the lower mobility of adatoms compared to the bilayer case.

Typically, under a nitrogen rich environment (region 4 of figure 2.10) the low growth

temperature and the large nitrogen flux result in a low diffusion length of GaN and a rough surface. However, recent results [95, 96] have shown that a very high quality GaN can be obtained under N-rich environment by growing at temperatures above GaN thermal decomposition. When the Ga-N bond is broken, nitrogen desorbs rapidly while gallium stays on the surface for longer times. As a consequence, also in this case a metallic layer can be found on the surface which however is produced by GaN decomposition rather than a III/V ratio larger than 1. Moreover, under this condition the growth temperature can be much higher compared to the intermediate regime, which results in even better crystal quality [95]. However, to be able to grow in this regime it is necessary to have very high fluxes to compensate for the loss of material.

3

Characterization Techniques

3.1 Reflection High-Energy Electron Diffraction

Reflection High-Energy Electron Diffraction (RHEED) is an in-situ characterization technique which is typically used in the MBE setup. It is a very convenient characterization technique to monitor the surface morphology and reconstruction during the growth. Moreover, analyzing the intensity oscillations of the diffraction pattern gives information on the growth rate with a precision of the order of one monolayer. A collimated electron beam with an energy of 10-100 KeV is sent on the sample surface at a grazing angle ($\sim 2°$) and the diffracted beam is collected by a fluorescent screen. Thanks to the grazing incidence, the vertical penetration depth of the electron beam is of few nm which makes this technique suitable for surface analysis. Typically the beam spot size on the surface is of few mm, which means that the information obtained are an average over that macroscopic size.

The working principle of RHEED can described using the Ewald construction. A wave vector $\vec{k}$ can be associated to the incident beam. The Laue condition for constructive interference is realized when $K_{||} = k^{'}_{||} - k_{||}$, where $k^{'}$ is the wave vector of the electron beam exiting the surface and $||$ refers to the component of the vector parallel to the sample surface. In the above condition $K_{||}$ is a vector of the surface reciprocal-lattice which corresponds to a rod due to the lattice symmetry breaking at the surface. Visually, the Laue condition is fulfilled when a 2D lattice rod is intersected by the Ewald sphere, which is the sphere constructed in the reciprocal space with radius k and touching the (0,0) point (i.e. the origin of the 2D reciprocal space). The real-space surface morphology modifies the shape of the ideal reciprocal lattice rods, which in turn affect the diffraction pattern. In figure 3.1 are reported some RHEED patterns depending on the surface morphology. In particular, an ideally flat surface has thin reciprocal space rods and produces single spots in the RHEED pattern corresponding to the intersection of the Ewald sphere with the rods. A less ideal surface results in a streaky or modulated pattern. Finally, transmission spots are observed in case of islands since the bulk periodicity is restored.

3.2 Reflectance

Studying the reflectance spectrum is a fast and powerful technique used to obtain the thickness of a thin film by measuring the intensity of the reflected radiation as a function of the

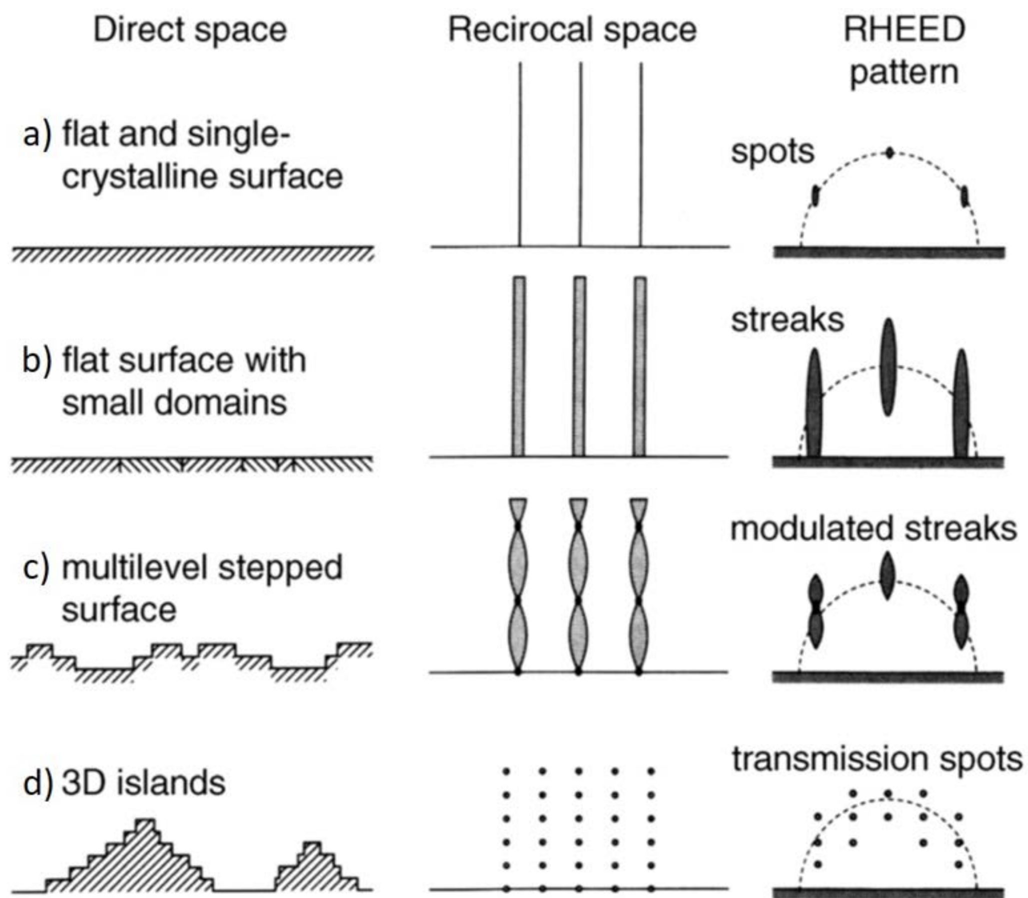

Figure 3.1: Schematics of RHEED pattern depending on surface morphology.

incident wavelength. When the radiation encounters an interface between different materials, part of the beam is reflected and part is refracted. In a thin film, when two interfaces are present, this phenomenon takes place at the air/film and film/substrate interfaces. In this way, the radiation which is refracted at the first interface and reflected at the second can interfere with the incident radiation at the air/sample interface. This results in constructive or disruptive interference depending on the path traveled by the light, which is related to the film thickness. If the refractive indexes of the materials are known, the reflectance spectrum can be fitted by using the formula 1 of ref. [97] with the thickness of the film as the fitting parameter. The use of this technique to calculate the film thickness is particularly accurate. The uncertainties depend on the spectral width of the incident radiation, on the resolution of the detector and on the sharpness of the interfaces. However, when multiple interference peaks are visible in the spectrum (i.e. for thick samples) the error reduces significantly to the order of nanometer.

This technique can also give some hints about the origin of some side peaks typically observed in PL measurements of InGaN QWs. The emitted light originated from the optical recombination process undergoes the same phenomenon of diffraction and reflection at the interfaces described above. Since the emission spectrum is typically broad in the orange-red region, a great number of photons with different wavelengths is emitted, which can interfere enhancing or suppressing the emission of specific wavelengths. When the interference occurring at the air/film interface is constructive, the light extraction is enhanced resulting in an apparent peak in the PL spectrum. An example of this phenomenon is shown in figure 4.13, where it is possible to observe that many local maxima of the PL spectrum correspond to reflectivity maxima.

3.3 Transmission Electron Microscopy

Transmission electron microscopy (TEM) is an imaging technique which uses the transmitted electrons to reconstruct an image of the sample. This technique is particularly interesting since it has an atomic resolution and it permits to distinguish the different atomic species. An electron beam is accelerated towards the sample by an accelerating potential of several KV. After being focused by means of electromagnetic lenses, part of the beam is transmitted through the sample and it is measured with a fluorescent screen or a photo-multiplier. The image shown in this thesis was taken using a Hitachi HD-2700 scanning TEM (STEM). In this technique the beam is focused in a spot with a diameter of $\sim$0.2 nm, which is moved across the sample to form the final image. The interaction of the electron beam with the atoms of the sample depends on their atomic mass and it affects the output image. In the case of this work, a heavier atom results in a brighter image, as can be seen from figure 4.9. Therefore, not only it is possible to have an atomic resolution to visualize the atomic arrangement, but it is also possible to identify each atomic species by analyzing the contrast.

3.4 Atomic Force Micrscopy

Atomic force microscopy (AFM) is a technique developed to study the morphological properties of materials at the nanometer scale. In this technique the surface is probed with a sharp tip mounted at the end of a cantilever. The in-plane movement of the sample stage are finely controlled by piezoelectric elements with a lateral resolution of several nm. When the tip

approaches the sample, the interatomic force (i.e. van der Waals force) between the tip and the surface causes the bending of the cantilever. This deflection is then measured optically (i.e. with the help of a laser) or electrically (i.e. by measuring a change in resistance) and converted into a height map of the surface, with a resolution of the order of the $\AA$. The scan mode used in this work is the tapping (or semi-contact) mode, which is an intermediate regime between contact and non-contact. In this mode, the cantilever tip oscillates at its resonance frequency tapping the sample and detaching. The vibrational amplitude is measured and kept constant with the aid of a feedback system, which changes the height of the cantilever accordingly. This scan mode is one of the most used since combines the advantages of contact and non-contact modes, while avoiding most of the disadvantages. In particular, it proves a very accurate height resolution avoiding the extended contact of the tip with the surface which shortens its lifetime. The resonant frequency of a cantilever depends on the square root of its spring constant, which in turn depends on the force acting on the cantilever (i.e. van der Waals forces on the tip) which changes depending on the distance from the sample. Therefore by measuring the oscillation frequency it is possible to determine sample topography.

The analysis of surface morphology can give complementary results to some other techniques (e.g. XRD, PL) in order to determine the crystal quality. In particular, a smooth surface is a hint that the growth was performed under optimal conditions, while a rough surface suggests that the growth parameters need further optimization. This is particularly important when optimizing the growth conditions of the GaN buffer layer, since a rough surface will have a negative impact also on the quantum wells which will be grown.

3.5 Photoluminescence

Photoluminesce (PL) is a fast and powerful characterization technique to investigate the radiative properties of semiconductors. It is particularly useful for LEDs since it can mimic the behavior of the device with optical injection of carriers, which doesn't require the processing of the device. Generally, in PL experiments a sample is irradiated with a laser and the radiation emitted is measured by a photodetector. Many information on carrier dynamics can be accessed with this technique by changing the type of measurements and the laser sources.

One of the most simple and fast PL measurements that can be performed is room temperature PL using a laser with the excitation energy larger than the material band gap. In this measurements, the laser radiation is absorbed by the material and produces electron-hole pairs which then recombine through radiative or non-radiative processes. Since this technique relies on the analysis of emitted radiation, only the e-h pairs which recombine radiatively (i.e emitting photons) can give information. In particular, in this work the first setup used consisted of a 10 mW HeCd continuous-wave laser with an emission wavelength of 325 nm and an Ocean Optics USB 2000 spectrometer as detector with a detection range going from 327 nm to 800 nm with 1380 reading channels. The emitted light is collected by an optic fiber and carried directly to the detector. The thickness of the material in which e-h pairs are generated can be estimated using Lambert-Beer law $I = I_0 e^{-\alpha x}$ where α is the absorption coefficient of the material at a given wavelength. In the case of GaN and an exciting wavelength of 325 nm, the thickness required to absorb 99% of the incident light is $\sim$ 370 nm, which is approximately the region that can be studied with this technique. Once

the e-h pairs are generated, they can diffuse before undergoing the recombination process. In order to recombine radiatively electrons and holes need to be located in the same spatial region, which implies that this process is efficient only where a high density of carriers is present in the same location. Since quantum wells are very efficient capturing and recombination centers, most of the carriers generated in the GaN barrier will be captured and recombine in the QWs. As a consequence this technique is particularly suited to study the luminescence properties of the nanostructures. However, not all the carriers are collected by the QWs since also defects are efficient capturing centers. Therefore, part of the emission spectrum may also be generated by defects-assisted radiative recombination. The light emitted with this process is very interesting since it can give information on the type of defects without having to perform complicated measurements [22]. Finally, also band-to-band recombination contributes to the emission spectrum.

When analyzing the emission spectrum of quantum wells, the most important parameters to calculate are the peak wavelength, the line width and the integrated intensity. To show how the analysis to extract these values is performed, in figure 3.2 it is shown the PL spectrum of a GaN/InGaN/AlGaN MQW sample. Before the measurements, the background emission was measured and automatically subtracted from the PL spectrum. Then, the peak wavelength of the spectrum is obtained by searching the maximum intensity and the FWHM is calculated by measuring the width of the peak at half peak intensity. The calculation of the integrated intensity is more complicated since in some cases a broad background emission can be generated by defects, as happens for the sample of figure 3.2. Therefore, to define a general procedure on how to delimit the integration interval, I have chosen the lowest intensity value for which the peak signal is above the background luminescence. This was done by tracing an horizontal line and increasing its value until when it intersects the spectrum in only two points, which are the boundaries of the integration interval.

Another analysis based on PL measurements is the calculation of the chromaticity coordinates. This measurement indicates the color properties of the emission spectrum and it is fundamental to characterize LEDs. This can be done by calculating the tristimulus values (i.e. X, Y and Z) based on CIE color matching functions using the formula:

$$X = \int_{\lambda} L(\lambda)\bar{x}(\lambda)d\lambda \tag{3.1}$$

where the integration interval is the visible spectrum (i.e. from 380 to 780 nm), L is the spectral radiance and $\bar{x}$ is the color matching function. To calculate also Y and Z it is necessary to substitute the respective color matching functions $\bar{y}$ and $\bar{z}$ in the formula 3.2. The calculated values of the tristimulus can then be used to compute the chromaticity coordinates (x,y), defined as:

$$x = \frac{X}{X + Y + Z} \tag{3.2}$$

$$y = \frac{Y}{X + Y + Z} \tag{3.3}$$

$$z = \frac{Z}{X + Y + Z} = 1 - x - y \tag{3.4}$$

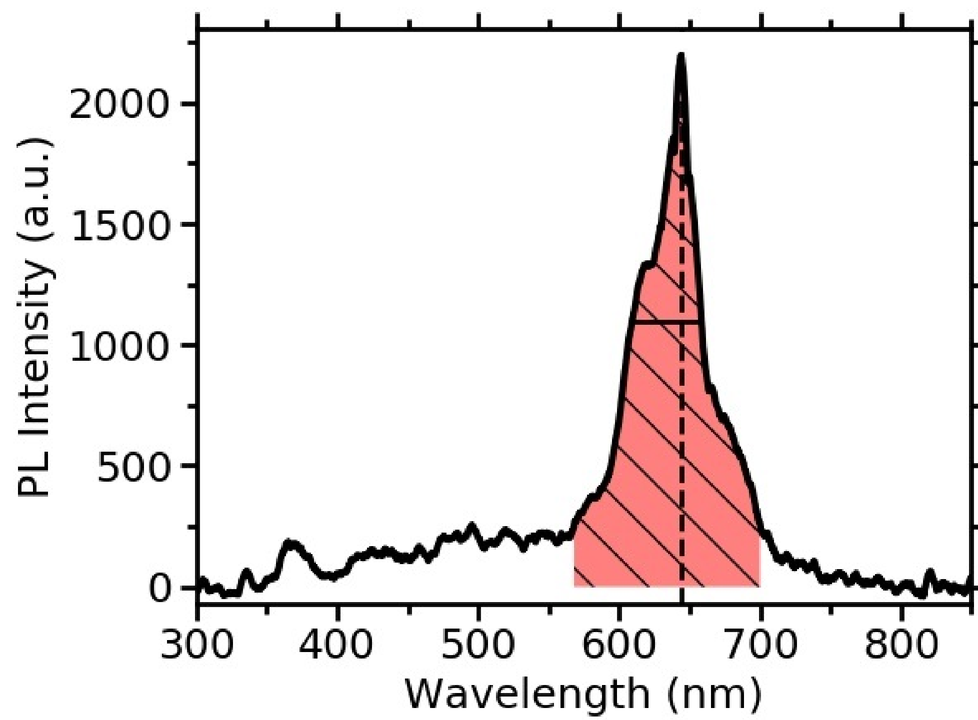

Figure 3.2: PL spectrum of an InGaN/AlGaN/GaN MQW sample. The filled area is the intensity of the emission peak, while the dashed black line shows the peak wavelength and the straight black line indicates the FWHM.

In this way it is possible to represent the chromaticity on a 2D plot known as CIE xyY color space, shown in figure 3.3

A color with its coordinates on the outer line of the diagram is called pure color. All the other colors inside the diagram can be obtained by mixing different pure colors. The two color spaces delimited by triangles (sRGB and Adobe RGB) represent the portion of the color space which can be accessed by mixing the red, green and blue colors of each vertex and represents the two standard color spaces typically used in modern displays. The possibility to reproduce these spaces requires the realization of an emitter with a color as close as possible to the coordinates of the vertices. The target of this work is to obtain red emission, which in the sRGB color space has (0.64, 0.33) coordinates.

The second setup used was able to perform PL as a function of temperature and power. A blue laser (100 mW at 405 nm) was focused on the sample at a 45° angle by means of an achromatic doublet with a focal length of 50 mm. The sample was placed in a cryostat able to reach the temperature of 15 K. The emitted radiation was collected normally to the sample and focused at the entrance of a monochromator with a focal length of 500 mm and dispersed by a 150 lines/mm grating and finally analyzed by a CCD. To prevent the diffused laser radiation from being detected, a long pass filter was used before the monochromator entrance. In this measurements, only InGaN QWs are able to absorb the incident radiation due to resonant excitation, therefore the portion of absorbed light is a fraction of the incident light and as a consequence the emitted intensity is much lower compared to the non resonant excitation. Moreover, there is no contribution to the PL spectrum from the surrounding barrier and its defects, which means that this setup is not suitable to study the emission properties of the whole structure and it is not a good setup to mimic the actual behavior of an LED. However, the possibility to study specifically the emission spectrum of the QWs as a function of temperature and power gives many information on the recombination properties [98].

3.6 X-Ray Diffraction

X-ray diffraction is one of the most powerful techniques used for crystal characterization. In this technique, a monochromatic beam of wavelength close to the lattice parameter is directed to the sample and the resulting diffraction pattern is collected with a detector. The mathematical description of the diffraction pattern is based on Bragg's law:

$$2d_{hklm}\sin\theta = n\lambda \tag{3.5}$$

with:

$$\frac{1}{d_{hkml}^2} = \frac{4}{3}\frac{h^2+hk+k^2}{a^2} + \frac{l^2}{c^2} \tag{3.6}$$

where h, k, m, l are the Miller indexes for an hexagonal crystal, a and c are the lattice parameters and θ is the angle between the incident beam and the surface. An important consequence of the Bragg law is that each point which satisfies eq. 3.6 must be a reciprocal lattice point, as demonstrated by von Laue. In his formulation, von Laue states that, given an incident wave vector $k_0 = \boldsymbol{n}/\lambda$ and a diffracted beam $k_h = \boldsymbol{n'}/\lambda$, constructive interference occurs only if the change in wave vector $\boldsymbol{S} = \boldsymbol{k_h} - \boldsymbol{k_0}$ is a reciprocal lattice vector. Using this formulation it is possible to construct the reciprocal space of a crystal starting from its

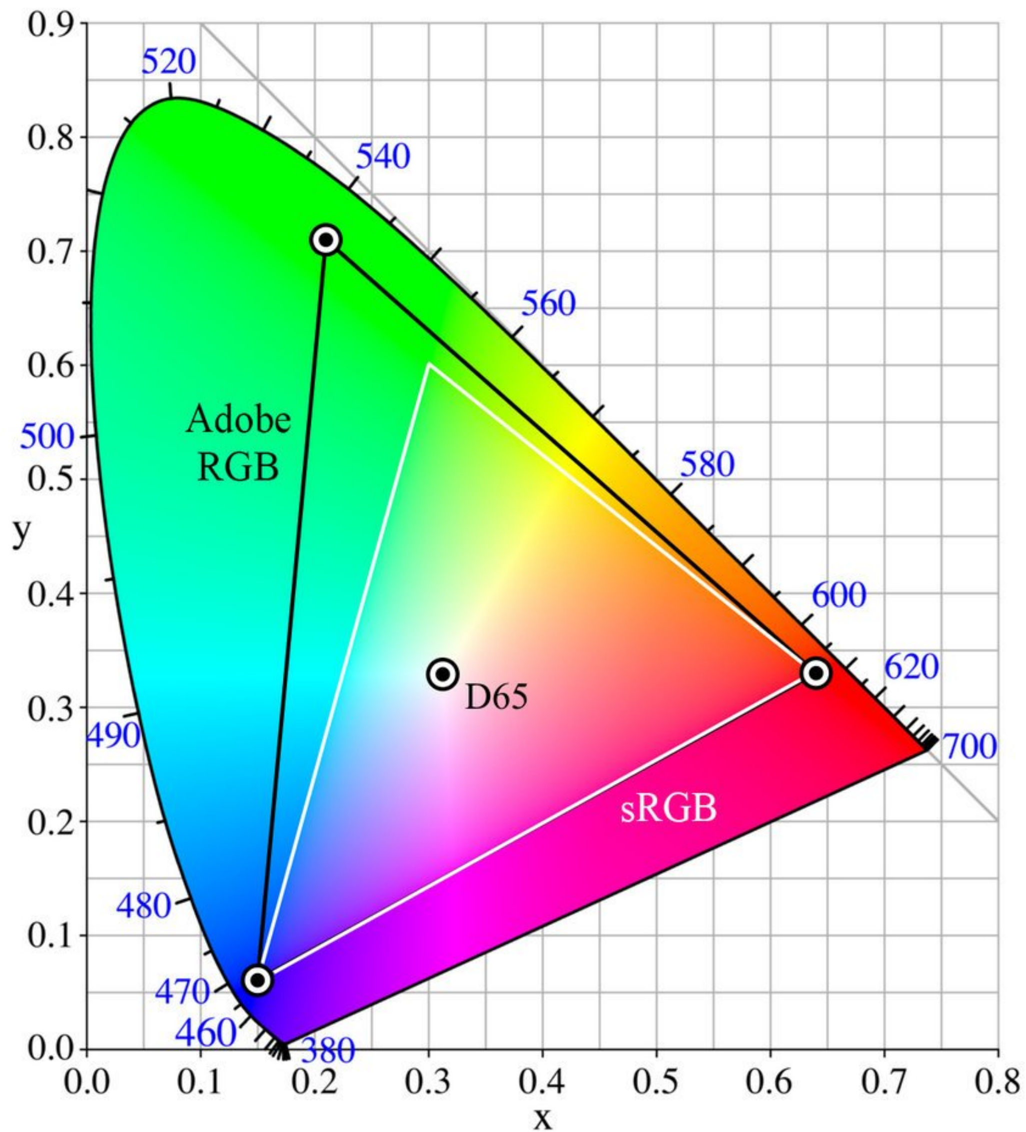

Figure 3.3: CIE 1931 chromaticity diagram. A color which lies on the border is a pure color, while a color which lies inside the diagram can only be obtained by adding different pure colors.The black triangle represents the Adobe RGB color space, which expands the sRGB space, while the point labeled D65 represents the coordinates of pure white.

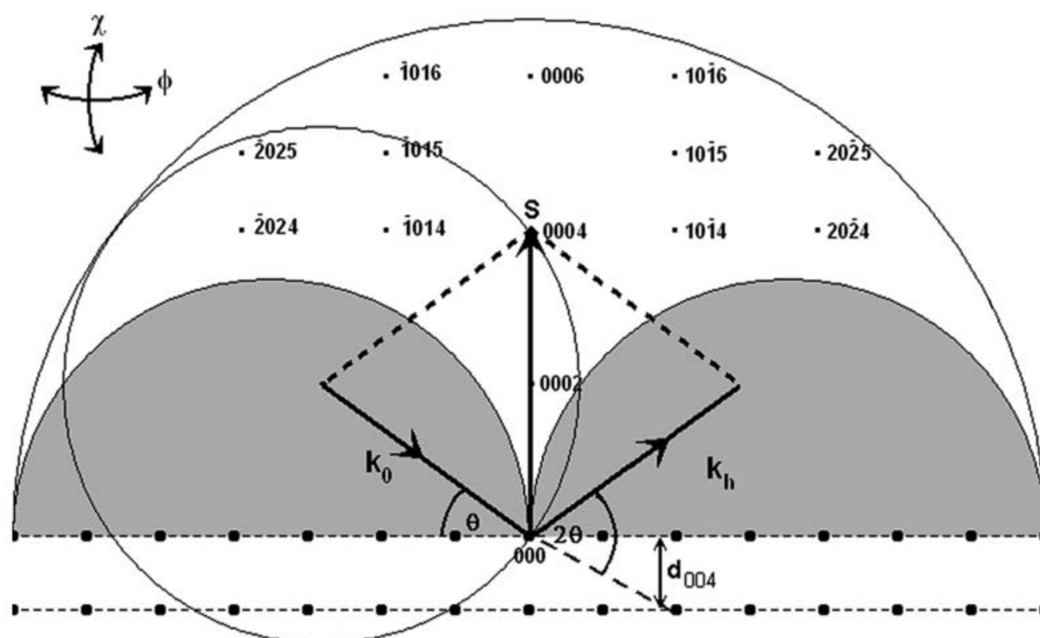

Figure 3.4: Reciprocal space of GaN [0001]. It is shown the von Laue construction of the (0004) plane and its Ewald sphere. The grey areas are inaccessible with a standard XRD geometry. From [99].

direct lattice. In figure 3.4 it is shown the reciprocal space of GaN [0001] with the von Laue construction of the (0004) plane. It is also indicated the corresponding Ewald sphere, which is the sphere touching the origin of k_0 with a radius $r = |\boldsymbol{k_0}|$ [99].

Typical XRD instruments use as incident beam the Cu K-α line, which corresponds to the radiation emitted by the relaxation of an electron from the 2s orbital to the 1s in a copper atom. The energy of this transition is 8.04 KeV (i.e. 0.64 $\mathring{A}^{-1}$) which fixes the magnitude of the incident and diffracted wave vectors k. The incident angle of the x-rays with respect to sample surface is generally called ω while the angle of detection is 2θ. Each point of the reciprocal space shown in figure 3.4 can be reached by changing the direction and the magnitude of the scattering vector $\boldsymbol{S}$. Changing the magnitude of S while keeping the inclination fixed can be done in an $\omega - 2\theta$ scan, where both incidence and detection angle are changed. If $\omega = 2\theta$ only the symmetric peaks (000l) can be probed, otherwise an offset is required to probe the asymmetric peaks. With an ω scan instead the magnitude of S remains constant while its direction changes by modifying the angle of incidence. By making $\omega - 2\theta$ scan for many different ω it is possible to construct a reciprocal space map (RSM). This measurement is the most complete one and it is possible to extract many information on crystal quality, strain and composition. In figure 3.5 are shown the directions of the reciprocal space measured with ω and $\omega - 2\theta$ scans, as well as the reciprocal space maps around two points.

As can be seen from the RSM of figure 3.5, reciprocal lattice points are asymmetrically broadened and assume an elliptical shape. This broadening is the convolution between instrument resolution, microstructural defects and macroscopic deformations. The horizontal broadening is caused by the limited lateral size of coherent domains, which is affected by dislocation density or by lateral strain and composition fluctuations. The vertical broaden-

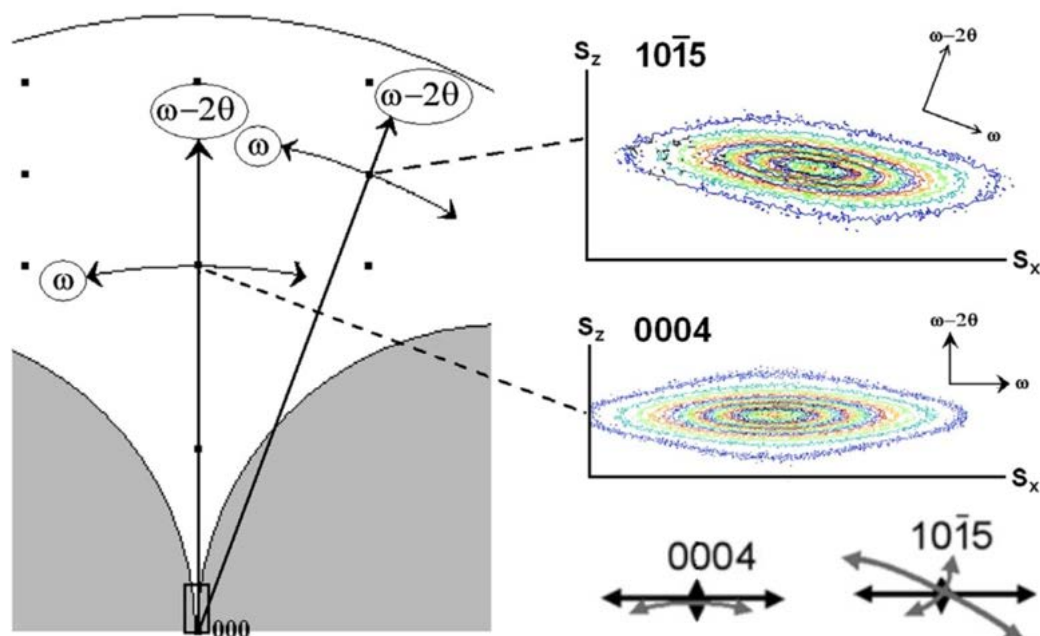

Figure 3.5: Directions of the reciprocal space measured with ω and $\omega - 2\theta$ scans for a symmetrical and an asymmetrical point. Are also shown reciprocal space maps of those points obtained by taking $\omega - 2\theta$ scans at many different ω. In the bottom right corner are shown the directions of the broadening affecting the symmetrical and the asymmetrical points. From [99].

ing is caused by the limited vertical thickness of coherent domains or by vertical strain and composition fluctuations. The broadening along the ω scan line is caused by mosaic tilt and screw component of dislocations. The broadening along the $\omega - 2\theta$ scan line is caused by mosaic twist and edge component of dislocations and it is visible only in a particular scan geometry (i.e. skew symmetric geometry). In this work the XRD used was a PANalytical X'Pert PRO equipped with a CCD detector and a four-crystal Ge [220] monochromator.

XRD is also particularly useful to study systems with multiple quantum well since many information about composition and thickness of the repeated layers can be obtained [100]. In order to perform this analysis, $\omega - 2\theta$ scan around the 0002 symmetrical peak is typically performed thanks to its higher intensity and it is measured using a high resolution detector (analyzer crystal). In figure 3.6 is reported the 0002 $\omega - 2\theta$ scan of a sample grown for this work with five GaN/InGaN/GaN QWs in which it is possible to see the presence of several diffraction peaks as well as the main GaN peak. In periodic structures, the beams reflected at the top and at the bottom of the stack interfere producing a diffraction pattern. This measurement is the equivalent of the reflectance (see section 3.2) with the difference that in this case the wavelength of the probing radiation is much lower. As a result, the pattern measured by XRD originates from the interference of much thinner layers. In particular, the position and spacing of the main satellite peaks is determined by the mean composition of the periodic structure and its thickness, their relative intensity is related to thickness ratio and the spacing of the intermediate peaks gives the total thickness of the structure [101,102].

One drawback of this technique is that the fitting parameters are the total thickness and the average composition of the structure. In order to obtain the thicknesses and compositions for the quantum well and barrier separately it is necessary to fit the measured diffrac-

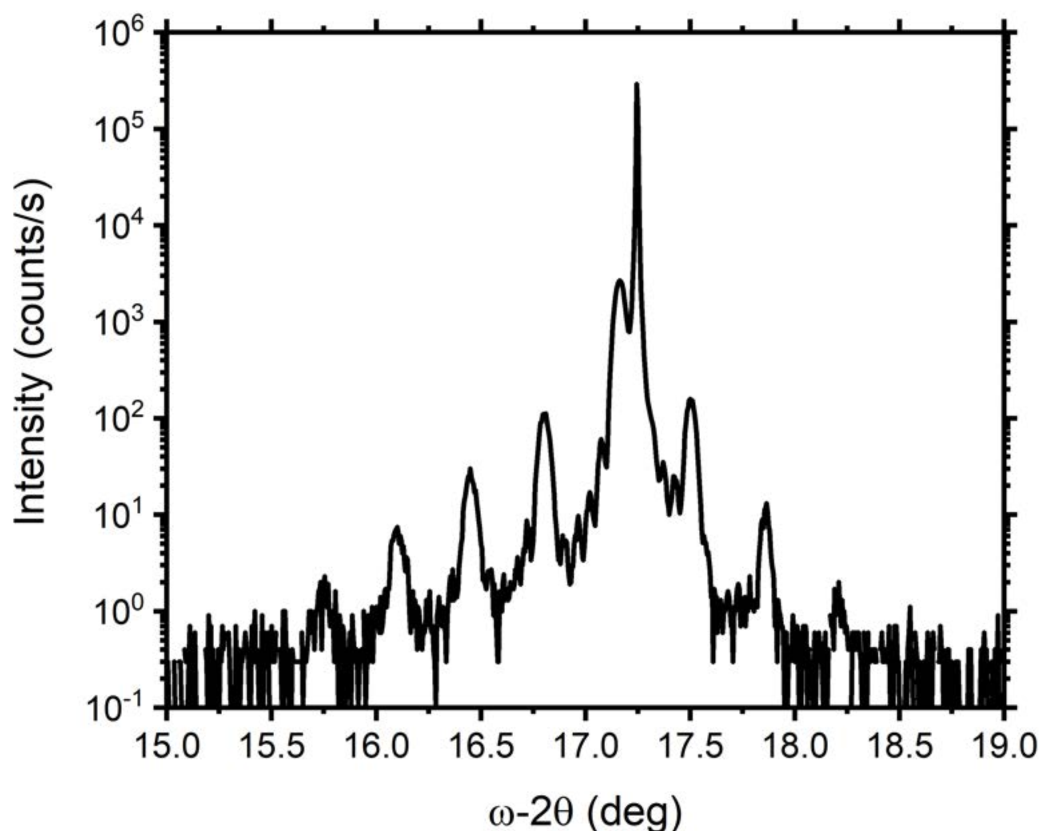

Figure 3.6: 0002 $\omega - 2\theta$ scan of an InGaN/GaN MQW sample. The best fit gave a QW thickness of 2.6 nm with 16% In content and a GaN barrier of 10.5 nm.

tion pattern. However, not always the fit is unique and therefore different combination of thicknesses and compositions may be possible due to the degeneracy of the parameters. To avoid this problem, complementary measurements can be required to narrow the parameters space. In the case of three different materials (i.e. barrier, well and cap) it is fundamental to fix some of the parameters by other measurements in order to extract meaningful information.

3.7 Simulations

Simulations are a very powerful method to understand the physical behavior of an LED. However, since the results are determined by the specific choice of simulation parameters, it is important to compare the results with the experiments in order to verify that the chosen parameter set gives reasonable results. This is particularly important when simulating III-Ns since in literature it is possible to find many different parameter sets which give different results.

In this work I focused on the simulation of the band structure and confined states in the QWs in order to study the recombination properties depending on the quantum well and capping layer structures. The tool used for these simulations is TiberCAD [103], a multi-physics and multiscale commercial software capable of combining classical and quantum

calculations. To study the quantum wells it is sufficient to make one dimensional simulations along the growth axis (i.e. [0001]) since in the xy plane the system con be considered as infinite and constant (i.e. can be treated as bulk). Since InGaN QW and AlGaN cap are grown pseudomorphically on GaN, which has a different lattice parameter, the strain in the structure has to be calculated first.

This is done by minimizing the elastic energy

$$E = \frac{1}{2} \int_{\Omega} C_{ijkl}(\boldsymbol{r}) \epsilon_{ij}(\boldsymbol{r}) \epsilon_{kl}(\boldsymbol{r}) d^3(\boldsymbol{r}) \tag{3.7}$$

where Ω is the lattice matched unit cell, C_{ijkl} is the elasticity modulus tensor and ϵ_{ij} is the strain tensor, defined as

$$\epsilon_{ij} = \frac{1}{2} \left(\frac{\partial u_i}{\partial x_j} + \frac{\partial u_j}{\partial x_i} \right) + \epsilon_{ij}^0 \tag{3.8}$$

where ϵ_{ij}^0 is the strain tensor between the unstrained and reference material. By minimizing equation 3.7 in all three directions, it is possible to obtain the displacement field $\boldsymbol{u}(\boldsymbol{r}) = \boldsymbol{r} - \boldsymbol{r'}$, with $\boldsymbol{r'}$ and $\boldsymbol{r}$ defined as the coordinates of a point before and after the deformation. In this definition, the displacement is calculated with respect to the reference lattice rather than to the unstrained material. As a consequence, applying this deformation to the mesh results in the matching of crystal lattices at the interface. A more detailed and rigorous derivation of the displacement field can be found in Ref. [104]. In general, strain can modify the shape of the energy bands. Moreover, the stretching of atomic bonds give rise to a polarization field, as discussed in chapter 1. In case of GaN/InGaN/GaN QWs, this piezoelectric field can be extremely large and has a severe impact on the quantum properties of the structures. The piezoelectric field can be calculated from the strain tensor using the formula

$$\boldsymbol{P}_{pz} = \begin{pmatrix} 0 & 0 & 0 & 0 & e_{15} & 0 \\ 0 & 0 & 0 & e_{15} & 0 & 0 \\ e_{31} & e_{31} & e_{33} & 0 & 0 & 0 \end{pmatrix} \begin{pmatrix} \epsilon_{xx} \\ \epsilon_{yy} \\ \epsilon_{zz} \\ \epsilon_{yz} \\ \epsilon_{xz} \\ \epsilon_{xy} \end{pmatrix} = \begin{pmatrix} e_{15}\epsilon_{xz} \\ e_{15}\epsilon_{yz} \\ e_{13}(\epsilon_{xx} + \epsilon_{yy}) + e_{33}\epsilon_{zz} \end{pmatrix} \tag{3.9}$$

where e_{ij} are the components of the piezoelectric tensor and ϵ_{kl} are the components of the calculated strain tensor (the Voigt notation is used) [9, 105]. In particular, considering the [0001] direction as the growth axis, equation 3.9 simplifies to $\boldsymbol{P}_{pz} = P_{pz}^z = e_{13}(\epsilon_{xx} + \epsilon_{yy}) + e_{33}\epsilon_{zz}$. The total polarization field in the structure is then obtained as the sum of the spontaneous (also called pyroelectric) and piezoelectric polarization.

To calculate the energy bands, the Schrödinger equation is solved for the whole structure using the $\boldsymbol{k}\cdot\boldsymbol{p}$ method. With this method it is possible to simplify the electronic Hamiltonian and obtain the analytic expression of the band dispersion around the high-symmetry points. With this approach, the kinetic term of the Hamiltonian can be written as $(\hbar\boldsymbol{k} + \boldsymbol{p})^2/2m$ and the wave function can be simplified to the periodic part of the Bloch wave, which does not depend on the spatial coordinate. This new equation can be solved assuming a small k vector (i.e. close to a high symmetry point) and applying the perturbation theory.

The resulting eigenvalues can be used to define the effective mass, which in general is a 3×3 tensor representing the masses that carriers appear to have in the crystal. This tensor includes all the information connected to the material and its band structure. In the $\boldsymbol{k} \cdot \boldsymbol{p}$ framework, the effective mass tensor is related to the carrier masses by the equation

$$\frac{1}{m*} = \frac{1}{m} + \frac{2}{m^2 k^2} \sum_{n' \neq n} \frac{|\langle u_{n0}|\boldsymbol{k} \cdot \boldsymbol{p}|u_{n'0}\rangle|^2}{E_{n0} - E_{n'0}} \tag{3.10}$$

where u_{n0} are the non-degenerate eigenfunctions and the summation is on the different energy bands, each weighted over the energy difference with the reference band. The same results can be extended to an heterojunction by assuming a position dependent effective mass and by adding a non-periodic potential term in the Hamiltonian to take into account the band discontinuity at the interfaces.

Carrier dynamics is then described by solving drift-diffusion equations. The system of equations consists of a Poisson equation and two continuity equations for electrons and holes:

$$\begin{cases} -\nabla(\epsilon\nabla\phi - \boldsymbol{P}) = -e(n - p - N_d^+ + N_a^-) \\ -\nabla(\mu_n n \nabla\phi_n) = R \\ -\nabla(\mu_p p \nabla\phi_p) = -R \end{cases} \tag{3.11}$$

where ϵ is the permittivity of the material, ϕ is the electric potential, $\boldsymbol{P}$ is the electric polarization, n and p are electrons and holes density respectively, N_d^+ and N_a^- are the densities of ionized donor and acceptors, μ is carrier mobility and R is the net recombination rate.

To compute the confined energy levels in the nanostructure, some approximations are required due to the complexity of the system. Considering the non-periodic potential as a slowly varying perturbation, the electron wave function can be expressed as a linear combination of the solutions of the unperturbed system (i.e. Bloch waves). To make this approximation more accurate, the contribution of different bands has to be taken into account. In this work were considered three hole states (i.e. HH, LH, SO) and one conduction state, each with the two spin components giving a total of eight bands. After some rearrangements, the wave function can be written as the product of the rapidly changing component of the Block wave and a slowly varying modulation called envelope function. The Hamiltonian then applies only to the envelope function and can be solved to obtain the eigenvalues and eigenfunctions of the quantized system.

The emission properties can be studied by considering the process as a carrier-photon scattering. This approach is more accurate than just considering electron-hole overlap since it includes the interaction with light, which can not be neglected. The complete wave function which has to be considered is made of the obtained envelope function ψ multiplied by the rapidly varying part of the Bloch wave u. The optical matrix element between the initial state $\psi_i u_i$ and the final state $\psi_f u_f$ is

$$\langle\psi_f u_f|\hat{\boldsymbol{H}}|\psi_i u_i\rangle = \langle u_f|\hat{\boldsymbol{H}}|u_i\rangle_{cell}\langle\psi_f|\psi_i\rangle + \langle\psi_f|\hat{\boldsymbol{H}}|\psi_i\rangle\langle u_f|u_i\rangle_{cell} \tag{3.12}$$

where $\hat{\boldsymbol{H}}$ is the time-dependent perturbation which represents carrier-photon scattering and it is equal to $e/m^* \boldsymbol{A} \cdot \boldsymbol{p}$ with $\boldsymbol{A}$ the vector potential of the electromagnetic field and $\boldsymbol{p}$ the momentum operator. In the case of interband transitions, which are the topic of this

work, the second term of equation 3.12 is zero due to the orthogonality of Bloch waves from different bands. Therefore, the optical matrix element is determined by the envelope function overlap $\langle \psi_f | \psi_i \rangle$ multiplied by a constant factor for the ground state transitions [106].

The parameters used for the simulations are reported in table 3.1.

From literature it is well know that for ternary nitride alloys a bowing parameter has to be considered to obtain the correct band gap energy [107, 110–113]. However, there is no agreement on which are the best parameters to be used. Therefore in this work I decided to use the ones proposed by Vurgaftman [107], since these are the most commonly used. The chosen bowing parameters are 1.4 eV and 0.7 eV for InGaN and AlGaN respectively. The review paper of Vurgaftman was also used as main reference for all the parameters reported in table 3.1 except for piezoelectric constants, which were taken from [108], and valence band offsets, taken from [109]. The values proposed in those papers were chosen because they were calculated specifically for wurtzite structures. The simulation results obtained using the chosen parameter set was then compared to experimental data to verify the agreement.

Parameters	GaN	AlN	InN
a ($\AA$)	3.189	3.112	3.544
c ($\AA$)	5.185	4.982	5.718
Eg at 0 K (eV)	3.510	6.25	0.78
α (meV/K)	0.909	1.799	0.245
β (K)	830	1462	624
VBO (eV)	1.28	0	2.39
Δ_{cr} (eV)	0.010	-0.169	0.040
Δ_{so} (eV)	0.017	0.019	0.005
$m_e^{\parallel}$	0.20	0.32	0.07
$m_e^{\perp}$	0.20	0.30	0.07
A_1	-7.21	-3.86	-8.21
A_2	-0.44	-0.25	-0.68
A_3	6.68	3.58	7.57
A_4	-3.46	-1.32	-5.23
A_5	-3.40	-1.47	-5.11
A_6	-4.90	-1.64	-5.96
a_1 (eV)	-4.9	-3.4	-3.5
a_2 (eV)	-11.3	-11.8	-3.5
D_1 (eV)	-3.7	-17.1	-3.7
D_2 (eV)	4.5	7.9	4.5
D_3 (eV)	8.2	8.8	8.2
D_4 (eV)	-4.1	-3.9	-4.1
D_5 (eV)	-4.0	-3.4	-4.0
D_6 (eV)	-5.5	-3.4	-5.5
C_{11} (GPa)	390	396	223
C_{12} (GPa)	145	137	115
C_{13} (GPa)	106	108	92
C_{33} (GPa)	398	373	224
C_{44} (GPa)	105	116	48
e_{31} (C/m^2)	-1.863	-2.027	-1.63
e_{33} (C/m^2)	1.020	1.569	1.238
P_{sp} (C/m^2)	1.312	1.351	1.026

Table 3.1: Simulation parameters used in this work which were taken from [107–109].

4

MOVPE Growth Optimization

In the first part of this work are reported the results obtained during the optimization of GaN/InGaN/(Al)GaN QWs grown by MOVPE. The emission properties were studied and compared in order to find the best growth parameters. MOVPE was chosen as the growth technique since it is the most established technique for the growth of these structures, allowing to obtain the best crystal quality.

4.1 GaN on Sapphire Template Growth

In this work 2" wafers of c-plane sapphire were used as substrates. On each substrate, a $\sim$1.8 μm thick GaN buffer layer was grown to obtain a GaN template. Due to the large lattice mismatch between GaN and sapphire, an initial nucleation layer is required to improve the quality of the epilayer and prevent cracking. The most common approaches reported in literature make use of an AlN layer [17] or a low temperature GaN nucleation layer [18]. The procedure used in this work to obtain a high quality GaN buffer layer is based on the LT-GaN nucleation layer technique described in section 1.2.

After an initial thermal baking of sapphire at 1150°C under ammonia, the temperature was lowered to 550°C to grow the LT-GaN nucleation layer. The GaN layer was deposited in 5 minutes with a TMGa flux of 12 sccm and a NH_3 flux of 5 slm. After this deposition, the temperature was raised up to 1100°C with only NH_3 flowing. After waiting for 3 minutes at this temperature, 29 sccm of TMGa were supplied for 60 minutes, resulting in $\sim$1.8 μm GaN. During this growth, the carrier gas used was H_2.

In figure 4.1 it is shown a 5x5 μm AFM image of a template grown following this procedure. As can be immediately seen, the surface morphology is extremely smooth with an evident step-flow growth mode. The measured roughness rms is $\sim$170 pm. From the figure it is possible to note some dark spots, which are the V-pits typically found at the termination of threading dislocations. The dislocation density measured by cathodoluminescence was found to be in the low 10^8 cm^{-2} range.

Once the GaN template was completed, each wafer was cut into square pieces with a lateral size of approximately 2 cm.

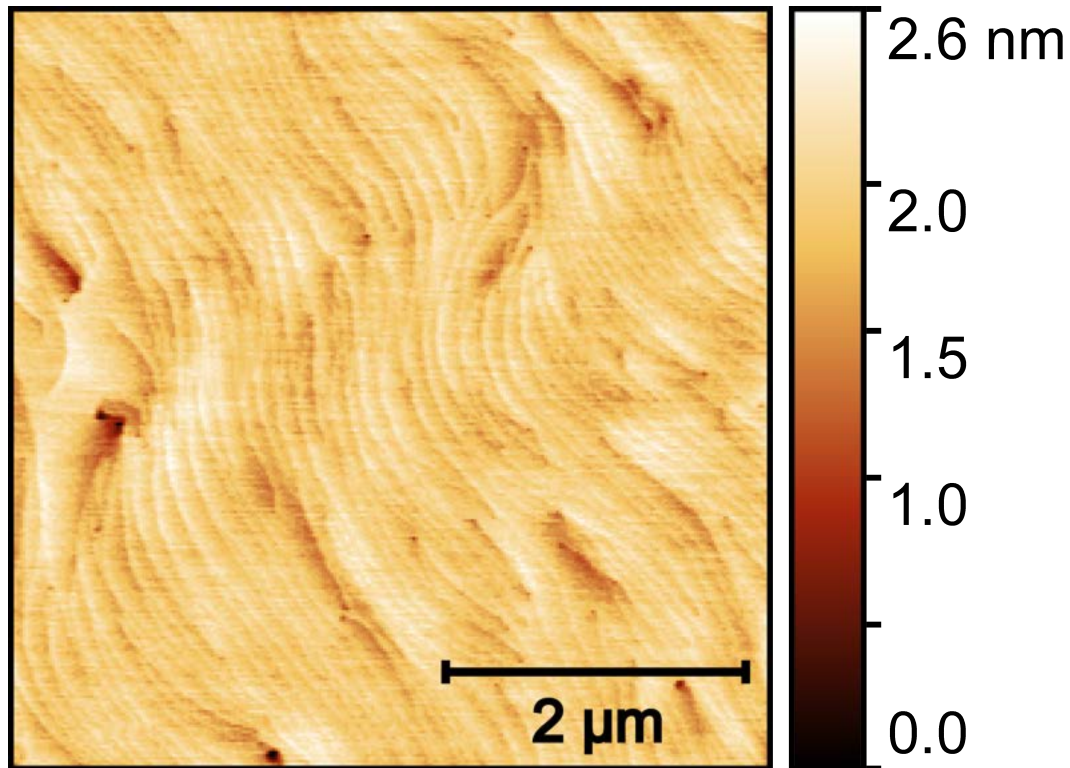

Figure 4.1: 5x5 μm AFM scan of a GaN template. The measured roughness is $\sim$170 pm.

4.2 Growth of the Quantum Structures

Before choosing the growth sequence and growth parameters to be used for the QWs, it is important to decide the desired thickness of the structures, which influences the electrical and optical properties of the device. As previously discussed in section 1.5, the emission wavelength is influenced by QW thickness and composition. In particular, increasing the thickness leads to an energy reduction of the confined states together with a larger spatial separation of the wave functions due to QCSE. On the other hand, increasing the indium content decreases the emission energy and increases the wave function overlap. However, it becomes difficult to grow a high indium-content InGaN without increasing defects density as well [35]. Based on these considerations, the targeted QW thickness is between 3 nm and 4 nm with an indium content between 20% and 25%, which should allow to emit at long wavelength with a limited amount of indium . Also the barrier thickness is important, since it affects the injection properties of the LED. A thick barrier increases the threshold voltage while a thin one may lead to a coupling of the QW states. In this case, the targeted GaN barrier thickness was approximately 10 nm, which is the value typically used in the literature [2, 43, 114], .

The growth sequence chosen for the quantum structures, shown in figure 2.2, is based on the Q2T approach of ref. [86] described in section 2.1.3, in which the capping layer is grown at the same temperature of the QW in order to improve interface smoothness and avoid indium segregation and desorption at the surface, while the barrier is grown at higher temperature to improve the crystal quality. The precursors used to grow the QWs and

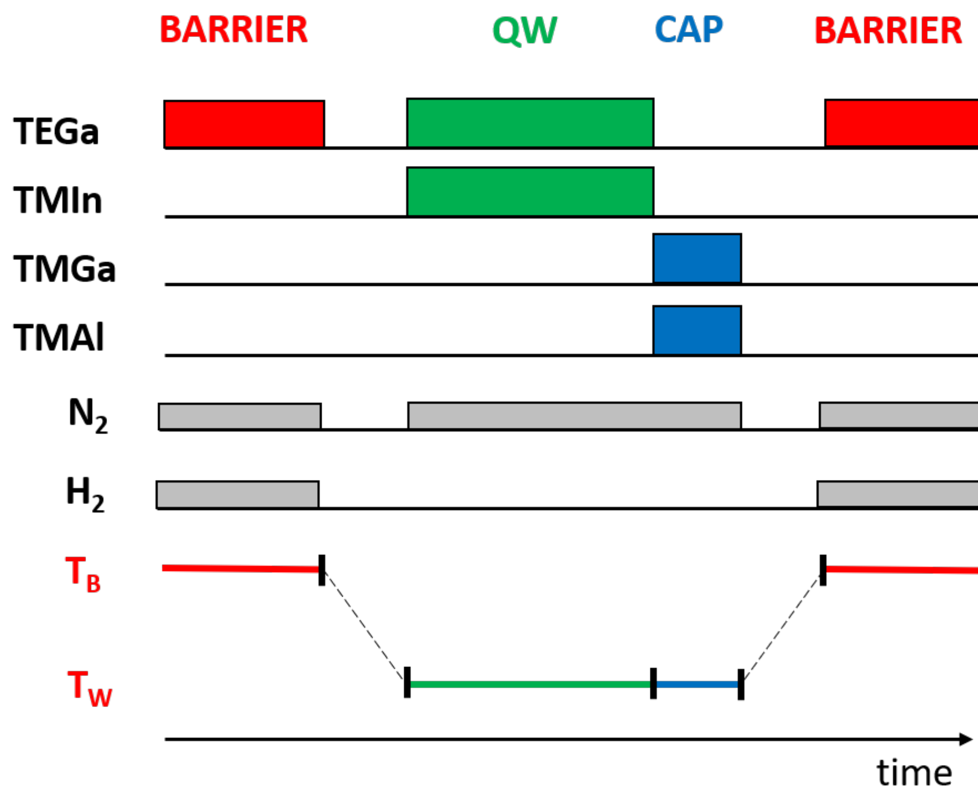

Figure 4.2: Representation of the quantum structure growth sequence used in this work. This sequence was repeated five times to obtain the MQW samples.

barriers were chosen based on the arguments discussed in section 2.1.2. The best choice for the gallium precursor is TEGa, which was used for the QW and the barrier. The choice of using TMGa to grow the capping layer, even if not optimal due to the low temperature used, was done in order to reduce the negative effect of the growth interruption on the quantum well. It is well known that interrupting the growth just after the deposition of the QW has detrimental effects on indium incorporation and interface sharpness [86, 115]. Since only one TEGa bubbler was available in the used MOVPE system and it was already used for the QW, TMGa was used for the capping layer. On top of that, the larger vapor pressure of TMGa allows for a faster covering of the surface, decreasing the exposure time of InGaN. This choice was also made in order to avoid turbulence related to a rapid variation in the flow and to have more possibilities to change the Ga/Al vapor pressure ratio. Since TMGa has a large vapor pressure, a low carrier flow is required to have a low growth rate. However it is better not to reduce the flow below 1% of the total capability of the MFC (i.e. 500 sccm for the used MFCs) in order to have a precise control over the flow. Therefore, I decided to use a TMGa flow of 4 sccm. Moreover, TEGa and TMAl can have a strong parasitic reaction in the gas phase, with a negative impact on the growth. The AlGaN layer has to be grown at low temperature following the Q2T growth sequence. This implies that the AlGaN capping layer can not be grown under optimal conditions [46, 50, 59]. Moreover, the use of TMGa at low temperatures leads to a higher carbon incorporation (see section 2.1.2) which contributes to the formation of point defects. However, this choice permits to grow the QW under optimal conditions which I prioritized over having a higher quality of the capping layer. The addition of hydrogen (1% of the total gas flow) to the nitrogen carrier gas during the growth of the barrier layer was done in order to remove the possible indium residues floating on the surface and to improve the sharpness of the interface [86, 115]. Indeed, as discussed in section 2.1.2, a large concentration of hydrogen in the atmosphere hinders indium incorporation in the growing film. Finally, the NH_3 flow was kept fixed at 5 slm for all the samples.

4.2.1 InGaN Quantum Well Optimization

Before growing the QWs, an initial buffer layer was grown on top of the template in order to bury the surface defects. To do so, GaN was grown at 1100°C for 3 minutes with a TMGa flux of 29 sccm and a NH_3 flux of 5 slm, resulting in approximately 100 nm thick layer. After that, the growth of the nanostructures was initiated with the growth of a GaN barrier.

To optimize the growth of the structure, I started by studying the effects of several growth parameters on the quantum well structural and emission properties. To avoid spurious effects and to improve the reliability of the XRD analysis, the grown structure consisted of five stacks of GaN/InGaN/GaN QWs. This choice was made in order to have a sufficiently high signal without increasing too much the growth time. The initial choice of growth parameters was based on previous attempts to grow green GaN/InGaN/GaN QWs and are reported in table 4.1.

The first parameter studied was the QW growth temperature (T_W). In this set of samples, all the other parameters were kept fixed, as can be seen from table 4.1, while T_W was set at 700°C, 720°C, 735°C and 750°C. The XRD analysis determined a QW thickness of $\sim$2.5 nm with an indium content ranging from 7% to 24% from higher to lower growth temperature respectively and a barrier thickness of $\sim$11 nm. However, the XRD interference patterns of the samples grown at 750°C and 735°C were not sharp, suggesting a lower qual-

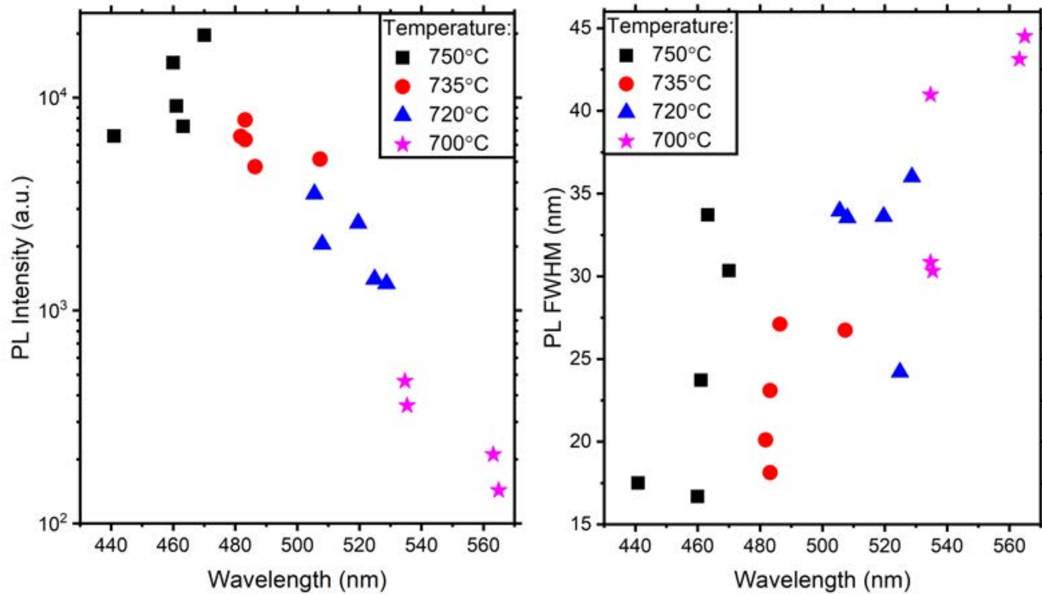

Figure 4.3: a) PL integrated intensity and b) FWHM as a function of emission wavelength. Decreasing the growth temperature results in a longer emission wavelength and larger emission line width with a decrease in the emission intensity.

ity of the InGaN QWs as well as a low reliability of the XRD analysis for those samples. In any case, this result demonstrates that indium incorporation is strongly dependent on growth temperature [60, 80], as was already discussed in section 2.1.3. On the other hand, the measured thickness does not seem to depend strongly on the growth temperature, indicating that the growth is carried out under the transport-limited regime apart from indium which is probably limited by the desorption process.

The measured PL intensity and line width are shown in figure 4.3. For each sample, the PL spectra were taken in five different spots (in the center and slightly off towards each corner) to take into account also the macroscopic non-uniformities of the sample. As can be seen, even if there is some scattering of the points within each sample, the general behavior follows an exponential reduction of intensity with decreasing growth temperature. This result is in agreement with what can be found in literature about the efficiency droop [3]. At the same time, decreasing the growth temperature results in an increase of the PL FWHM, which is typically attributed to an increased disorder of the system. At this stage of the work, the target is to have a quantum well emitting in the green-yellow region with a high intensity and narrow line width to use it as a starting point to grow and optimize the AlGaN capping layer. Based on the obtained results, the best growth temperature was 720°C. This sample was a good compromise between sample quality and high growth temperature. The measured thickness of the QW is 2.5 nm with an indium content of 21%.

Since the obtained QW had a thickness below the target of 3-4 nm, the following sample was grown increasing the QW deposition time by $\sim$33%. The results obtained from the XRD analysis of this sample showed a QW thickness of 3.3 nm with an unchanged In concentration of 21%. The comparison of the PL spectra is shown in figure 4.4. It is possible to see that the emission wavelength shifted from 515 nm to 557 nm with a substantial decrease in intensity, while the emission line width increased from 34 nm to 42 nm. This

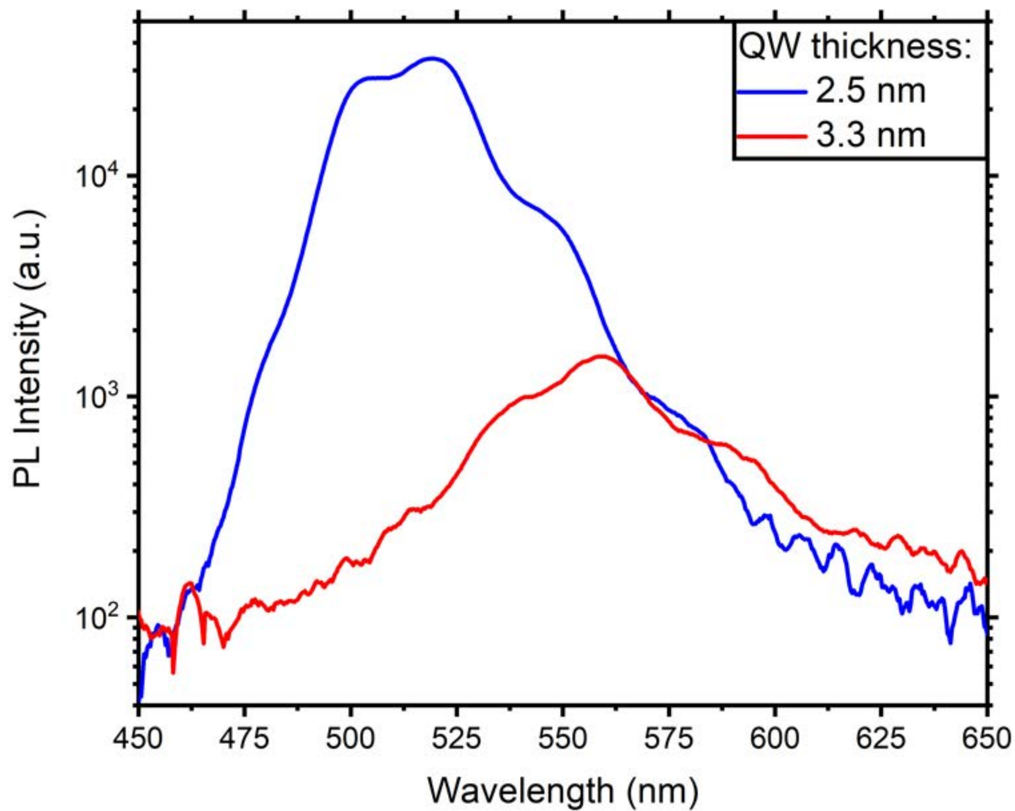

Figure 4.4: PL spectra of two samples in which only the QW deposition time was changed, resulting in different thicknesses.

difference in emission properties can be attributed to the change in QCSE due to the larger polarization field.

Next, I studied the influence of In/Ga ratio by changing TMIn flow between 25,50 and 75 sccm while keeping TEGa fixed at 8 sccm. The growth parameters are reported in table 4.1. To understand how the indium incorporated is affected by the change in TMIn flow it is useful to consider the variation of the product between In composition and QW thickness. The value of this parameter is obtained directly from the fit of the XRD interference pattern (see section 3.6) and it is more reliable than extracting QW thickness and composition of each sample due to the degeneracy of the fitting parameters. This gives the values of 0.54 nm, 0.69 nm and 0.80 nm for the TMIn fluxes of 25 sccm, 50 sccm and 75 sccm respectively. It is evident that the increase in the In flux does not result in a similar increase in indium incorporation. Indeed, doubling the TMIn flow results in a 27% increase in indium incorporation and increasing it by three times results in an increase of 48%. This is because the In incorporation is limited by the desorption process in this temperature range. The In and Ga atoms reaching the surface form a metal layer before being incorporated in the growing film. The composition of this layer is mostly determined by the desorption of the adatoms. Since the desorption process has an exponential dependence on temperature, increasing linearly the In partial pressure does not shift significantly the equilibrium. In figure 4.5 PL intensity and line width are reported as a function of emission wavelength for the three samples. The results show an in increase in emission wavelength and line

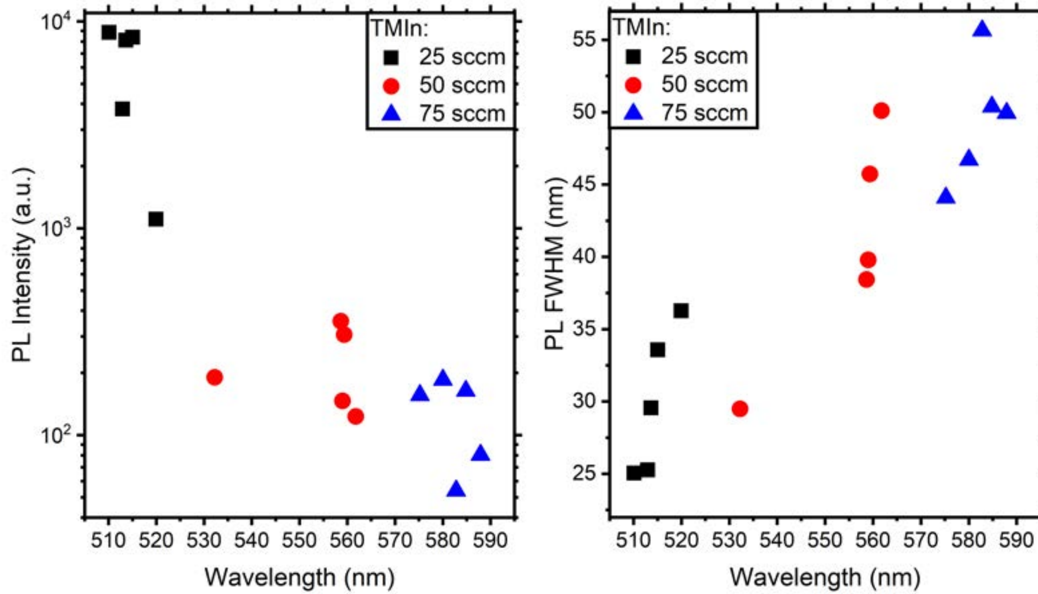

Figure 4.5: a) PL integrated intensity and b) FWHM as a function of emission wavelength for different TMIn flows. Higher flow leads to a higher emission wavelength, a larger line width and a reduction in emission intensity.

width with increasing TMIn flow. Trying to extract the thickness and composition of the QWs, the change in emission wavelength between the samples grown with 25 sccm and 50 sccm of TMIn seems to be related to an increase in the In content. On the other hand, the redshift observed when the TMIn flow was increased from 50 sccm to 75 sccm seems to be related to an increase in the QW thickness with no substantial change in In concentration. A possible explanation for this result is that the indium in excess floating on the surface was partly incorporated in the initial layers of the barrier, resulting in an effective increase in the QW thickness. Interestingly, the In concentration in the QW is the same as in the case with a TMIn flow of 50 sccm, supporting the assumption of the incorporation being temperature-limited. Based on the above discussion, the best TMIn flow was 50 sccm since it guaranties the highest In composition with a limited incorporation in the capping layer.

Another growth parameter which has a strong influence on QW emission properties is the growth rate. For this series the best sample obtained from the previous calibration was taken as reference, which was grown with a rate of 1 nm/min. For this series the growth rate was taken as half (0.5 nm/min) and double (2 nm/min) the one of the reference sample by changing both TMIn and TEGa flows, as shown in table 4.1. The PL results are shown in figure 4.6. Increasing the growth rate leads to an higher indium incorporation since the increased In vapor pressure slows down the desorption process and enhances the incorporation in the growing film. Moreover, the faster covering of the surface results in a shorter desorption time for In adatoms. At the same time, the mean free path of adatoms on the surface is reduced leading to a lower crystal quality and a higher disorder. This can be seen by looking at the emission FWHM when growing at 2 nm/min, which is more than doubled compared to the sample grown at 1 nm/min. On the other hand, decreasing the growth rate leads to a shorter emission wavelength together with a decrease in PL line width, as can be seen from figure 4.6. In this case, indium incorporation is reduced due to the lower vapor

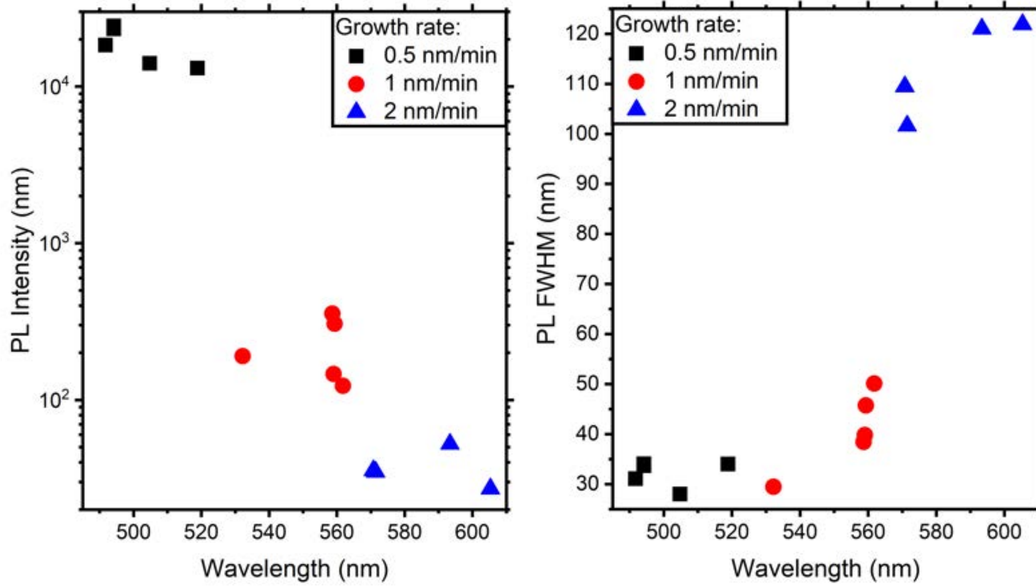

Figure 4.6: a) PL integrated intensity and b) FWHM as a function of emission wavelength as a function of growth rate. Higher growth rate leads to a higher emission wavelength and a significant increase in crystal disorder. On the other hand, decreasing the growth rate reduces emission wavelength.

pressure which in turn enhances the desorption of In adatoms. On top of that, the longer time required to grow a monolayer results in an increased indium desorption. Also the resulting disorder of the InGaN layer is reduced due to the lower indium concentration and the higher adatoms mean free path which allows to find better nucleation sites. However, even if the quality of this sample was greater, the too short emission wavelength made me choose the growth rate of 1 nm/min as the best growth condition for this application.

As a conclusion, the best growth parameters to grow the InGaN quantum well are reported at the end of table 4.1.

Sample series	Structure	Temperature (°C)	Deposition time (min)	TEGa flux (sccm)	TMGa flux (sccm)	TMIn flux (sccm)
QW temperature	Barrier	850	9	8	-	-
	QW	750 / 735 / 720 / 700	2:30	8	-	50
	Capping	750 / 735 / 720 / 700	1	-	4	-
In/Ga ratio	Barrier	850	9	8	-	-
	QW	720	2:30	8	-	25 / 50 / 75
	Capping	720	1	-	4	-
QW growth rate	Barrier	850	9	8	-	-
	QW	720	1:40 / 2:30 / 6:40	16 / 8 / 4	-	100 / 50 / 25
	Capping	720	1	-	4	-
Best parameters	Barrier	850	9	8	-	-
	QW	720	2:30	8	-	50
	Capping	720	1	-	4	-

Table 4.1: Growth parameters used for the quantum well optimization. The best parameters chosen for each sample series are indicated in red.

4.2.2 AlGaN Capping Layer and GaN Barrier Optimization

To optimize the AlGaN capping layer and the GaN barrier, the principal characterization technique used was photoluminescence. As explained in section 3.6, the use of XRD to determine the structural parameters of multiple layers of different materials is not reliable due to the degeneracy of the fitting parameters. However, at this stage photoluminescence gives enough information on which is the effect of the capping layer on emission properties, provided that one knows the characteristics of the GaN/InGaN/GaN QW used. The initial choice of growth parameters for the AlGaN capping layer is reported in table 4.2.

The first GaN/InGaN/AlGaN sample was done by adding TMAl during the capping layer growth sequence of the best GaN/InGaN/GaN sample obtained before (see section 4.2.1). The deposition time of the capping layer was then increased from 60 s to 90 s and 120 s to study the influence of deposition time on the emission properties, as reported in table 4.2. The obtained PL results are shown in figure 4.7, in which emission intensity and line width are expressed as a function of wavelength. As can be seen, adding aluminum to the capping layer results in an increase of the emission wavelength. The main reason for this effect is the increased QCSE due to the larger polarization charges at the InGaN/AlGaN interface compared to the InGaN/GaN, resulting in the redshift of emission wavelength as discussed in sections 1.6 and 1.8. Increasing the AlGaN deposition time resulted always in a longer emission wavelength until the quality of the grown material degrades. In this last case, the emission consisted of a very broad peak centered around 570 nm with a FWHM larger than 100 nm. The emission properties of this peak are compatible to the yellow luminescence band discussed in section 1.3, characterized by an emission energy of 2.2-2.3 eV and a FWHM at room temperature between 0.4 eV and 0.5 eV [22]. This broad band was never observed clearly in the previous samples. The origin of this emission could be defects in the AlGaN layer or in the GaN barrier. Carriers, which previously were not encountering these defects, are now captured due to the increased electric field which may cause a redistribution of electrons and holes (see chapter 6).

It is clear from figure 4.7 that the sample grown with 90 s of AlGaN deposition time has the best emission properties with a PL peak in the red spectral range and a narrow line width. Since the emission properties of this sample match the target of this work, I proceeded by making a complete characterization of the structure with XRD and TEM. The RSM of that sample, taken around the asymmetric (10-15) point, is reported in figure 4.8, where it is possible to see the satellite peaks originating from the repeated quantum structure as well as the main GaN peak. From the image it is possible to see that all the maxima of the intensity are almost aligned vertically with very similar reciprocal lattice unit. This indicates that the structure is coherently stained with respect to the GaN substrate, with a very low degree of relaxation. To have an exact measure of the thickness of the structure, a TEM image, shown in figure 4.9, was taken on a different sample grown following the exact growth procedure as the best one. From the image it is possible to notice that the QWs interfaces are quite sharp, especially the bottom ones. The upper ones instead have more intermixing due to the indium tail problem described in section 2.1.3. It is also clear that the disorder in the crystal increases with the QW number, probably due to strain accumulation or due to a non perfect flattening of the surface after each QW stack. The mean values of the measured thicknesses are 3.5$\pm$0.3 nm for the QW, 12.8$\pm$1.2 nm for the capping layer and 6.0$\pm$0.8 nm for the barrier. Since the only parameter changed in this set of samples was the capping layer deposition time, it is possible to estimate the capping layer thickness of all

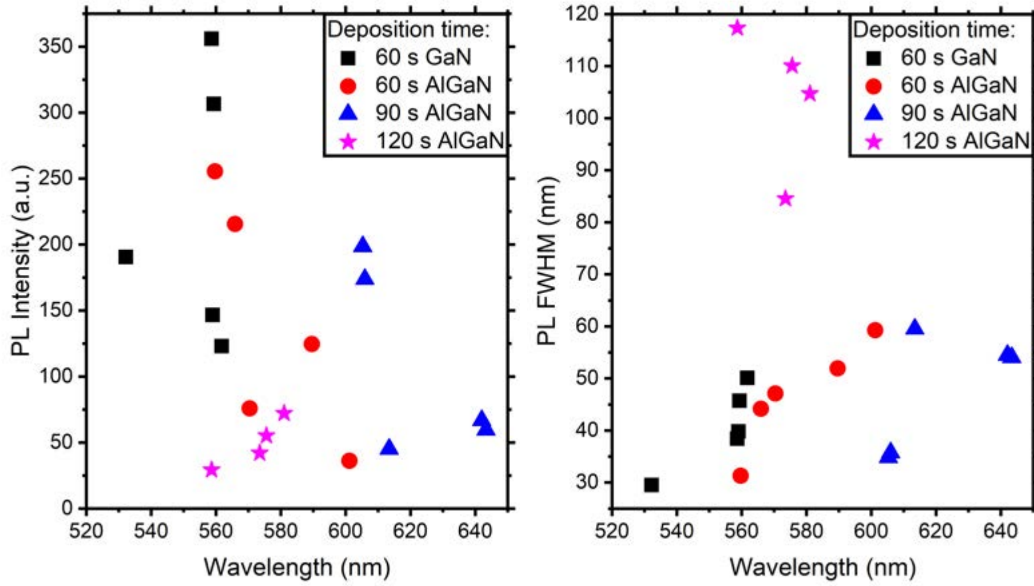

Figure 4.7: a) PL integrated intensity and b) FWHM as a function of emission wavelength for different capping layer deposition times. Increasing deposition time leads to a higher emission wavelength and line width until the growth quality deteriorates.

the other samples by assuming a linear relation with the growth time. The obtained capping layer thicknesses are 8.5±0.8 nm and 17.1±1.6 nm for the samples with a capping layer deposition time of 60 s and 120 s respectively. Assuming that the indium content of the QW is unchanged respect to the sample with no Al in the capping layer, it is possible to estimate the aluminum content by comparing the observed PL emission with the simulated energies. As can be seen from figure 7.1, there is a remarkable agreement between the experiments and the simulations assuming an Al concentration of 18%. Even if the obtained thickness of the capping layer is too large to be used in an LED since it may negatively affects the turn-on voltage, the emission peak is in the targeted red region.

Keeping the same QW and capping layer, the barrier growth parameters were optimized keeping as reference the emission spectrum of the red sample. The parameters studied were barrier deposition time and temperature. A thicker barrier increases the leakage current and the activation voltage of the LED [116] and decreases its efficiency at high injection currents [117]. On the other hand, it increases the emission wavelength due to the increased polarization field [118] and enhances the smoothening of the surface. Indeed, after growing the AlGaN layer the surface becomes rough due to the non-optimal growth conditions. The following GaN barrier, grown under a 2D regime, helps to re-obtain a flat surface. Regarding the effect of the barrier growth temperature, a higher temperature should lead to an increase in emission intensity due to a higher crystal quality and lower defect density in the barrier. At the same time, a higher growth temperature increases the risk of In segregation in the quantum wells due to the breaking of In-N bonds. The measured PL spectra for different barrier deposition time are shown in figure 4.11 a), while the PL spectra of the samples grown with different barrier temperatures are shown in figure 4.11 b). Decreasing the barrier thickness results in a much worse emission spectrum compatible with the YL [22]. On the other hand, there is not a substantial difference between 9 min and 11 min

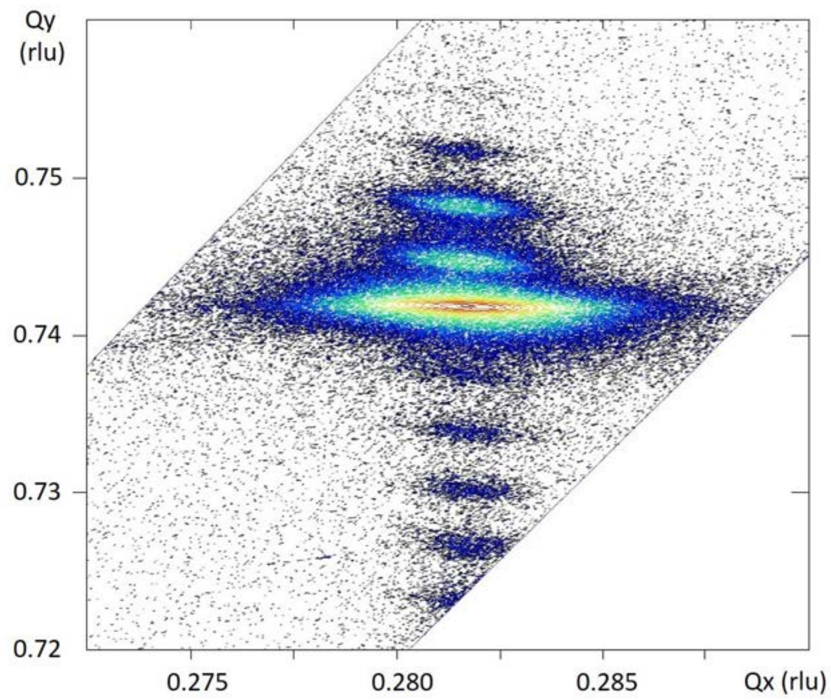

Figure 4.8: Asymmetric (10-15) reciprocal space map of the sample grown with a capping layer deposition time of 90 s.

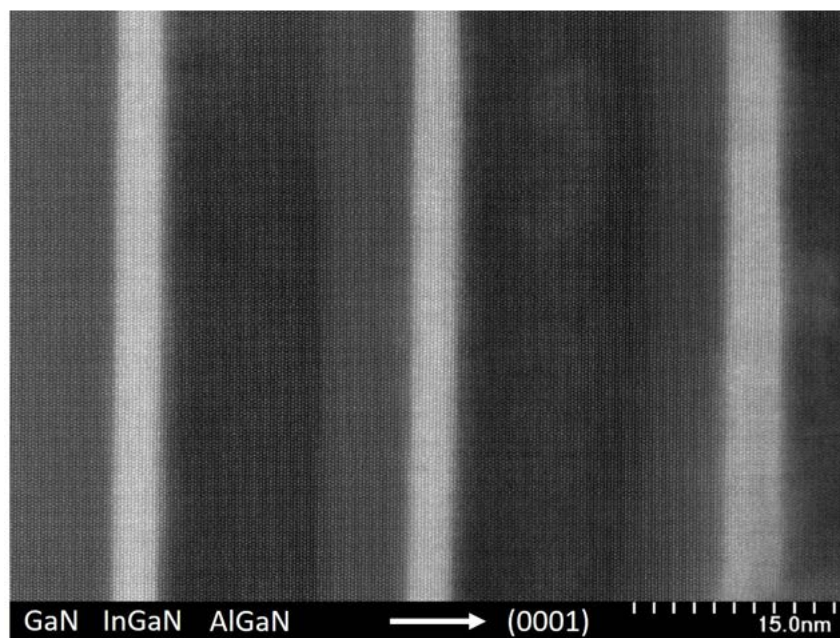

Figure 4.9: TEM image of the sample grown with a capping layer deposition time of 90 s.

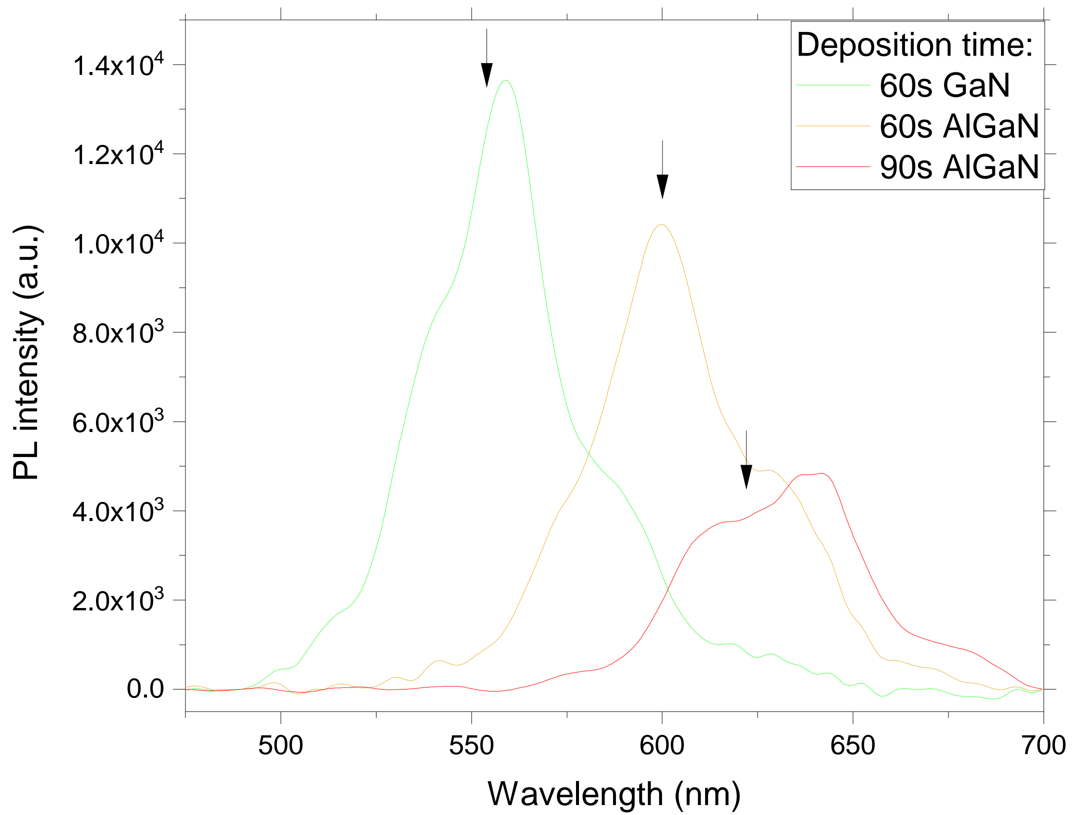

Figure 4.10: Comparison between PL spectra and simulated transition energies (black arrows) for the samples grown with increasing AlGaN capping layer deposition time assuming an Al concentration of 18%.

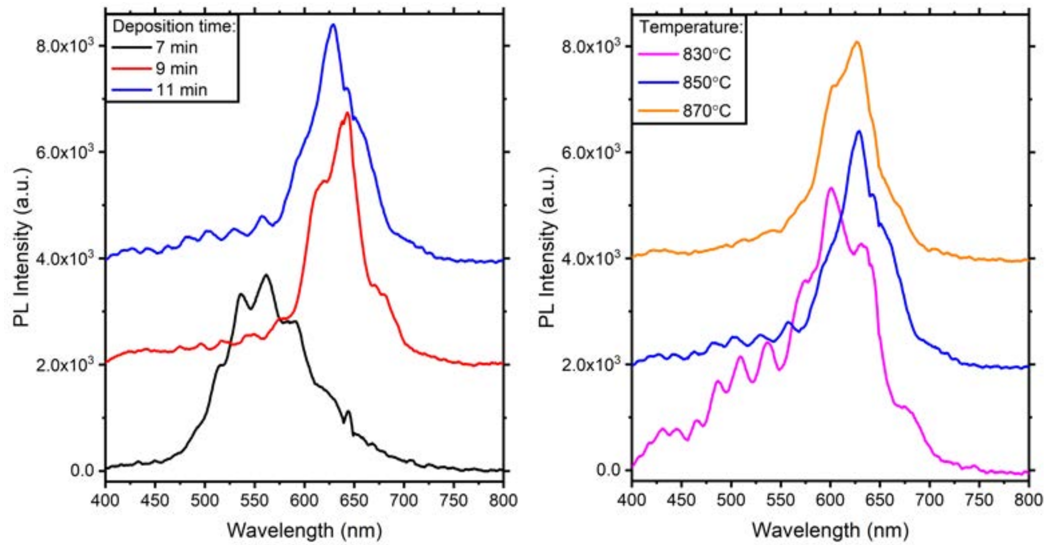

Figure 4.11: PL spectra of a) samples grown with different barrier deposition times and b) barrier growth temperatures.

deposition time. Also lowering the growth temperature leads to a noticeable degradation of the barrier crystal quality, demonstrated by the increase of the 550 nm luminescence band. On the other hand, increasing the barrier growth temperature does not change significantly the emission wavelength and line width. Based on these measurements, both 9 min and 11 min deposition time result in a good emission quality. However, in the spectrum with a deposition time of 11 min it is possible to see a slightly more intense YL. Therefore the chosen growth time for the barrier layer was 9 min. The chosen barrier growth temperature is 850°C, since it was observed that increasing it does not produce noticeable improvements but increases the risk of indium dissociation.

As a conclusion, the best growth parameters found for the structure are reported in table 4.2. Finally, it is important to verify the reproducibility of the samples. For this purpose, another sample was grown using the best growth conditions reported in table 4.2. The comparison between this sample and the one previously grown during the optimization process showed similar results in terms of emission properties, with minor changes which can be addressed to the experimental error in the growth procedure. The consistency of the results proves the effectiveness of the AlGaN capping layer as a reliable method to obtain red emission from GaN based QWs.

Sample series	Structure	Temperature (°C)	Deposition time (min)	TEGa flux (sccm)	TMGa flux (sccm)	TMIn flux (sccm)	TMAl flux (sccm)
Initial parameters	Barrier	850	9	8	-	-	-
	QW	720	2:30	8	-	50	-
	Capping	720	1	-	4	-	5
Capping deposition time	Barrier	850	9	8	-	-	-
	QW	720	2:30	8	-	50	-
	Capping	720	1 / 1:30 / 2	-	4	-	5
Barrier deposition time	Barrier	850	7 / 9 / 11	8	-	-	-
	QW	720	2:30	8	-	50	-
	Capping	720	1:30	-	4	-	5
Barrier temperature	Barrier	830 / 850 / 870	9	8	-	-	-
	QW	720	2:30	8	-	50	-
	Capping	720	1:30	-	4	-	5
Best parameters	Barrier	850	9	8	-	-	-
	QW	720	2:30	8	-	50	-
	Capping	720	1:30	-	4	-	5

Table 4.2: Growth parameters used for the capping layer and barrier optimization. The parameters used for the quantum well were already optimized (see section 4.2.1).

4.2.3 Is it Red?

The perception of a color by the human eye does not depend only on the peak wavelength but also on the emission line width. This is known as Abney effect [119] and it results in a perceived color that may be different from the corresponding peak wavelength. In figure 4.12 a) it is shown the plot of the apparent long-wavelength colors based on [120], in which the combination of peak wavelength and line width appearing as red is delimited by the continuous red curves. In the image are reported the data of this work (labeled as R1 and R2), some of the best literature results [43, 121] and the data of commercially available AlInGaP LEDs [121]. The samples R1 is the one shown in figure 7.1 while sample R2 is the sample growth with the same parameters to verify the reproducibility. As can be seen, the apparent color of both samples selected from this thesis work is perceived as red by human eye. In particular R1 has a similar apparent color to the AlInGaP commercial LED even if it has a much larger line width. Among all the GaN based LEDs reported in the figure, the samples grown in this work have a remarkably narrow FWHM combined with a long emission wavelength, suggesting a good quality of the InGaN QWs.

However, to be more precise the true perceived color depends on the whole emission spectra in the visible range (i.e. 380-780 nm based on the CIE standard observer). The most complete representation of a color is expresses using the CIE chromaticity diagram as discussed in section 3.5. The result for sample R2 is shown in figure 4.12 b). As a reference it is also reported the position of the sRGB and Adobe RGB red which coordinates are (0.64, 0.33). The xy coordinates of the sample emission color are (0.582, 0.349), which does not correspond to a pure color (i.e. it is not spectrally pure). The excitation purity, defined in the CIE diagram as the distance between the sample color and the white point divided by the distance between the boundary monochromatic wavelength and the white point, is the parameter which defines the purity of a color. In case of the sample shown in figure 4.12 b), the corresponding boundary monochromatic wavelength is 605 nm and its purity is 0.80, showing that there is a white background in the emission spectrum which contributes in a significant way to the perceived color. In order to understand the origin of

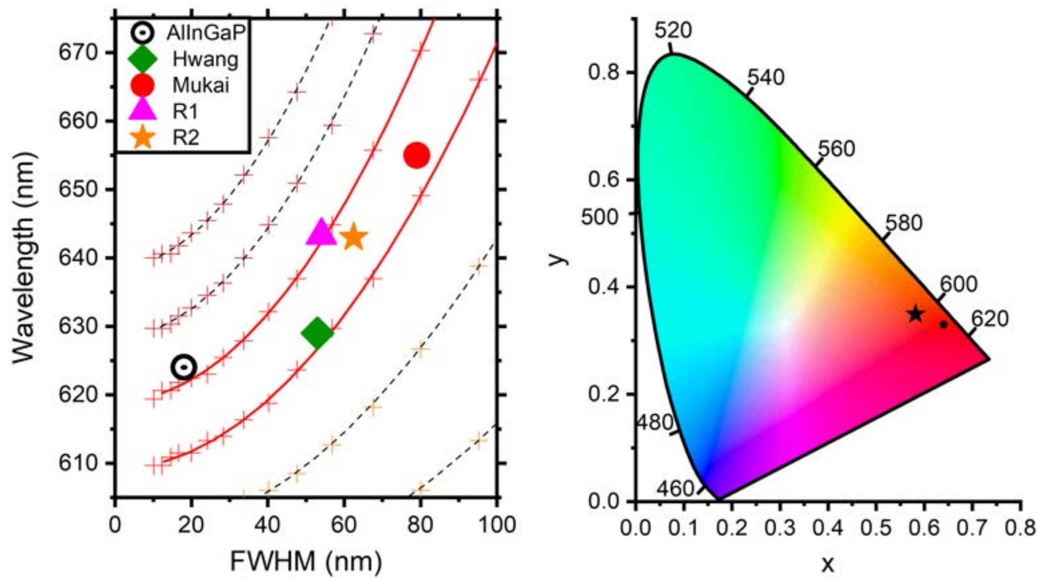

Figure 4.12: a) Representation of the Abney effect to the perceived color depending on peak wavelength and line width. In the image are also reported two samples of this work (R1 and R2) together with some literature data. b) CIE chromaticity diagram in which are reported the coordinates of sample R2 (black star). For comparison it is also reported the coordinate of the sRGB and Adobe RGB red (black dot).

this white background, in figure 4.13 it is shown the PL spectrum of that sample together with its reflectivity spectrum.

The emission peak at 368 nm, which originates from GaN band gap recombination, is not influencing the perceived color since it is in the UV part of the spectrum. However, starting from 400 mn it is possible to notice a background emission which is not present at wavelengths above 700 nm. Since this background is not constant for all the wavelengths, it is probably uncorrelated with the instrumental noise. Another hint for this comes by comparing the intensity oscillations with the reflectivity spectrum. The interference pattern observed in the reflectivity spectrum corresponds to the alternation of constructive and disruptive interference of the light reflected by the GaN/sapphire interface of the sample [97]. As can be seen, the maxima of the interference fringes observed in the reflectivity spectrum below 600 nm coincide with the intensity oscillations of the background emission. Since in PL experiments the only light source able to interfere is the radiation generated by optical recombination inside the sample, this demonstrates that the mentioned background emission must originate from the sample. The wavelength of the background emission, which is lower than the QW transition, it must be originated in the GaN barrier or in the AlGaN capping layer, since both materials can be excited by the HeCd laser. By comparing the emission properties with literature results, it can be identified as the YL band [22], which is believed to originate from a $V_{Ga}C_N$ complex (as discussed in section 1.3). This can be caused by the use of TMGa at low growth temperature during the deposition of the AlGaN capping layer, as discussed in section 2.1.2, or by a poor quality of the GaN barrier. In order to reduce effectively the intensity of the YL band, the best solution would be to use TEGa as precursor. Since the used MOVPE setup was not equipped with two TEGa bubblers, the other possibility is to find another set of growth parameters which allow to grow the QW

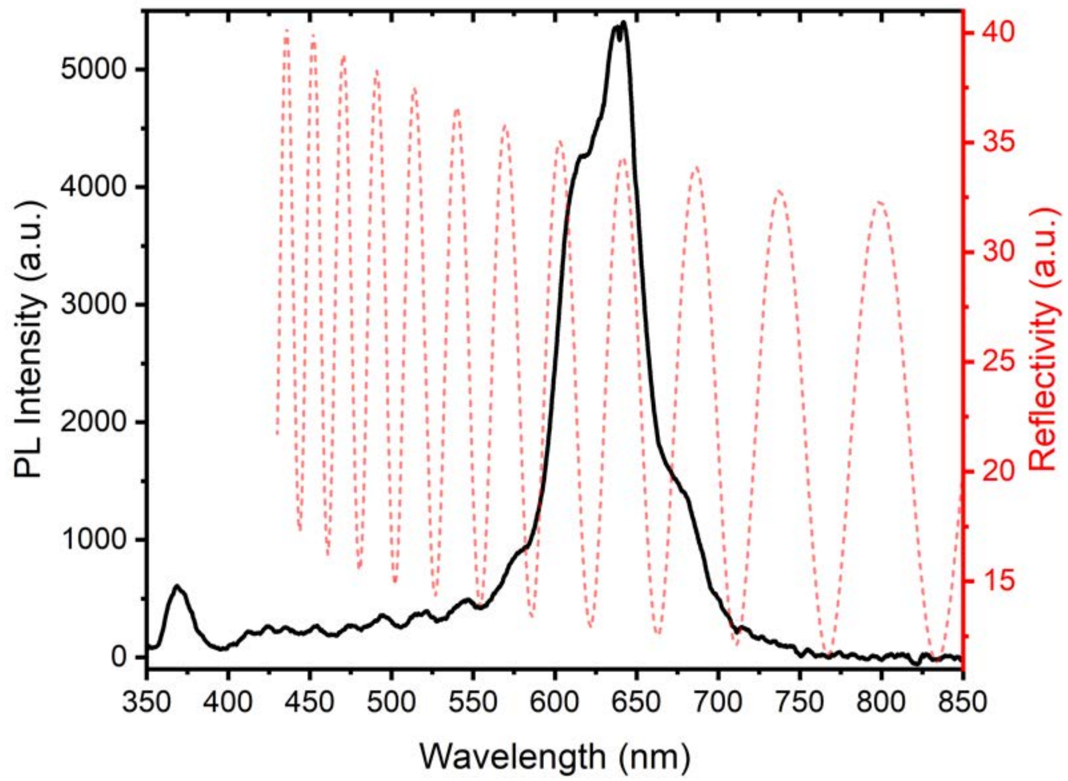

Figure 4.13: Comparison between the PL spectrum and the reflectivity of the red sample.

with a higher TEGa flux and use the same flow to grow the AlGaN capping layer.

5

MBE Growth Optimization

As discussed in section 4.2.3, even if the peak wavelength and line width are the one required for true red color, the broad background luminescence make it appear orange. The observed broad luminescence is most likely originated from radiative recombination through carbon impurities (YL, see section 1.3) in the GaN or AlGaN layers. As widely discussed, carbon incorporation is related especially to the use of TMGa at low growth temperatures. On top of that, also the low emission efficiency achieved at long wavelengths is caused by the high defectivity due to the low growth temperatures. As was discussed in chapter 2.1, MOVPE is extremely good for high temperature growths, but it is not particularly suited for the low temperature ones. On the other hand, MBE does not have the same issue of carbon incorporation since the growth environment is much more clean and the material sources are pure. These properties make MBE a more suitable technique for low temperature growths. Because of that MBE might be an interesting alternative to MOVPE for the realization of long wavelength LEDs. Therefore, the idea of this part of the work would be to reproduce the results of chapter 4 using MBE and compare the emission properties of the QWs to determine if MBE can be competitive in this specific task.

5.1 GaN Buffer Layer Optimization

Since the quality achievable with the high-temperature growth of GaN by MOVPE is higher than MBE, I decided to use as substrates the GaN on sapphire templates grown by MOVPE following the recipe described in section 4.1. In this way I was able to grow homoepitaxially GaN starting from a high quality material, without having to optimize the nucleation layer. However, before growing the QWs it is necessary to grow an initial buffer layer ($\sim$200 nm) to bury all the impurities at the surface far from the active region. It is important for the surface to be as smooth as possible to improve the sharpness of the interfaces with the QWs, ideally resembling the one shown in figure 4.1. It is also important to grow without degrading the crystal quality by introducing new dislocations or other extended defects which would compromise the recombination efficiency of the overlayer. As discussed in section 2.4, the best GaN growth condition with MBE can be achieved in the intermediate regime or under high nitrogen flux and high temperatures. However, since the QWs have to be grown at low temperatures, I decided to target the intermediate regime and use the same parameters as the starting point for the future growth of the QWs.

The growth process was initiated by a 5 minutes thermal cleaning of the template at 750°C under nitrogen plasma flux to avoid GaN dissociation and desorption. The temperature was measured by a thermocouple close to the back side of the sample. After the process, the cleaning of the surface was checked by RHEED, making sure that the diffraction pattern was clear and intense. The substrate temperature was then raised to the desired value and the growth was carried out for 30 minutes. Finished the growth, a RHEED image was taken to check the surface morphology. Finally, the substrate temperature was lowered with the N_2 plasma flowing when above 750°C to reduce the desorption and to stabilize the surface. The samples were then studied by optical microscope and AFM to verify the smoothness of the surface. The reflectivity spectrum was measured and compared to the one taken on the template before growth to calculate the thickness of the grown layer.

Substrate temperature (°C)	Ga BEP (Torr)	N_2 flux (sccm)	N_2 power (W)	RMS roughness (nm)	Growth rate (nm/min)
775	$5.7{\cdot}10^{-7}$	2	200	11.90	13
775	$5.7{\cdot}10^{-7}$	1.5	200	2.962	6.7
775	$5.7{\cdot}10^{-7}$	1	200	0.308	4.8
775	$5.7{\cdot}10^{-7}$	0.7	200	0.707	0.6

Table 5.1: Growth parameters used for the buffer layer optimization and the resulting roughness and growth rate.

The first parameter studied was the nitrogen flux, which corresponds to a change in III/V ratio (i.e. a vertical line in the growth diagram of figure 2.10). The growth parameters used are reported in table 5.1 together with the resulting roughness and growth rate. It is important to notice that changing only the nitrogen flux affects also the growth rate, which in turn has an impact on the surface morphology [122]. The initial parameters were chosen based on previous growths. In figure 5.1 are shown the RHEED images of those samples and in the insets are shown the respective AFM images taken at the end of the growth. As can be seen, there is a clear improvement in surface morphology when decreasing the nitrogen flux from 2 sccm to 1 sccm. However, decreasing it to 0.7 sccm results in droplet formation due to the gallium in excess. This improvement in surface morphology can be observed also by looking at RHEED images, with a clear transition from a spotty pattern to a streaky one. In the case of RHEED images however is not possible to determine exactly the real surface morphology since the diffraction pattern is averaged over the spot size, which is macroscopic. Indeed, the differences in the RHEED patter between the sample grown at 1.5 sccm and 1 sccm are not particularly evident, while the AFM images show a much different morphology. Therefore, to have a reliable characterization the AFM is required. Analyzing these images not only can quantify the roughness of the surface, but it can also give important information on the growth regime.

The sample growth with a nitrogen flux of 2 sccm shows a spotty RHEED pattern typical of a very rough surface, as confirmed by the AFM image. Based on the discussion of section 2.4, this result is most likely due to an excessive nitrogen flux. To improve the surface morphology it is necessary to increase the diffusion of Ga adatoms on the surface. This can be done by increasing the III/V ratio or by increasing the substrate temperature. Therefore, the following sample was grown reducing the N_2 flux to 1.5 sccm. In this case, the RHEED pattern consists of the modulated streaks shown in panel c of figure 3.1. The AFM image shows a larger number of smaller islands compared to the previous sample, which resulted in a lower but still significant roughness. The reduced III/V ratio enhanced the

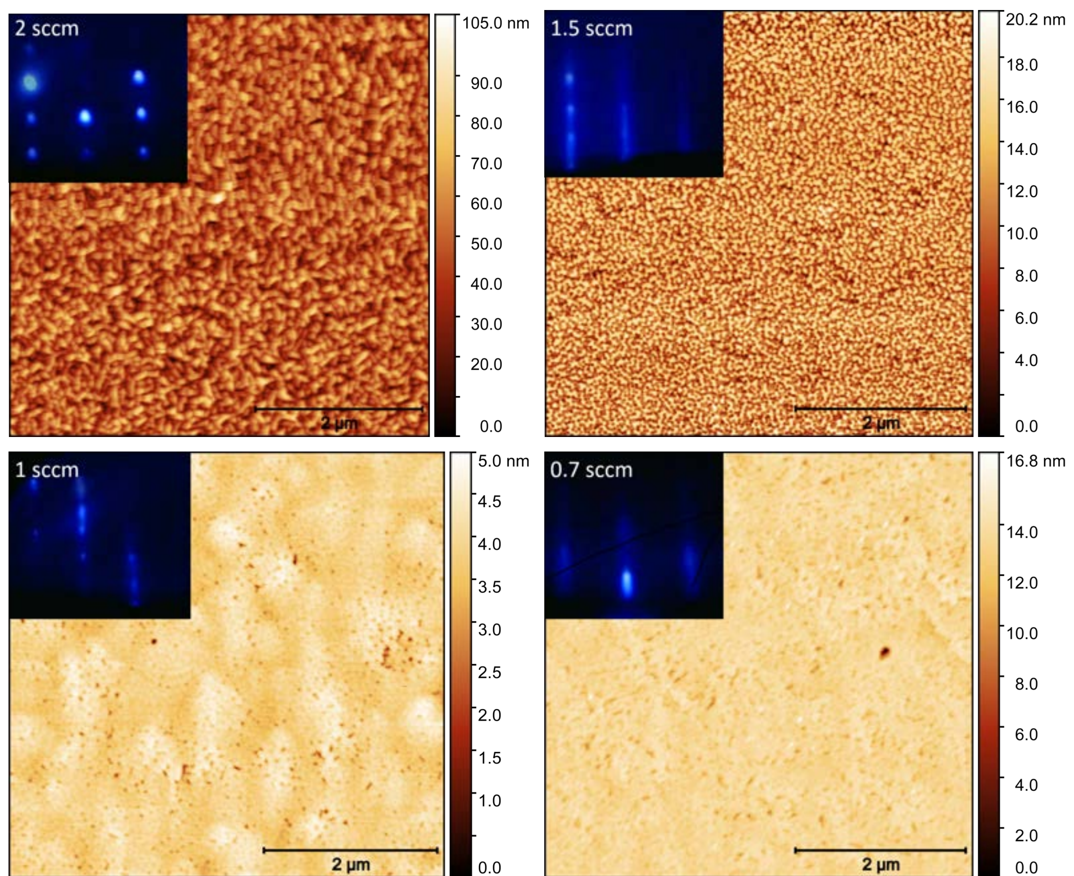

Figure 5.1: AFM images and RHEED patterns of the samples of table 5.1.

lateral diffusion of Ga adatoms which limited the growth ov vertical structures. However, the morphology shows that the mobility of the adatoms on the surface is not yet sufficient to obtain a smooth layer. Growing with a nitrogen flux of 1 sccm resulted in a very smooth surface with a rms roughness of 308 pm, calculated on an area of 25 μm^2. In this case there is no evidence of steps on the surface, suggesting that the growth was performed under the layer-by-layer growth mode. From the image it is possible to notice many holes in the surface. These can be the V-pit found at the termination of dislocations or can be caused by a non perfect merging of the 2D islands. Finally, the nitrogen flow was reduced to 0.7 sccm to verify if it was possible to improve further the surface smoothness. The RHEED image showed a streaky pattern similar to the one obtained for the previous sample, but less intense. This is a hint that the sample was covered by liquid droplets, as was later confirmed by optical microscope images. An AFM image was taken in between the droplets and showed a smooth surface. This finding supports the discussion of section 2.4 that the best growth conditions are found with a Ga bilayer on the surface. Indeed, to form the droplets all the surface has to covered by the metallic Ga bilayer. If more gallium is supplied to the surface, it aggregates and forms liquid droplets since this configuration permits to reduce the surface energy. However, when the droplets are formed the rest of the surface is still covered by the metal bilayer which enhances the Ga diffusion, resulting in a smooth growth as discussed in section 2.4. Despite having a smooth surface, the presence of droplets make the sample unusable for the desired application. Even if it would be possible to chemically remove the gallium droplets, the quality of the GaN grown under the droplets is expected to be lower than the rest of the sample due to the different growth conditions. As a result, the best growth conditions were found using a nitrogen flow of 1 sccm and a power of 200 W.

The next parameter changed was the substrate temperature (corresponding to an horizontal line in the growth diagram of figure 2.10). The Ga flux was kept at $5.7 \cdot 10^{-7}$ Torr and the plasma cell parameters were 200 W and 1 sccm, while the substrate temperature was increased from 775°C to 790°C. The AFM image of this sample is shown in figure 5.2. The measured roughness is 0.740 nm, which is slightly worse compared to the best sample obtained. In particular it is possible to notice a degradation of the surface with an evident mesh-like structure, which is typically observed in nitrogen rich growths. Indeed, if at 775°C the III/V ratio was optimal increasing the growth temperature resulted in an increased Ga desorption (as demonstrated by the lower growth rate measured) which led to an excess of nitrogen on the surface. Reducing the growth temperature below 775°C would most probably result in a lower surface and structural quality and in a gallium-rich environment with the risk of droplet formation.

Therefore it is possible to conclude that the best growth condition were obtained with a substrate temperature of 775°C, Ga flux of $5.7 \cdot 10^{-7}$ Torr, nitrogen flux of 1 sccm and a plasma power of 200 W. The obtained growth rate permits to obtain a buffer layer thick enough (144 nm) in a relatively short time (30 min) which is a good result. Therefore I didn't investigate the effect of a different growth rate on the surface morphology since the obtained result was satisfactory. Indeed, even if better results could be achieved by changing the growth rates, this would have required another optimization of the growth parameters. As an example, reducing the growth rate could lead to a step-flow growth mode [122] but at the same time the desorption rate of Ga adatoms is expected to increase due to the longer time elapsed before binding to a nitrogen atom. As a consequence, keeping the same temperature and III/V ratio would probably lead to a nitrogen-rich growth with a

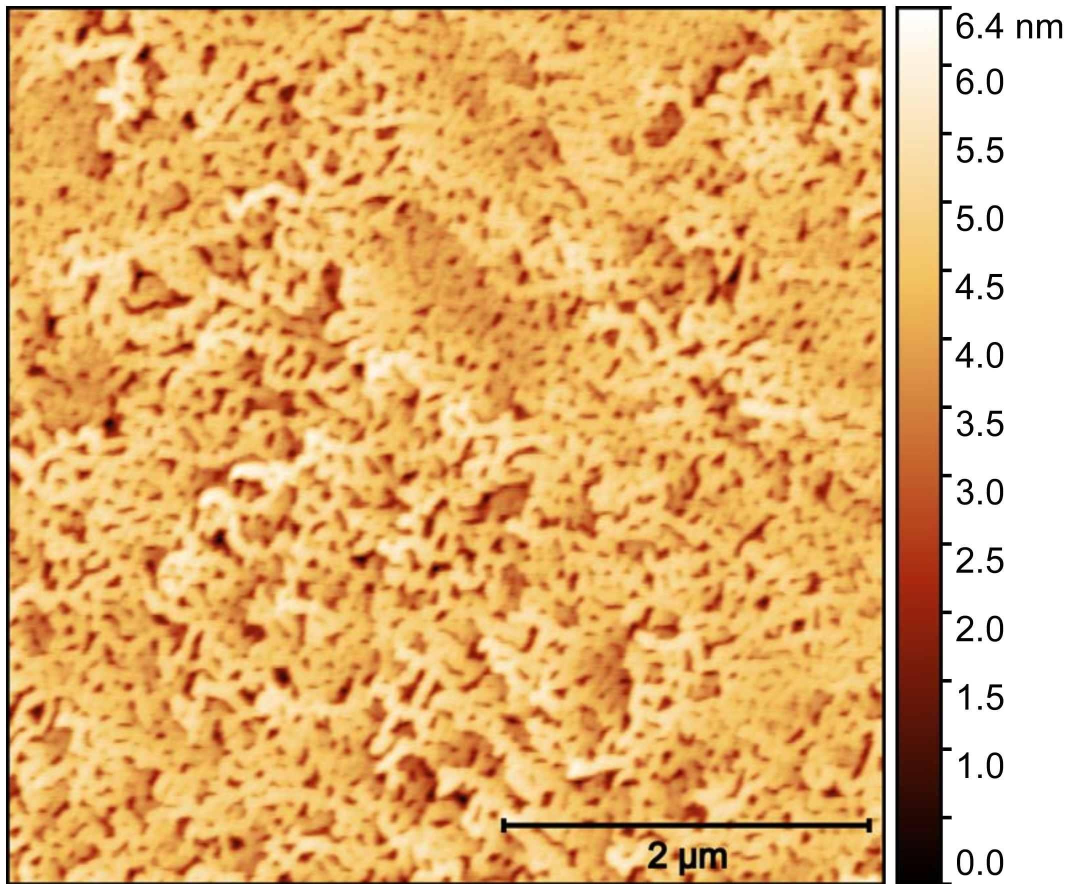

Figure 5.2: AFM image of the sample growth at 790°C.

roughening of the surface.

As a conclusion, a good buffer layer morphology was obtained after the optimization process in which the III/V ratio and the substrate temperature were changed. The future step of this work will be the realization of GaN/InGaN/GaN QWs on top of the buffer layer, using the obtained parameters as a starting point for the optimization. The target of this future work will be to obtain a green QW with an emission peak wavelength similar to the best result of section 4.2.1 to compare the line width and emission intensity. Depending on the result, I will proceed with the growth and optimization of the AlGaN capping layer to verify if GaN/InGaN/AlGaN QWs grown by MBE can improve the results obtained by MOVPE.

6

Simulations

Simulations are a powerful tool to study the effect of AlGaN capping layer on the emission properties from a numerical point of view. Although simulations do not take into account many experimental properties of the system, they allow to have an insight of the physics involved. This permits to give an explanation of the observed phenomena and to understand the fundamental properties which determine the observed results. As mentioned in section 3.7 and verified in chapter 4, the simulation parameters used are in good agreement with the experimental data. This gives more relevance to the results that will be discussed in the following part. This chapter will be entirely based on the theoretical simulation of GaN/InGaN/GaN and GaN/InGaN/AlGaN QWs. Based on the analysis of these results I will discuss the effect of the AlGaN capping layer on the emission properties of the GaN/InGaN/GaN QWs and propose an explanation. Part of these results were published in ref. [123].

It is well known that the quantization energy of a nanostructure is inversely proportional to the width of the confining region. As a consequence, increasing the thickness of the QWs results in a longer emission wavelength. However, this also decreases the wavefunction overlap which results in a reduced oscillator strength. A longer emission wavelength can also be obtained by increasing the indium content of the QW, which in turn reduces the recombination probability due to higher wave function separation caused by the increased piezoelectric field. In figure 6.1 are shown the simulated emission wavelength a) and optical matrix elements b) of a GaN/InGaN/GaN QW as a function of thickness and indium content. As expected, a longer emission wavelength can be obtained both by increasing the indium composition or the QW thickness.

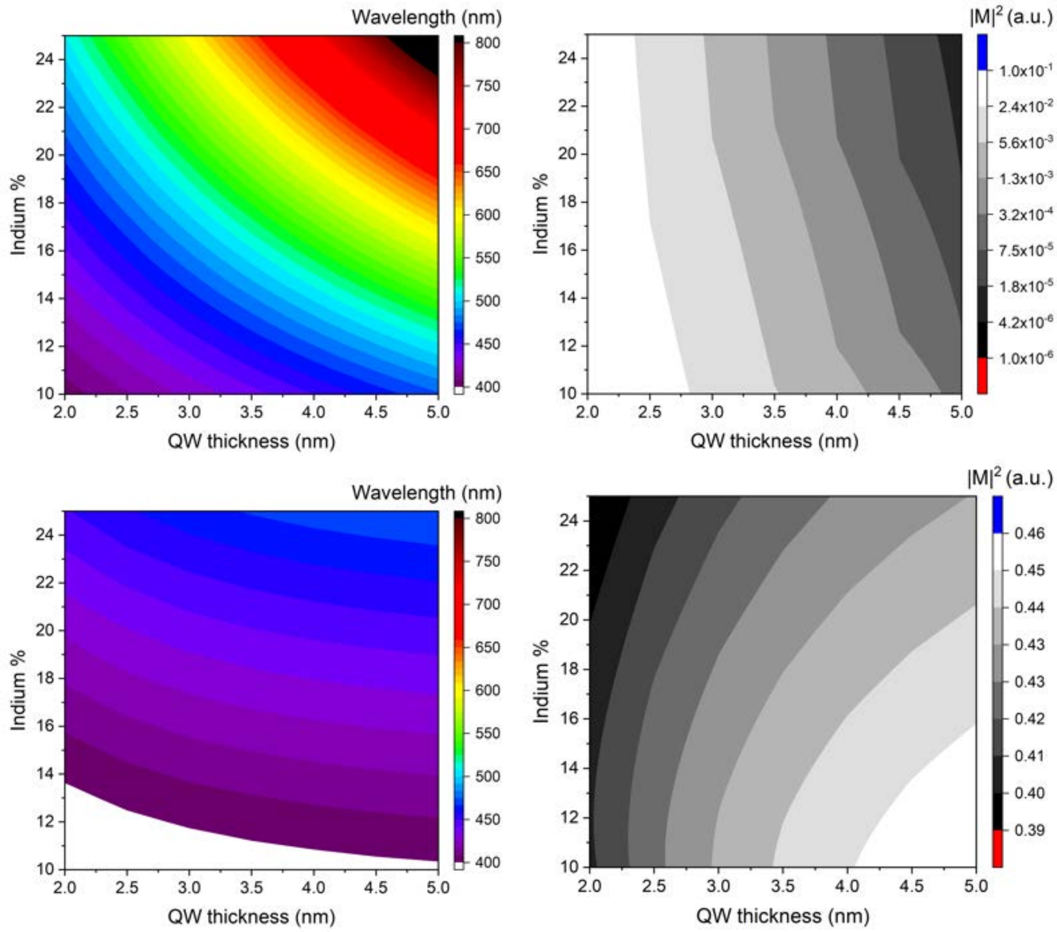

Figure 6.1: a) Simulated emission wavelength and b) optical matrix elements of an GaN/InGaN/GaN QW as a function of well thickness and indium composition. Panels c) and d) show the calculated emission wavelength and optical matrix elements for non-polar orientation.

In figure 6.1 c) and d) are shown the calculated emission wavelength and optical matrix elements for the same structure with a non-polar orientation. It is evident that the effect of the electric field has a sever impact on both emission wavelength and optical matrix elements. In case of the emission wavelength, the electric field is responsible of the QCSE, as discussed in section 1.6. This phenomenon leads to a redshift of the emission wavelength proportional to the intensity of electric field in the QW. On the other hand, it reduces the spatial overlap of the electron and hole wavefunctions due to the opposite response to the field, resulting in a reduced $|M|^2$ of several orders of magnitude compared to the case without field. These simulations show the importance of using a non-polar orientation to be able to obtain long emission wavelengths with a limited indium content. This is particularly important since having a large indium concentration requires low growth temperatures which enhance the defects incorporation, as discussed in section 2.1.3. These results indicates that the electric field does have positive effects on the recombination properties.

However, when discussing about the use of the AlGaN capping layer to obtain long emission wavelength, the high electric field is typically addressed in literature as a negative effect which has to be mitigated. While it is true that a high electric field reduces the

spatial overlap of the wave functions due to the increased QCSE, it gives many advantages which are often neglected. Therefore, in this section I will analyze in depth the effect of the AlGaN capping layer on the emission properties of GaN/InGaN/AlGaN QWs. For this purpose, I studied the effect of capping layer thickness and composition on the emission wavelength and optical matrix elements for different In concentrations of the InGaN QW. A higher electric field in the QW can be achieved both by increasing the Al content in the capping layer or by making it thicker. In the first case, the electric field in the QW increases due to the larger polarization constants of AlN compared to GaN. Therefore, a larger aluminum content results in a larger polarization field. In the second case, a thicker capping layer increases the potential drop in the AlGaN layer. If the total thickness of the GaN/InGaN/AlGaN structure increases, the absolute value of the electric field in the QW has to increase as a result of the PBC. This can be understood by approximating the structure as a parallel plate capacitor. The potential drop across the structure has to be zero due to the PBC. Since $\Delta V = \Delta(E \cdot d)$, the change in the total thickness of the structure d has to be compensated by a change in the electric field. In particular, it can be shown that the electric field in the barrier and capping layer decrease while the electric field in the QW increases.

In the next section I will study the effect of the increase in AlGaN composition while keeping the thickness of the capping layer constant.

6.1 AlGaN composition change

When the Al percentage in the capping layer is increased, the polarization charges at the interfaces increase due to the larger polarization constants of AlN compared to GaN and the larger strain. This leads to an increase in QCSE which, as discussed in section 1.6, is expected to increase the emission wavelength and reduce the wave function overlap. To study the effect, I have calculated the optical properties of GaN/InGaN/GaN and GaN/InGaN/AlGaN QWs. The simulated structure consists of 10 nm GaN barrier below a 3.5 nm InGaN quantum well and a 5 nm (Al)GaN capping layer. On top of the capping layer there was another GaN barrier 5 nm thick. Periodic boundary conditions (PBC) were imposed to the structure in order to mimic the behavior of MQWs in a biased n-p junction. Indium composition of the QWs was varied between 18% and 29%. (Al)GaN thickness was kept fixed at 5 nm, while the Al content was increased in steps of 2% from 0% until the highest hole state moves outside of the QW due to the increased polarization field and low confining potential.

Figure 6.3 shows the optical matrix element ($|M|^2$) of the ground state transition as a function of emission wavelength for GaN/InGaN/GaN and GaN/InGaN/AlGaN QWs. For comparison, the same theoretical analysis was performed on a multi QW system inserted in a n-p junction with an applied forward bias of 2V to verify that the two behaves similarly. The simulated band structure is reported in figure 6.2 in which are also shown the calculated ground state wavefunctions of electrons and holes. The emission wavelengths and optical matrix elements, calculated for the central QW, are shown in figure 6.3 b) ("biased LED") and are compared to the results obtained from the undoped structure with PBC ("undoped") for the $In_{0.22}Ga_{0.78}N$/AlGaN/GAN case, where in both cases each data point corresponds to a 2% increase in Al content. It is important to mention that the "biased LED" and "undoped" structures have a similar behavior for all the indium contents of figure 6.3 a). Here it is shown only the 22% indium case as an example. As can be seen, in the "biased LED"

simulated curve there are some missing points, which is caused by the fact that in some cases the simulations failed to converge due to numerical errors. Nevertheless, all the points for which the simulation converged show a remarkable agreement with the optical properties of the simulated QW with PBC. The reason for this agreement is because in the yellow-red region the polarization fields due to strain are much larger than the one imposed by the band bending from the biased junction. However, from the imgae it is possible to notice that there is no strict correspondence between Al content and emission wavelength for the two structures. This happens because not only the QCSE contributes to the emission wavelength, but also the electric field in the barriers. Therefore a small difference in the fields results in slightly different emission wavelengths with the same Al content and this effect is expected to be enhanced with increasing field.

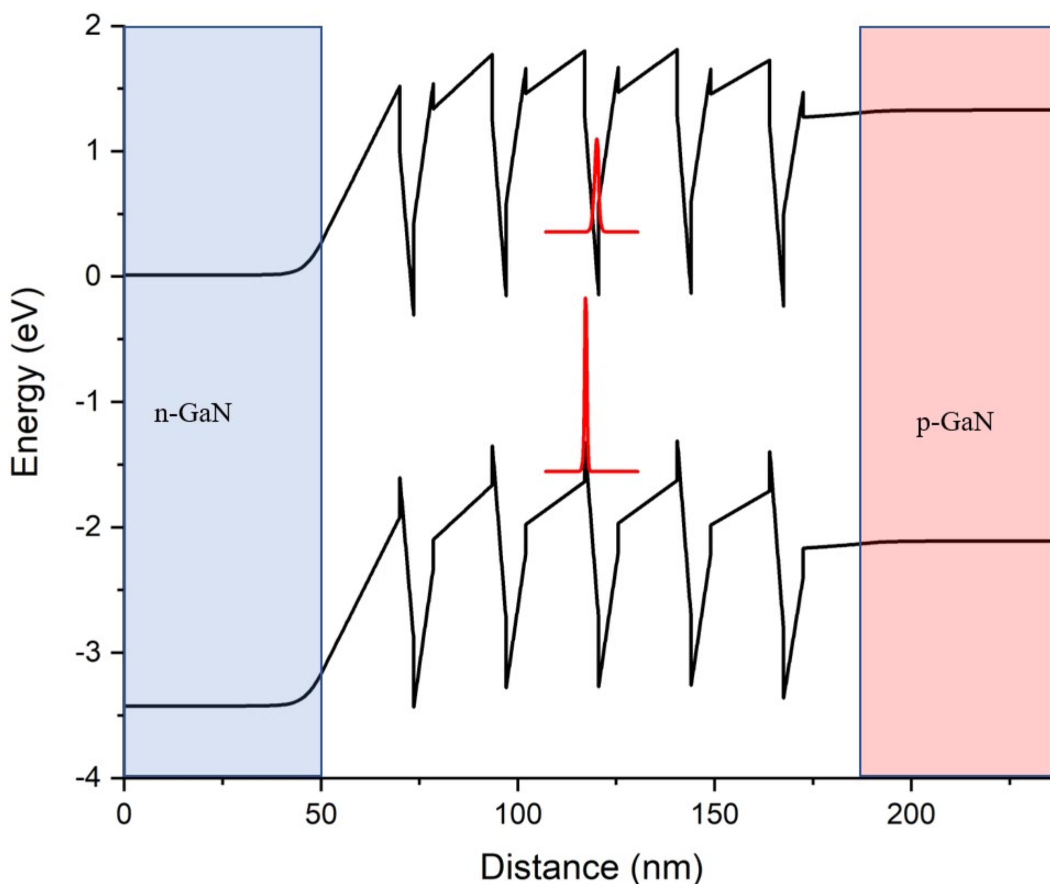

Figure 6.2: Calculated band structure of a biased LED with five stacks of GaN/InGaN/AlGaN QWs. The quantum properties were calculated for the central well. The resulting electron and hole wavefunctions are shown in red.

As already discussed, the main reason for the emission redshift is the increase in QCSE. By definition, a larger electric field is expected to decrease the wave function overlap due to increased carrier separation. However, from the simulations of figure 6.3 it is possible to see that initially the optical matrix elements increase, despite the larger electric field. The maximum increase in $|M|^2$ is found for the lowest indium concentration, which also shows the fastest reduction of intensity when further increasing Al content. Moreover, the

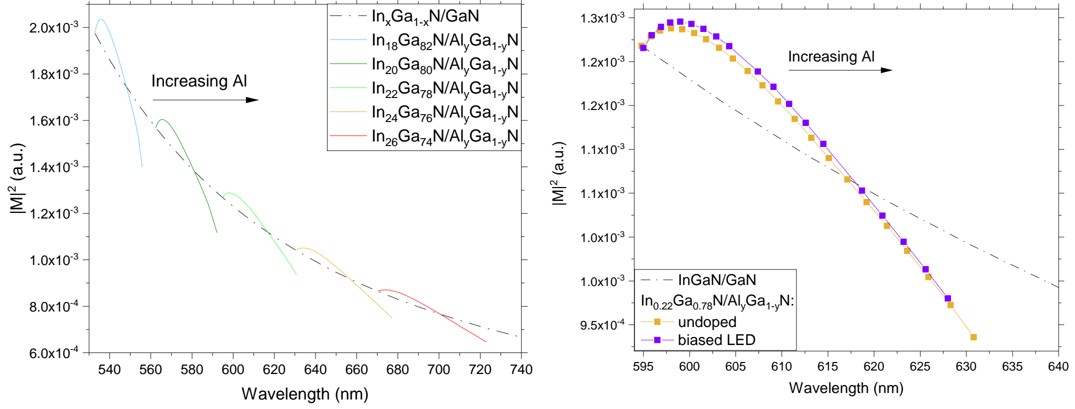

Figure 6.3: a) Calculated optical transition matrix element of the ground state ($|M|^2$) for various GaN/InGaN/(Al)GaN QWs with indium content ranging from 18% to 29% (on the black line). The emission wavelength increases when adding an AlGaN capping layer. b) Magnification of the simulated GaN/$In_{0.22}Ga_{0.78}N$/AlGaN QW where each data point corresponds to a 2% increase in Al content. The result is compared with the simulation of the same structure in a biased n-p junction, from where it is possible to see that there is no substantial difference between the results. From [123]

peak of $|M|^2$ is found at higher redshifts for higher indium contents. The optical matrix elements of the GaN/InGaN/AlGaN QWs for low Al contents are always larger than the GaN/InGaN/GaN QWs until when they cross and the $|M|^2$ of the latter becomes larger.

To understand the origin of this behavior a useful parameter is to calculate the portion of carrier wave function located in the quantum well. Although the correct physical behavior of the system is represented by the optical matrix elements (figure 6.3), the probability of finding carriers in the QW can be used as a visual explanation of how the AlGaN capping layer affects the carrier location. Interestingly, I found that the probability of finding electron (figure 6.4 a) and hole (figure 6.4 b) in the QW region is affected by the change in aluminum content in a profoundly different way. For GaN/InGaN/GaN QWs (i.e. no aluminum in capping layer), the carrier position is only related to InGaN composition, which determines potential barriers and polarization field. As expected, for higher indium contents the wave functions are more strongly localized near the interfaces due to higher field and larger band offset. Despite the higher probability to find electrons and holes in the QW region, the overlap decreases as a consequence of the increased QCSE. In fact, the higher field tends to separate electrons and holes, confining them at the opposite interfaces (holes at the GaN/InGaN one and electrons at the InGaN/(Al)GaN one), which can be seen from the band structure of figure 6.5.

When an AlGaN capping layer is added to the structure, the behavior of electrons and holes deviates significantly. In case of electrons (figure 6.4 a), the larger potential barrier combined with the higher field increase the fraction of the electron wave function inside the QW from around 72% to even 90%, regardless of initial indium concentration. On the other hand, holes (figure 6.4 b) are confined at the GaN/InGaN interface. Therefore, they are only sensitive to the InGaN content and the change of the field in the GaN barrier. With increasing AlGaN content, the field across GaN barrier decreases, causing hole wave function to leak out from QW. For the low-indium case, the probability of finding a hole

inside the InGaN region decreases more than linearly with the increasing field due to lower band offsets, while for high indium content the leakage is reduced by the higher confining potential.

The combination of the different responses to the increased aluminum content in the capping layer determines the unexpected behavior of the optical matrix elements of figure 6.3.

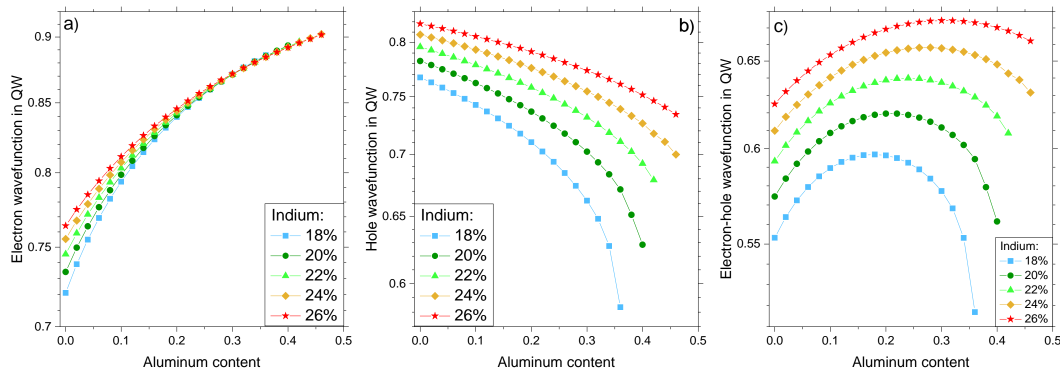

Figure 6.4: Probability of finding an electron (a), hole (b) and both electron and hole (c) in the QW as a function of the increase in aluminum content for GaN/InGaN/AlGaN QW. In case of electrons, the increasing field enhances the confinement inside the InGaN QW. Hole confinement instead is strongly affected by initial indium composition and decreases with increasing Al content. The resulting combined probability shown in panel (c) resembles the behavior of the optical matrix elements, with an increase in confinement followed by a decrease. From [123]

To visualize how wave functions are affected by the AlGaN capping layer, figure 6.5 shows the band structures and electron and hole ground state wave function probability densities of $In_{0.24}Ga_{0.76}N$/GaN and $In_{0.24}Ga_{0.76}N/Al_{0.40}Ga_{0.60}N$/GaN QW. As was shown in figure 6.4 a, the electron wave function is pushed further into the QW with increasing aluminum content in the AlGaN layer due to larger polarization field in the capping layer and the higher band offset at the InGaN/AlGaN interface . Both these effects contribute to increase the confinement of the electron wave function in the QW. This explains the higher portion of the electron wave function in the InGaN QW of figure 6.4. At the same time holes, which are located at the GaN/InGaN interface, start to leak in the GaN barrier due to lower field in the GaN barrier until the highest hole state is almost entirely outside from the QW.

Based on this analysis, there is a fundamental aspect of the AlGaN layer effectiveness that was never really considered in literature, which is the change of the InGaN/(Al)GaN interface. This phenomenon permits to increase the carrier overlap despite the larger electric field in the QW and is one of the reasons for which GaNInGaN/AlGaN QWs have a higher recombination intensity compared to GaN/InGaN/GaN.

To further investigate this aspect, it is also interesting to study how the AlGaN thickness influences the emission properties.

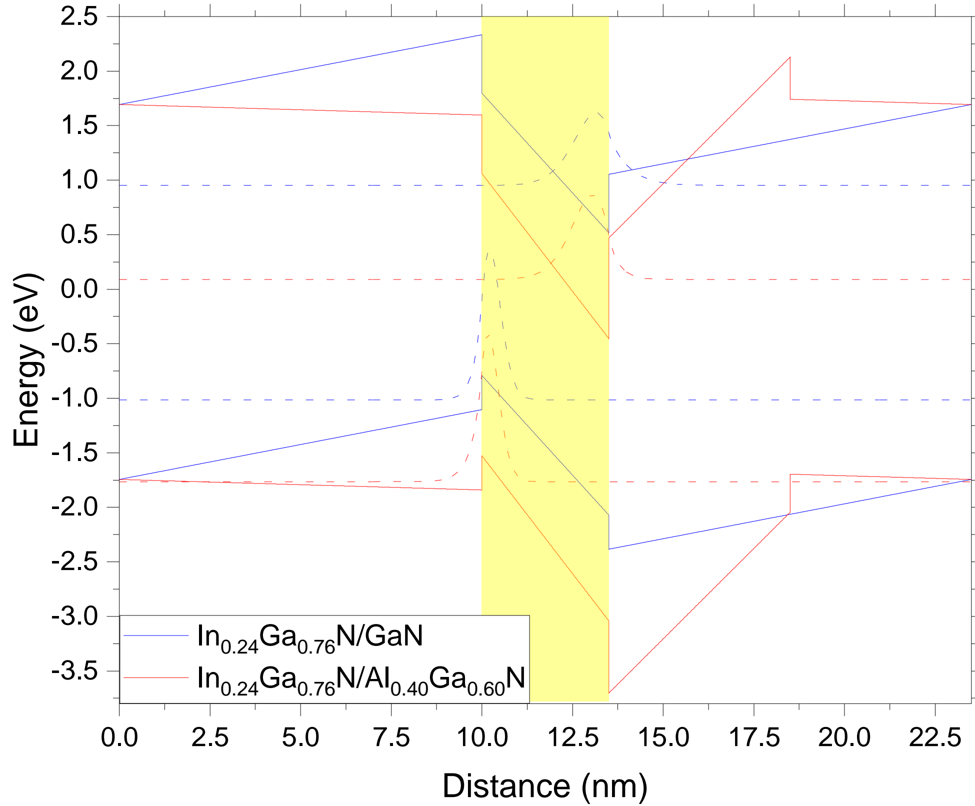

Figure 6.5: Calculated band structure (solid lines) of $In_{0.24}Ga_{0.76}N/GaN$ (red) and $In_{0.24}Ga_{0.76}N/Al_{0.40}Ga_{0.60}N/GaN$ (blue) QW with the electron/hole ground state wave function probability density shown as dashed lines. The QW region is highlighted for easier comparisons. From [123]

6.2 AlGaN thickness change

To study how the AlGaN thickness affects the emission properties, the simulated structure was similar to the one used in section 6.1. It consisted of a 10 nm GaN barrier below a 3.5 nm InGaN QW capped with an AlGaN layer of thicknesses ranging from 1 to 9 nm and an Al content from 0% until the hole wavefunction starts to leak out in the barrier. Finally a GaN barrier layer was put on top of the capping layer. The total thickness of the capping layer plus the top barrier was kept fixed at 10 nm.

In figure 6.6 it is shown the result for an $In_{0.22}Ga_{0.78}N$ QW. Each data point corresponds to an increase of 5% in Al content. The result for a 5 nm capping layer (dark blue line) is the same of figure 6.3 b. As can be seen, the capping layer thickness has a profound effect on the emission properties of the QW. An increase in the capping thickness leads always to the redshift of the emission wavelength except for the 1 nm case. Moreover, to obtain the same emission wavelength is required lower Al content if the capping layer is thicker. As an example, it is possible to obtain 620 nm emission with a 3 nm thick $Al_{0.60}Ga_{0.40}N$ or a 9 nm $Al_{0.15}Ga_{0.85}N$ capping layer. This happens because the absolute value of the electric field intensity in the QW is larger for thicker capping layer with the same aluminum content due to larger polarization field, as can be seen from figure 6.7.

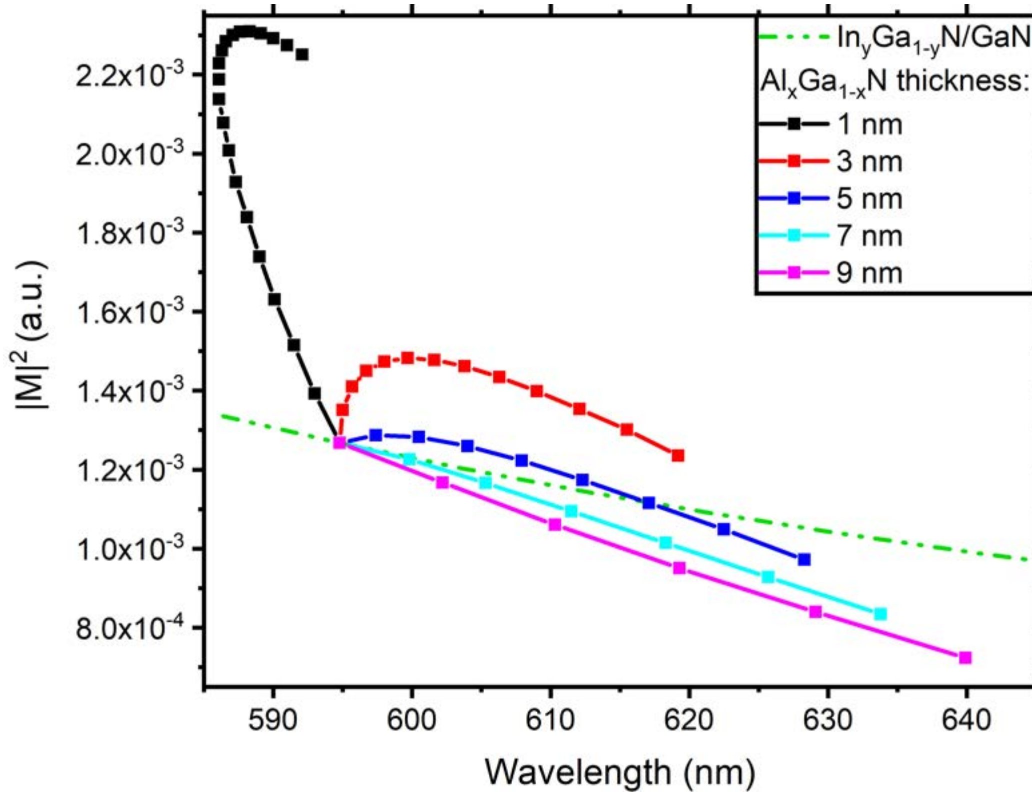

Figure 6.6: Optical matrix elements of an $In_{0.22}Ga_{0.78}N$/AlGaN/GaN QW for different AlGaN thicknesses. Each data point corresponds to a 5% increase in Al content in the capping layer. For comparison is also shown the $|M|^2$ of $In_yGa_{1-y}N$/GaN QW with varying In composition (green line).

Based on QCSE theory (section 1.6), one would expect that the same emission wavelength is obtained for the same electric field in the QW. If we take as example an electric field of -3.8 MV/cm, referring to the data shown in figure 6.7 this can be obtained with an aluminum content ranging between ∼20% to ∼95% depending on the capping layer thickness. However, the emission wavelengths of those structures (figure 6.6) are different from each other. From table 6.1 it is possible to notice that the thicker is the capping layer, the longer is the emission wavelength, despite having approximately the same electric field in the QW. The difference in emission wavelength with increasing capping thickness is larger for thinner layers and it becomes negligible for thicker ones.

AlGaN thickness	Aluminum content	Emission wavelength (nm)	QW E field (MV/cm)	Capping E field (MV/cm)	Electron WF in QW	Hole WF in QW
1 nm	95.1%	591	-3.80	10.35	0.96	0.745
3 nm	39.7%	606	-3.80	3.55	0.90	0.745
5 nm	25.3%	612	-3.80	2.19	0.86	0.745
7 nm	18.6%	616	-3.80	1.55	0.83	0.745
9 nm	14.7%	619	-3.80	1.29	0.81	0.745

Table 6.1: Properties of the simulated GaN/InGaN/AlGaN QW with different capping layer thickness and Al content but approximately the same QW electric field.

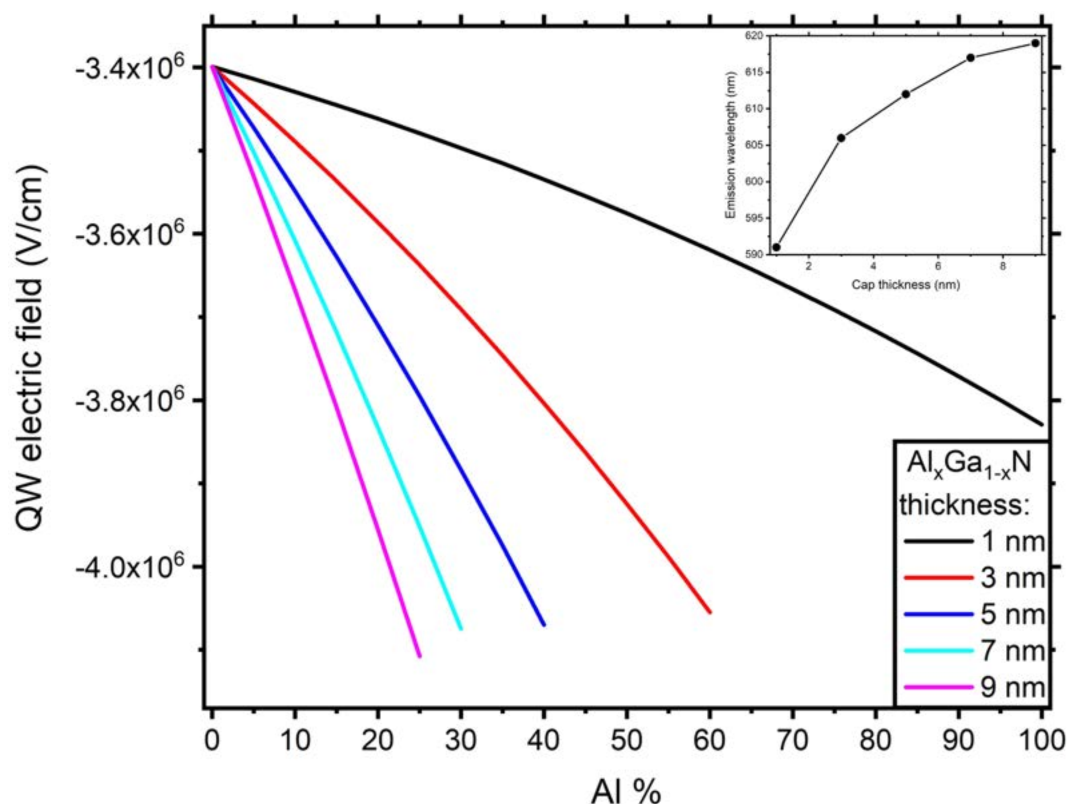

Figure 6.7: Quantum well electric field of an $In_{0.22}Ga_{0.78}N$/AlGaN/GaN QW for different AlGaN thicknesses. The inset shows the emission wavelength as a function of cap thickness. As can be seen, for thicker capping layers the emission wavelength tends to saturate.

It is clear from this analysis that there is another effect which affects the emission wavelength besides QCSE. It can be seen that despite having a similar electric field in the QW and in the barrier, the one in the capping layer is extremely different. As a consequence, the GaN/InGaN interface is expected to remain unchanged for all the structures of table 6.1, while we can expect significant differences at the InGaN/AlGaN interface. Indeed, this effect has an influence only on the electron wavefunction since holes are affected by the changes in the GaN/InGaN interface. This is verified by the data reported in table 6.1.

In order to understand the origin of this phenomenon, in figure 6.8 is shown the electric potential of those structures. As can be seen, the potential in the barrier and the QW is the same for all the AlGaN thicknesses. In the capping layer however the potential drop is different depending on the capping layer thickness. In particular, the thinner is the capping layer, the smaller is the potential drop. More importantly, the derivative of the potential (i.e. minus the electric field) is larger for thinner capping layers. However it should be noted that in all the cases the total potential drop in the capping layer and the top barrier is constant, as imposed by the PBC. The electric potential determines the slope of the energy bands and can be imagined as a pushing force for the carriers. As a consequence, a steeper slope in the capping layer (which corresponds to a larger electric field) increases the localization of the electron wave function in the QW. This effect, combined with the change in potential barrier depending on the AlGaN composition, is responsible for the differences in

electron confinement reported in table 6.1. On the other hand, hole properties are uniquely determined by QCSE since there is no change in the GaN/InGaN interface and indeed all the structures of table 6.1 show exactly the same behavior. This result shows again that the emission properties of the GaN/InGaN/AlGaN QWs is not only determined by QCSE, but is strongly affected by the InGaN/AlGaN interface and also by the capping layer properties.

By looking again at the figure 6.6 it is possible to observe that the results obtained for a capping layer thickness of 3 nm are the most interesting since it guarantees a large recombination efficiency and long emission wavelength. Moreover, the thickness of the capping layer is not excessive and therefore the negative impact on the electrical properties of an LED is expected to be small.

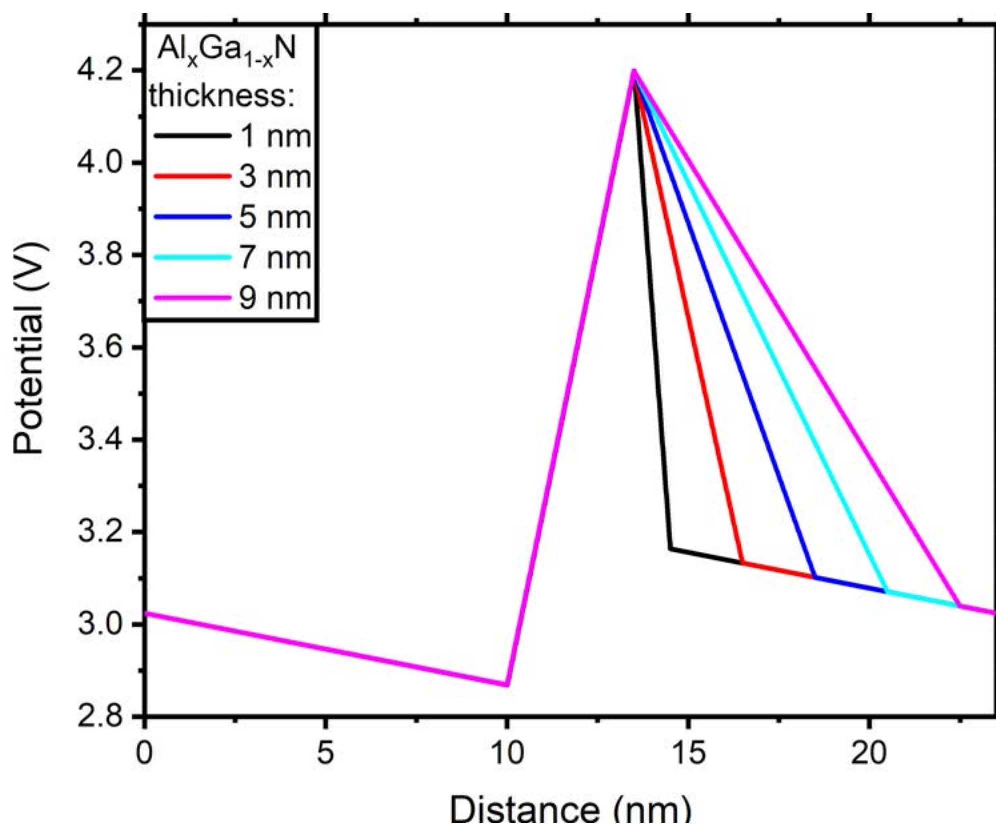

Figure 6.8: Electric potential of the structures reported in table 6.1.

An issue which has emerged from this simulations is the low confining potential for holes. As typically happens for III/V semiconductors, the band offset of an heterojunction is not split equally between conduction band and valence band. In the case of these simulations, the obtained InGaN/GaN valence band offset is 36%. As introduced in section 6.1, when the capping layer is too thick the holes wave function tend to leak in the barrier causing a loss of confinement, resulting in a decrease in the optical matrix elements. Based on the previous discussion, this is only determined by the electric field in the QW and in the GaN barrier. On the other hand, the results discussed in this chapter have demonstrated that the increased efficiency of GaN/InGaN/AlGaN QWs is determined by the changes in the InGaN/AlGaN interface. Most importantly, the simulations have shown that there is an increase in the oscillator strength when using the AlGaN capping layer despite the larger

QCSE. As discussed, this counter-intuitive result is determined by the combination of a larger electric field and a larger potential barrier at the InGaN/(Al)GaN interface. In the past the electric field in polar structure was always considered as a negative effect which had to be mitigated. As a result, the possibility to engineer the potential barrier and the electric field to improve the recombination efficiency were only investigated to reduce the electric field in the structure. This work has shown instead that increasing the QCSE with a proper optimization of the potential barrier can give interesting results. In particular the structure of figure 6.6 with a capping layer of 3 nm seems to be the most interesting one in terms of achievable emission wavelength and oscillator strength. Another possible solution to increase the polarization field and confining potential can be the use of AlInN as a barrier layer, similarly to what was recently done by Sun et al. [124]. This would lead to a larger confining potential for holes and a larger polarization field in the QW. The possibility to have AlInN lattice-matched with GaN can bring these advantages without increasing the elastic energy in the structure.

7 Results and Discussion

In chapter 4 I reported the effect of various growth parameters on the emission and structural properties of InGaN/GaN and InGaN/AlGaN/GaN QWs, managing to obtain red emission. Even if the samples requires further optimizations, the results show that this approach is very promising to obtain red emission using III-N semiconductors. In chapter 6 I studied the effect of the AlGaN capping layer from a theoretical point of view, showing an unexpected increase in wavefunction overlap and identifying its origin. The purpose of this chapter is to study more into details some experimental results introduced in chapter 4 by comparing them with theoretical simulations. I will use this comparison to discuss more into detail the observed effect of the AlGaN capping layer.

7.1 Intensity analysis

The best way to understand the effect of the capping layer on the emission properties of the QWs is to directly compare the luminescence of InGaN/GaN and InGaN/AlGaN/GaN samples with the QWs grown under the same conditions. Those samples were presented in figure 7.1 of section 4.2.2 and are reported here for a better reading.

In that sample series the InGaN QWs and the GaN barrier were grown under the same conditions. Even if there is no experimental proof that the QW are identical, it is reasonable to assume that the differences are negligible. The simulated transition energies for those samples are indicated in the figure by the black arrows. As can be seen, the agreement with the spectra at lower emission wavelength is extremely good. On the other hand, the simulated peak of the last sample doesn't seem to correspond to the maximum of the emission spectrum but it coincides nicely with its center of gravity. The luminescence spectrum of this sample is quite broad and it is possible to observe two local maxima. There are many possible explanations for this observation, such as emission from defects (red luminescence reported in [22]) and alloy or electric field fluctuations. However, by comparing the PL spectrum with the reflectivity (figure 4.13), it is possible to note that the two local maxima of the emission spectrum coincides with two subsequent maxima of the Fabry-Perot interference pattern. Based on this result, it is possible to conclude that both the observed local maxima are enhanced by constructive interference. It can also be speculated that the true emission peak can be found between 600 nm and 650 nm, which is in good agreement with the simulated emission peak at $\sim$625 nm. As can be seen from the image, this wavelength

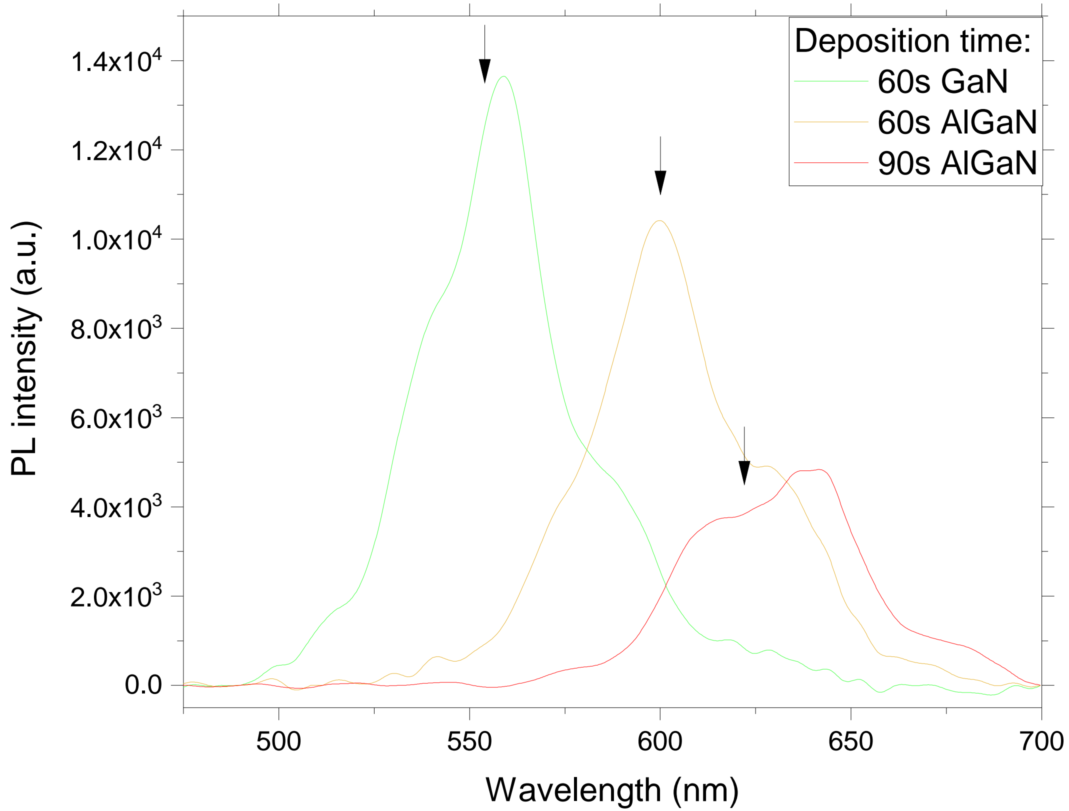

Figure 7.1: PL spectra of three samples with increasing capping layer thickness.

corresponds to a minimum of the reflectivity, which may explain why it does not correspond to a maximum of the PL spectrum. Moreover, if one considers the center of gravity of the PL peaks the agreement with the simulated transitions is extremely good for all the samples. Since the calculated emission wavelengths are based on the structural parameter obtained by XRD analysis, which are mediated on a macroscopic area, it is possible to conclude that the observed redshift does not depend on microscopic variations of indium or aluminum concentrations. Based on the discussion of chapter 6, it is therefore possible to identify the change in QCSE and spatial confinement of carriers as the main reasons for the observed emission redshift. It is now interesting to verify if the simulations are able to describe accurately also the change in emission intensity.

Figure 7.2 shows the comparison between the normalized integrated intensity of the measured PL spectra of figure 7.1 and the calculated optical matrix elements. The decrease in emission intensity predicted by the simulations is in agreement with the observations. However, the measured intensity is always larger compared to the calculated optical matrix elements. This shows that there might be some effect which increases the recombination efficiency which is not taken into account in the simulations. Based on the discussion of section 1.8 and on the literature, this effect may be identified as the compensation of the elastic energy in the structure. This conclusion is plausible since this effect is expected to improve the crystal quality of the QWs and as a consequence the emission intensity. However, based on the discussion of chapter 6, there might another explanation based on the interaction with defects. As discussed widely, the low growth temperature required for

this structures results in a low crystal quality. In particularly, the (Al)GaN capping layer is grown with TMGa under non-optimal conditions (see section 2.1.2). As a consequence, a large number of point defects is expected to be found in these layers. These defects are very effective recombination centers, reducing the number of carriers available to recombine radiatively in the QW.

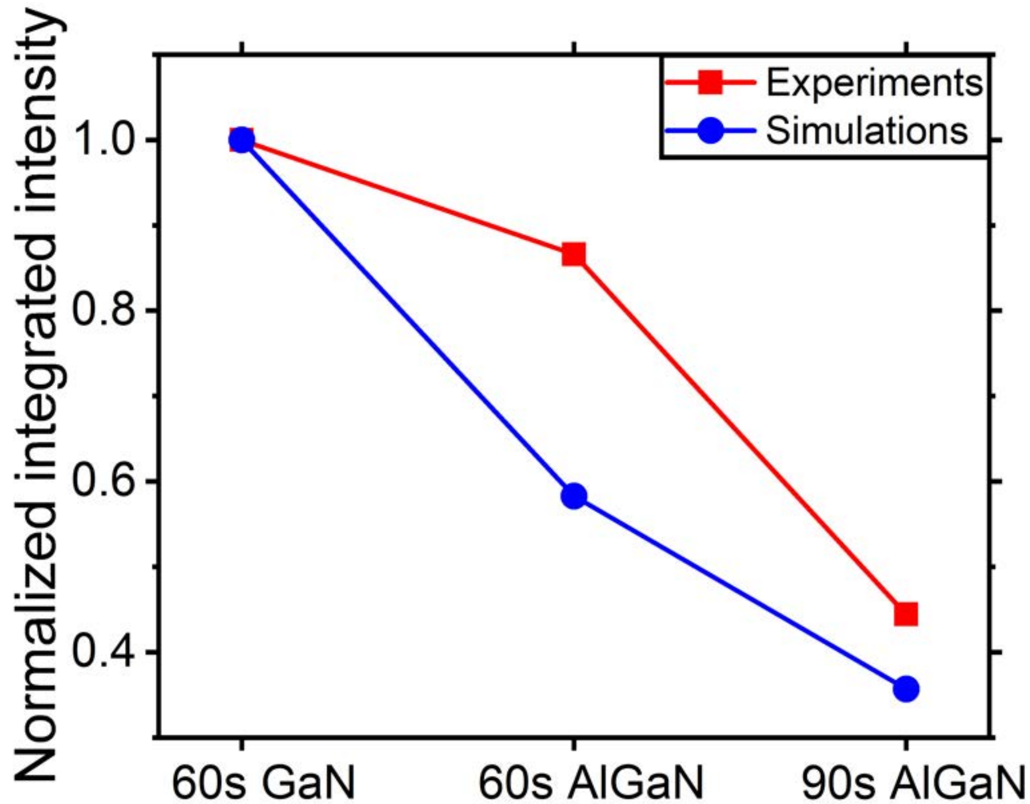

Figure 7.2: Comparison between the measured and simulated PL integrated intensity of the three samples of figure 7.1. It is possible to see that the experimental value is always more intense compared to the simulated one.

As can be seen from figure 6.4, one effect of the AlGaN capping layer is to push the electron wavefunction in the QW. As a consequence, the extension of the electron wavefunction in the barrier decreases with increasing Al content in the capping layer. This reduces the interaction probability of electrons with the point defects in the capping layer, reducing the carrier loss through competitive recombination channels and increasing the number of carriers recombining radiatively in the QW. In the case of the three samples of figure 7.1, the change in localization shows a different behavior as reported in table 7.1. To simplify the discussion, I will call the samples studied as GS (green sample), OS (orange sample) and RS (red sample) referring to the samples with a capping layer of 60 s GaN, 60 s AlGaN and 90 s AlGaN respectively. As can be seen, the behavior of the holes is analogous to what was presented in figure 6.4. On the other hand, the probability of finding an electron in the QW increases from sample GS to OS, but it decreases from OS to RS, remaining however larger than the one of GS. To help visualize and understand this behavior, in figure 7.3 are reported the band structure and the electron ground state wavefunction probablity density

of the GS, OS, RS. From the figure it is possible to see that the wavefunction shrinks with increasing AlGaN thickness, which is also confirmed by the FWHM data reported in table 7.1. However, even if it always decreases, the positions of the FWHM extremes shows a significantly different behavior. The left part of the electron wavefunction keeps on moving towards the right interface of the QW. On the other hand, the right part of the wavefunction initially moves inside the QW but for the RS it moves back towards the capping layer. Based on the analysis done in chapter 7, it is possible to identify the origin of this behavior in the combination of the QCSE and the potential barrier at the InGaN/AlGaN interface. The only difference between sample OS and RS is in the capping layer thickness. This results in a larger electric field in the QW and at the same time a decrease of the electric field in the capping layer. The increased field pushes the electron wavefunction towards the InGaN/AlGaN interface, which then extends more into the capping layer due to the low potential barrier. This explains the different results compared to the one reported in section 6.1.

Sample name	Electron wf in QW	Electron wf FWHM beginning / end (value)	Hole wf in QW	Hole wf FWHM beginning / end (value)
GS (60 s GaN)	0.784	7.31 / 8.66 (1.35)	0.823	5.62 / 4.94 (0.68)
OS (60 s AlGaN)	0.824	7.38 / 8.59 (1.21)	0.729	5.54 / 4.88 (0.66)
RS (90 s AlGaN)	0.805	7.42 / 8.61 (1.19)	0.666	5.51 / 4.85 (0.66)

Table 7.1: Probability of finding an electron or a hole in the quantum well and the FWHM of their ground state wavefunction probability density of the three samples studied.

This result can be also used to explain the data shown in figure 7.2, assuming a similar defect density in the capping layers of the three samples, probably originating from the low temperature growth using TMGa. The larger intensity observed experimentally for sample OS compared to the simulations is related to the reduced interaction of the electrons with the defects in the capping layer thanks to the larger confinement in the QW. A similar result is observed for sample RS, with however a much lower difference between simulation and experiment. As shown before, the probability of finding an electron in the barrier increases in sample RS compared to OS, resulting in a larger probability of interaction with defects. As a consequence, the intensity difference between simulations and experiments is lower compared to the OS sample. However, by looking at table 7.1, one may argue that with increasing AlGaN thickness the probability of finding a hole in the barrier increases. As a consequence, the probability of interacting with non-radiative defects is expected to increase. Although this is true, its effect is smaller compared to the electron case. First, the density of defects in the barrier is expected to be lower compared to the capping layer since the growth temperature is much higher.

The same effect can be used to explain the increased intensity of GaN/InGaN/AlGaN QWs compared to GaN/InGaN/GaN. Figure 7.4 is showing the PL intensity of a wide variety of GaN/InGaN/GaN and GaN/InGaN/AlGaN multi-QWs in which both compositions and thicknesses were changed. As can be seen, the PL intensity of the GaN/InGaN/GaN QWs decreases exponentially when moving towards longer wavelengths, which is typical for the green gap [125]. However, when an AlGaN capping layer is added on top of the QWs, the typical intensity drop of the green gap is shifted by 30-50 nm toward longer wavelengths. Interestingly, for wavelengths shorter than 560 nm the GaN/InGaN/GaN QWs seems to have higher PL intensities compared to GaN/InGaN/AlGaN QWs. This effect was already observed in other works (figure 2 in ref. [4] and figure 1 in ref. [42]), where it was not shown directly but it can be easily inferred from the reported data. However, in

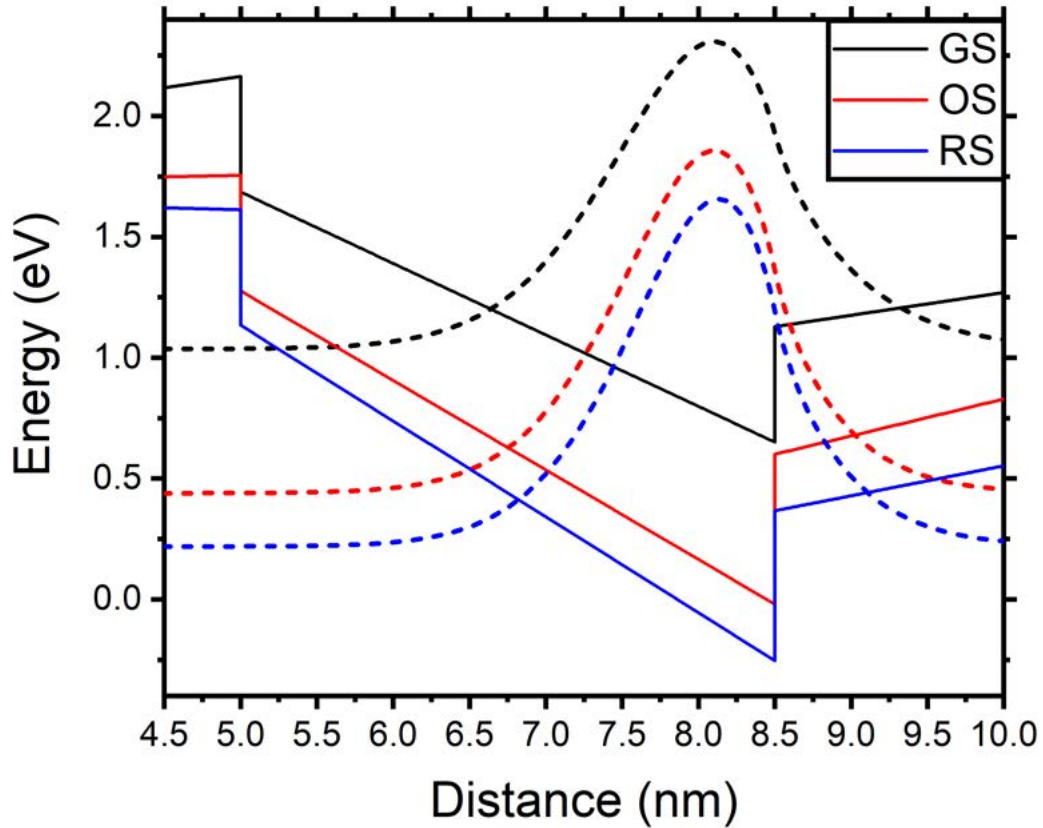

Figure 7.3: Calculated band structure (solid lines) of GS, OS and RS with their electron ground state wave-function probability density shown as dashed lines.

those cases the crossing occurs around 500-530 nm, thus at lower wavelengths compared to our case. The explanation proposed is analogous to the previous discussion and it is based on a trade-off between the increase of non-radiative defects and carrier confinement due to the AlGaN capping layer. The use of AlGaN as capping layer increases the polarization field in the QW, which in turn reduces the spatial extension of the wave function. Since the non-radiative lifetime steadily decreases with increasing wavelength [126, 127], at wavelengths longer than 560 nm the density of non-radiative defects of the sample is expected to be high [35]. Therefore reducing the spatial extension of the wavefunction reduces significantly the electron-hole interaction volume with the surrounding defects. On the other hand, a better crystal quality at shorter emission wavelengths is expected due to higher growth temperatures, making wave function separation due to QCSE the (negative) dominant effect. Since this effect depends mostly on point defects, we expect it to happen at longer wavelengths for samples with a lower point defect density (which is growth condition dependent). This explanation is in agreement with the recent work of David et al. [36], who identified the defect-assisted Auger recombination as the main reason for the efficiency droop. Indeed, reducing the interaction of carriers with defects can effectively mitigate the green gap by reducing SRH and defect-assisted non-radiative recombination even if the actual defect density is unchanged.

These results demonstrate that the electric field can have a positive effect on the emis-

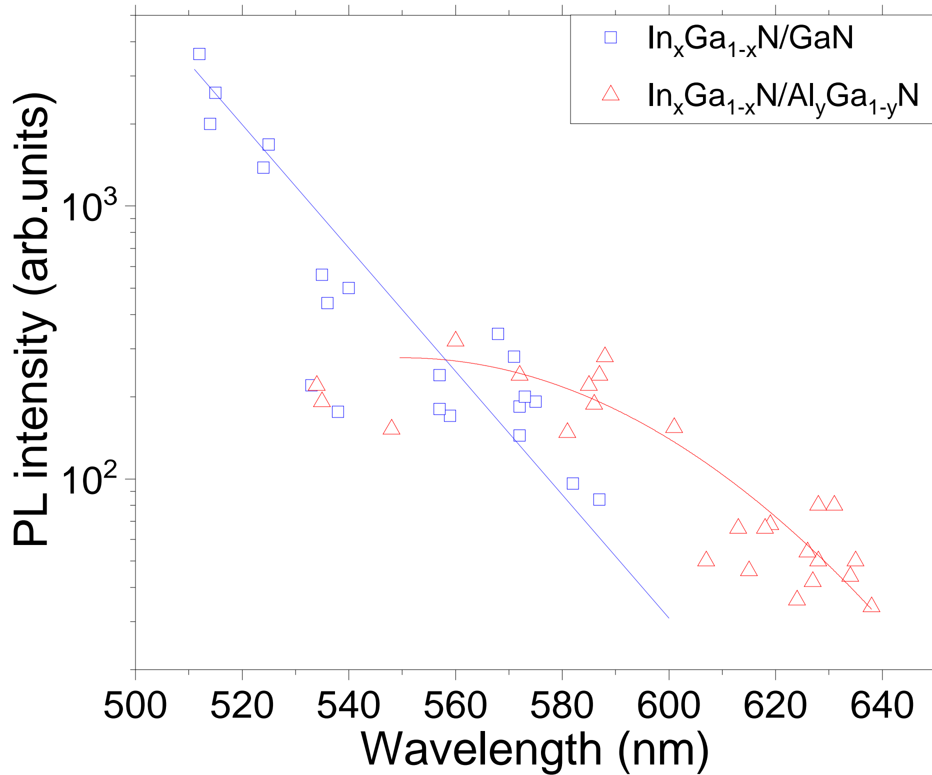

Figure 7.4: Room temperature photoluminescence intensity as a function of emission wavelength of the grown QWs with (△) and without (□) an AlGaN capping layer, in which both compositions and thicknesses were changed. The drop in intensity with AlGaN capping layer is clearly shifted by about 50 nm to longer wavelengths compared to GaN/InGaN/GaN QWs. From [123]

sion intensity, despite the common thinking. As demonstrated in chapter 6, there is indeed an increase of the optical matrix elements for certain AlGaN thicknesses and compositions. On top of that, it was discussed before that there might be also a second effect which increases the recombination efficiency and it is related to the reduction of the interaction probability of electrons with defects. This screening effect is also considered to explain the high efficiency of blue LEDs despite the large TD density. As discussed in chapter 1, the high electric field due to strain and composition changes close to the dislocations limits the interaction of carriers with the non-radiative centers. Surprisingly, a similar explanation was never considered when discussing the effect of the AlGaN capping layer.

7.2 Power and temperature analysis

Complementary information on the QW recombination properties can be obtained by measuring the PL spectrum as a function of the incident power and temperature. These measurements were conducted using a resonant laser with emission wavelength of 405 nm. Therefore, only the InGaN QWs are able to absorb the incident radiation and generate the e-h pairs. As a consequence, only the recombination processes taking place in the QW contribute to the emission spectrum, with a much simpler carrier dynamics compared to the

above-gap excitation.

In figure 7.5 are shown the PL spectra taken at 15 K of the sample RS for different incident powers. The peak wavelength is indicated by the black dots. It is immediately visible the blueshift of the emission wavelength with increasing power. This phenomenon is caused by the screening of the electric field due to the filling of the QW states. When an electron and a hole are located in the quantum well, they generate an electric dipole opposed to the existing electric field. As a consequence, the effect of the QCSE is reduced resulting in an increase of the confined energy levels. The screening effect is very important for LEDs, since the emission color changes depending on carrier injection.

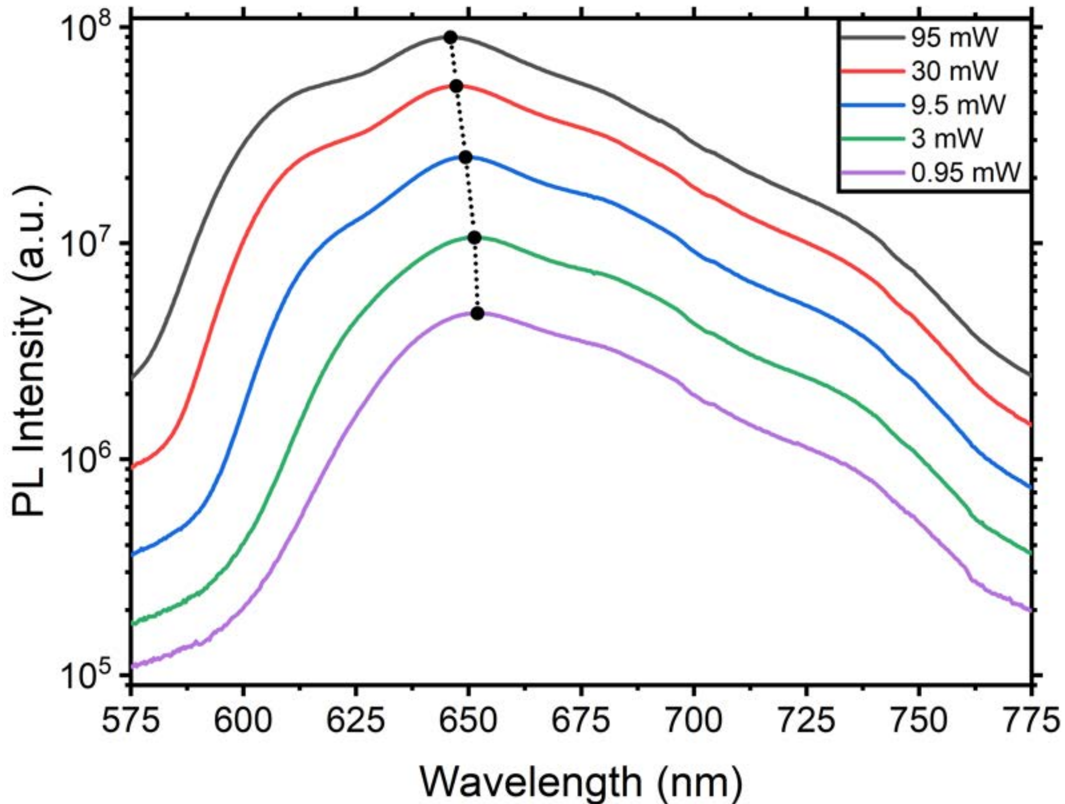

Figure 7.5: Photoluminescence spectra of sample RS for different incident powers taken at 15 K. The doted line connects the maxima of the PL spectra at different powers.

Figure 7.6 shows the photoluminesce peak energy of sample RS at different temperatures. As can be seen, the peak emission energy decreases from 15 K to 70 K, increases from 70 K to 150 K and finally decreases again above 150 K. The observed behavior, typically addressed as S-shape, was already reported in literature for GaN/InGaN/GaN QWs [14, 98, 128] but it was never shown for GaN/InGaN/AlGaN QWs. Since this phenomenon is typically observed in nitride-based QWs, it is believed that it originates from a combination of QCSE, screening of the electric field, potential fluctuations and carrier localization effects. The typical explanation is based on the redistribution of carriers with increasing temperature and in particular the blueshift of the emission energy is attributed to the increased population density of higher energy states [129, 130]. A more recent work by Langer et al. [98] suggested a competition between radiative and non-radiative processes

caused by a change in carrier lifetimes due to piezoelectric field. This proposal was supported by the much weaker S-shape observed in non-polar InGaN QWs, where there is no polarization field. The observation of the S-shape is consistent with literature results of InGaN/GaN QWs, which means that the AlGaN capping layer does not have a profound effect on the mechanisms involed in this phenomenon. However, the magnitude of the oscillation measured ($\sim$10 meV) is much lower compared to literature results [98] which could mean that the increased localization due to the larger electric field caused by the AlGaN layer may have an effect on the interaction of carriers with defects.

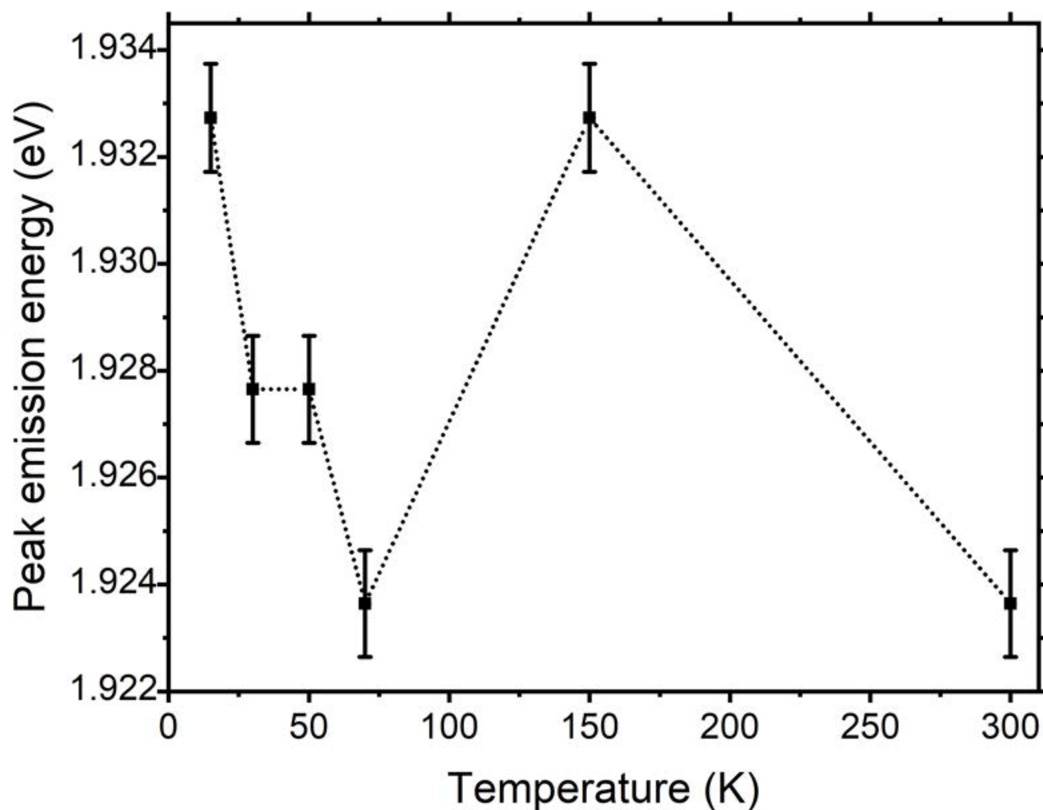

Figure 7.6: PL peak emission energy of sample RS as a function of temperature with an exitation power of 95 mW. It is visible the typical S-shape observed in InGaN/GaN QWs [98].

8 Conclusions and Future Prospects

In the initial part of this work I have grown by MOVPE and characterized several GaN/InGaN/(Al)GaN QWs in order to obtain a sample with red emission. For this purpose, I studied the effect of the different growth parameters on the structural and luminescence properties of the QWs to optimize the emission wavelength and line width. Even if the obtained QW emission met the requirements, the broad emission originating from defects in the barrier or capping layer made the color appear as dark orange rather than red. Since these defects are probably originated by the large carbon incorporation at low growth temperatures, it would be interesting as a future research to grow the same structures using MBE, which permits to reduce the carbon contamination. In addition to the MOVPE results, I reported in this work the preliminary optimization steps that I performed to grow the initial GaN buffer layer by MBE. This part of the work has to be considered as an initial feasibility study for the realization of long-wavelength LEDs by MBE, keeping as reference the results obtained in this work using MOVPE. If there will be an improvement, it would be interesting to investigate the possibility to combine the two growth techniques to realize an RGB all-nitrides-based emitter. At the same time, the quality of the MOVPE structure can be improved by growing the capping layer with TEGa to reduce carbon incorporation. This will require the optimization of the fluxes to avoid changing the TEGa flow between the QW and the capping layer.

The main part of this work was to improve the understanding of the effect of the AlGaN capping layer on the emission properties of GaN/InGaN/GaN QWs. I did this by combining the experimental data obtained with MOVPE and the theoretical simulations. The results showed that the AlGaN capping layer increases the emission wavelength due to the larger polarization field in the QW. Based on the literature, a larger QCSE is expected to reduce the emission intensity due to the larger wavefunction separation. However, it was observed an increase in emission intensity for the GaN/InGaN/AlGaN QWs compared to GaN/InGaN/GaN at the same wavelength. In the literature this result is typically related to the strain compensation effect of the AlGaN layer. In this work I proposed another explanation based on the increased confinement of electrons due to the larger potential barrier. This can increase the wavefunction overlap and reduce the interaction of electrons with point defects, resulting in an increased emission intensity. Understanding that the electric field

can be seen as an allied rather than as an enemy may open alternative paths to improve the efficiency of long-wavelength nitride-based LEDs.

List of Publications

- F. Basso Basset, S. Bietti, A. Tuktamyshev, S. Vichi, E. Bonera and S. Sanguinetti, ”Spectral broadening in self-assembled GaAs quantum dots with narrow size distribution”, *Journal of Applied Physics* **126**, 024301, 2019
- A. Ballabio, S. Bietti, A. Scaccabarozzi, L. Esposito, S. Vichi, A. Fedorov, A. Vinattieri, C. Mannucci, F. Biccari, A. Nemcsis, L. Toth, L. Miglio, M. Gurioli, G. Isella and S. Sanguinetti, ”GaAs epilayers grown on patterned (001) silicon substrates via suspended Ge layers”, *Scientific Reports* **9**, 17529, 2019
- S. Vichi, S. Bietti, A. Khalili, M. Costanzo, F. Cappelluti, L. Esposito, C. Somaschini, A. Fedorov, S. Tsukamoto, P. Rauter and S. Sanguinetti, ”Droplet epitaxy quantum dot based infrared photodetectors”, *Nanotechnology* **31**, 245203, 2020
- S. Vichi, Y. Robin, S. Sanguinetti, M. Pristovsek and H. Amano, ”Increasing the efficiency of long wavelengths InGaN quantum well structures by electric field engineering using AlGaN capping layer”, *Physical Review Applied* **14**, 024018, 2020

Bibliography

[1] M. Hocker, P. Maier, L. Jerg, I Tischer, G. Neusser, C. Kranz, M. Pristovsek, C. J. Humphreys, R. A. R. Leute, D. Heinz, O. Rettig, F. Scholz, and K. Thonke. Determination of axial and lateral exciton diffusion length in GaN by electron energy dependent cathodoluminescence. *Journal of Applied Physics*, 120(8), 2016.

[2] S. Saito, R. Hashimoto, J. Hwang, and S. Nunoue. InGaN light-emitting diodes on c-face sapphire substrates in green gap spectral range. *Applied Physics Express*, 6(11), 2013.

[3] B. Damilano and B. Gil. Yellow-red emission from (Ga,In)N heterostructures. *Journal of Physics D: Applied Physics*, 48(40):403001, 2015.

[4] T. Shioda, H. Yoshida, K. Tachibana, N. Sugiyama, and S. Nunoue. Enhanced light output power of green LEDs employing AlGaN interlayer in InGaN/GaN MQW structure on sapphire (0001) substrate. *Physica Status Solidi (A) Applications and Materials Science*, 209(3):473–476, 2012.

[5] D. Iida, S. Lu, S. Hirahara, K. Niwa, S. Kamiyama, and K. Ohkawa. Investigation of amber light-emitting diodes based on InGaN / AlN / AlGaN quantum wells. *Japanese Journal of Applied Physics*, 55:05FJ06, 2016.

[6] W. Paszkowicz. X-ray powder diffraction data for indium nitride. *Powder Diffraction*, 14(4):258–260, 1999.

[7] H. Angerer, D. Brunner, F. Freudenberg, O. Ambacher, M. Stutzmann, R. Höpler, T. Metzger, E. Born, G. Dollinger, A. Bergmaier, S. Karsch, and H. J. Körner. Determination of the Al mole fraction and the band gap bowing of epitaxial AlxGa1-xN films. *Applied Physics Letters*, 71(11):1504–1506, 1997.

[8] O. Ambacher. Thermal stability and desorption of Group III nitrides prepared by metal organic chemical vapor deposition. *Journal of Vacuum Science & Technology B: Microelectronics and Nanometer Structures*, 14(6):3532, 2002.

[9] A. E. Romanov, T. J. Baker, S. Nakamura, and J. S. Speck. Strain-induced polarization in wurtzite III-nitride semipolar layers. *Journal of Applied Physics*, 100(2), 2006.

[10] J. Wu, W. Walukiewicz, W. Shan, K. M. Yu, J. W. Ager, S. X. Li, E. E. Haller, Hai Lu, and William J. Schaff. Temperature dependence of the fundamental band gap of InN. *Journal of Applied Physics*, 94(7):4457–4460, 2003.

[11] L. F J Piper, T. D. Veal, C. F. McConville, Hai Lu, and W. J. Schaff. Origin of the n-type conductivity of InN: The role of positively charged dislocations. *Applied Physics Letters*, 88(25):1–4, 2006.

[12] I. Mahboob, T. D. Veal, C. F. McConville, H. Lu, and W. J. Schaff. Intrinsic Electron Accumulation at Clean InN Surfaces. *Physical Review Letters*, 92(3):4, 2004.

[13] J. Wu, W. Walukiewicz, S. X. Li, R. Armitage, J. C. Ho, E. R. Weber, E. E. Haller, Hai Lu, William J. Schaff, A. Barcz, and R. Jakiela. Effects of electron concentration on the optical absorption edge of InN. *Applied Physics Letters*, 84(15):2805–2807, 2004.

[14] S. Chichibu, T. Azuhata, T. Sota, and S. Nakamura. Spontaneous emission of localized excitons in InGaN single and multiquantum well structures. *Applied Physics Letters*, 69(27):4188–4190, 1996.

[15] Y. Narukawa, Y. Kawakami, M. Funato, S. Fujita, S. Fujita, and S. Nakamura. Role of self-formed InGaN quantum dots for exciton localization in the purple laser diode emitting at 420 nm. *Applied Physics Letters*, 70(8):981–983, 1997.

[16] L. Bellaiche, T. Mattila, L. W. Wang, S. H. Wei, and A. Zunger. Resonant hole localization and anomalous optical bowing in InGaN alloys. *Applied Physics Letters*, 74(13):1842–1844, 1999.

[17] H. Amano. Metalorganic vapor phase epitaxial growth of a high quality GaN film using an AlN buffer. 353(August):1–4, 1998.

[18] S.Nakamura. GaN Growth Using GaN Buffer Layer. *Japanese Journal of Applied Physics*, 30:L1705, 1991.

[19] K. Hiramatsu, S. Itoh, H. Amano, I. Akasaki, N. Kuwano, T. Shiraishi, and K. Oki. Growth mechanism of GaN grown on sapphire with A1N buffer layer by MOVPE. *Journal of Crystal Growth*, 115(1-4):628–633, 1991.

[20] J. Huang, H. Kuo, and S. Shen. *Nitride semiconductor light- emitting diodes (LEDs)*. Woodhead Publishing, 1st edition, 2014.

[21] J. K. Sheu, M. L. Lee, and W. C. Lai. Effect of low-temperature-grown GaN cap layer on reduced leakage current of GaN Schottky diodes. *Applied Physics Letters*, 86(5):1–3, 2005.

[22] M. A. Reshchikov and H. Morkoc. Luminescence properties of defects in GaN. 061301(January 2005), 2010.

[23] M. A. Reshchikov and R. Y. Korotkov. Analysis of the temperature and excitation intensity dependencies of photoluminescence in undoped gan films. *Physical Review B - Condensed Matter and Materials Physics*, 64(11):1152051–11520511, 2001.

[24] C. G. Van De Walle and J. Neugebauer. First-principles calculations for defects and impurities: Applications to III-nitrides. *Journal of Applied Physics*, 95(8):3851–3879, 2004.

[25] J. Neugebauer and C. G. Van de Walle. Gallium vacancies and the yellow luminescence in GaN. *Applied Physics Letters*, 69(4):503–505, 1996.

[26] T. Ogino and M. Aoki. Mechanism of Yellow Luminescence in GaN. *Japanese Journal of Applied Physics*, 19(12):2395–2405, 1980.

[27] H. C. Yang, T. Y. Lin, and Y. F. Chen. Nature of the 2.8-eV photoluminescence band in Si-doped GaN. *Physical Review B - Condensed Matter and Materials Physics*, 62(19):12593–12596, 2000.

[28] A. Addamiano. On the Preparation of the Nitrides of Aluminum and Gallium. *Journal of The Electrochemical Society*, 108(11):1072, 1961.

[29] M. R. Lorenz and B. B. Binkowski. Preparation, Stability, and Luminescence of Gallium Nitride. *Journal of The Electrochemical Society*, 109(1):24, 1962.

[30] H. Amano, M. Kito, K. Hiramatsu, and I. Akasaki. P-type conduction in Mg-doped GaN treated with low-energy electron beam irradiation (LEEBI). *Japanese Journal of Applied Physics*, 28(12 A):L2112–L2114, 1989.

[31] S. Nakamura, T. Mukai, M. Senoh, and N. Iwasa. Thermal annealing effects on P-type Mg-doped GaN films. *Japanese Journal of Applied Physics*, 31(2):139–142, 1992.

[32] S. Nakamura, N. Iwasa, M. Senoh, and T. Mukai. Hole Compensation Mechanism of P-Type GaN Films. *Japanese Journal of Applied Physics*, 31(5 R):1258–1266, 1992.

[33] D. S.P. Tanner, P. Dawson, M. J. Kappers, R. A. Oliver, and S. Schulz. Polar (In, Ga) N / Ga N Quantum Wells: Revisiting the Impact of Carrier Localization on the "green Gap" Problem. *Physical Review Applied*, 13(4):1, 2020.

[34] M. Auf Der Maur, A. Pecchia, G. Penazzi, W. Rodrigues, and A. Di Carlo. Efficiency Drop in Green InGaN/GaN Light Emitting Diodes: The Role of Random Alloy Fluctuations. *Physical Review Letters*, 116(2):1–5, 2016.

[35] S. Hammersley, M. J. Kappers, F. C.P. Massabuau, S. L. Sahonta, P. Dawson, R. A. Oliver, and C. J. Humphreys. Effects of quantum well growth temperature on the recombination efficiency of InGaN/GaN multiple quantum wells that emit in the green and blue spectral regions. *Applied Physics Letters*, 107(13), 2015.

[36] A. David, N. G. Young, C.e A. Hurni, and M. D. Craven. Quantum Efficiency of III-Nitride Emitters: Evidence for Defect-Assisted Nonradiative Recombination and its Effect on the Green Gap. *Physical Review Applied*, 11(3):1–6, 2019.

[37] M. Meneghini, C. De Santi, A. Tibaldi, M. Vallone, F. Bertazzi, G. Meneghesso, E. Zanoni, and M. Goano. Thermal droop in III-nitride based light-emitting diodes: Physical origin and perspectives. *Journal of Applied Physics*, 127(21):211102, 2020.

[38] C. Haller, J. F. Carlin, G. Jacopin, D. Martin, R. Butté, and N. Grandjean. Burying non-radiative defects in InGaN underlayer to increase InGaN/GaN quantum well efficiency. *Applied Physics Letters*, 111(26), 2017.

[39] C. Haller, J. F. Carlin, G. Jacopin, W. Liu, D. Martin, R. Butté, and N. Grandjean. GaN surface as the source of non-radiative defects in InGaN/GaN quantum wells. *Applied Physics Letters*, 113(11):1–5, 2018.

[40] D. D. Koleske, A. E. Wickenden, R. L. Henry, J. C. Culbertson, and M. E. Twigg. GaN decomposition in H2 and N2 at MOVPE temperatures and pressures. *Journal of Crystal Growth*, 223(4):466–483, 2001.

[41] A. Uedono, T. Watanabe, S. Kimura, Y. Zhang, M. Lozac'H, L. Sang, S. Ishibashi, N. Oshima, R. Suzuki, and M. Sumiya. Vacancy-type defects in InxGa1-xN grown on GaN templates probed using monoenergetic positron beams. *Journal of Applied Physics*, 114(18), 2013.

[42] D. D. Koleske, A. J. Fischer, B. N. Bryant, P. G. Kotula, and J. J. Wierer. On the increased efficiency in InGaN-based multiple quantum wells emitting at 530-590 nm with AlGaN interlayers. *Journal of Crystal Growth*, 415:57–64, 2015.

[43] J. Il Hwang, R. Hashimoto, S. Saito, and S. Nunoue. Development of InGaN-based red LED grown on (0001) polar surface. *Applied Physics Express*, 7(7), 2014.

[44] H. Zhao, R. A. Arif, Y. K. Ee, and N. Tansu. Self-consistent analysis of strain-compensated InGaN-AlGaN quantum wells for lasers and light-emitting diodes. *IEEE Journal of Quantum Electronics*, 45(1):66–78, 2009.

[45] H. M. Manasevit, F. M. Erdmann, and W. I. Simpson. The Use of Metalorganics in the Preparation of Semiconductor Materials: IV. The Nitrides of Aluminum and Gallium. *Journal of the Electrochemical Society*, 118(11):1864–1868, 1969.

[46] D. J. Kim, Y. T. Moon, K. M. Song, I. H. Lee, and S. Ju. Park. Effect of growth pressure on indium incorporation during the growth of InGaN by MOCVD. *Journal of Electronic Materials*, 30(2):99–102, 2001.

[47] J. R. Chen, S. C. Ling, H. M. Huang, P. Y. Su, T. S. Ko, T. C. Lu, H. C. Kuo, Y. K. Kuo, and S. C. Wang. Numerical study of optical properties of InGaN multi-quantum-well laser diodes with polarization-matched AlInGaN barrier layers. *Applied Physics B: Lasers and Optics*, 95(1):145–153, 2009.

[48] J. Randall Creighton, George T. Wang, William G. Breiland, and Michael E. Coltrin. Nature of the parasitic chemistry during AlGaInN OMVPE. *Journal of Crystal Growth*, 261(2-3):204–213, 2004.

[49] A. V. Kondratyev, R. A. Talalaev, W. V. Lundin, A. V. Sakharov, A. V. Tsatsul'nikov, E. E. Zavarin, A. V. Fomin, and D. S. Sizov. Aluminum incorporation control in AlGaN MOVPE: Experimental and modeling study. *Journal of Crystal Growth*, 272(1-4 SPEC. ISS.):420–425, 2004.

[50] A. V. Lobanova, K. M. Mazaev, R. A. Talalaev, M. Leys, S. Boeykens, K. Cheng, and S. Degroote. Effect of V/III ratio in AlN and AlGaN MOVPE. *Journal of Crystal Growth*, 287(2):601–604, 2006.

[51] W. C. Huang, Y. Y. Wong, K. S. Liu, C. F. Hsieh, and E. Y. Chang. The parasitic reaction during the MOCVD growth of AlInN material. *2012 10th IEEE International Conference on Semiconductor Electronics, ICSE 2012 - Proceedings*, pages 766–768, 2012.

[52] S. C. Cruz, S. Keller, T. E. Mates, U. K. Mishra, and S. P. DenBaars. Crystallographic orientation dependence of dopant and impurity incorporation in GaN films grown by metalorganic chemical vapor deposition. *Journal of Crystal Growth*, 311(15):3817–3823, 2009.

[53] A. Armstrong, A. R. Arehart, B. Moran, S. P. DenBaars, U. K. Mishra, J. S. Speck, and S. A. Ringel. Impact of carbon on trap states in n-type GaN grown by metalorganic chemical vapor deposition. *Applied Physics Letters*, 84(3):374–376, 2004.

[54] K. Seshan. *Handbook of Thin Film Deposition Techniques Principles, Methods, Equipment and Applications, Second Editon*. 2002.

[55] C. H. Chen, H. Liu, D. Steigerwald, W. Imler, C. P. Kuo, M. G. Craford, M. Ludowise, S. Lester, and J. Amano. A study of parasitic reactions between NH3and TMGa or TMAl. *Journal of Electronic Materials*, 25(6):1004–1008, 1996.

[56] D. G. Zhao, Z. S. Liu, J. J. Zhu, S. M. Zhang, D. S. Jiang, Hui Yang, J. W. Liang, X. Y. Li, and H. M. Gong. Effect of Al incorporation on the AlGaN growth by metalorganic chemical vapor deposition. *Applied Surface Science*, 253(5):2452–2455, 2006.

[57] T. G. Mihopoulos, V. Gupta, and K. F. Jensen. A reaction-transport model for AlGaN MOVPE growth. *Journal of Crystal Growth*, 195(1-4):733–739, 1998.

[58] H. Morkoç. *Nitride Semiconductor Devices : Principles and Simulation Properties of Group-IV , III-V and II-VI Semiconductors Nitride Semiconductors*. 2008.

[59] Q. Bao, T. Zhu, N. Zhou, S. Guo, J. Luo, and C. Zhao. Effect of hydrogen carrier gas on AlN and AlGaN growth in AMEC Prismo D-Blue® MOCVD platform. *Journal of Crystal Growth*, 419:52–56, 2015.

[60] Y. Guo, X. L. Liu, H. P. Song, A. L. Yang, X. Q. Xu, G. L. Zheng, H. Y. Wei, S. Y. Yang, Q. S. Zhu, and Z. G. Wang. A study of indium incorporation in In-rich InGaN grown by MOVPE. *Applied Surface Science*, 256(10):3352–3356, 2010.

[61] G. B Stringfellow. *Organometallic Vapor-Phase Epitaxy: Theory and Practice*. Academic Press, 2nd edition, 1999.

[62] C. A. Larsen, N.I. Buchan, S. H. Li, and G. B. Stringfellow. Decomposition mechanisms of trimethylarsine. *Journal of Crystal Growth*, 102(1-2):117–125, 1990.

[63] Ö. Danielsson, X. Li, L. Ojamäe, E. Janzén, H. Pedersen, and U. Forsberg. A model for carbon incorporation from trimethyl gallium in chemical vapor deposition of gallium nitride. *Journal of Materials Chemistry C*, 4(4):863–871, 2016.

[64] M. Tsuda, S. Oikawa, M. Morishita, and M. Mashita. On the Reaction Mechanism of the Pyrolyses of TMG and TEG in MOCVD Growth Reactors. *Japanese Journal of Applied Physics*, 26(5A):L564, 1987.

[65] G. B. Stringfellow. Novel precursors for organometallic vapor phase epitaxy. *Journal of Crystal Growth*, 128(1-4):503–510, 1993.

[66] J. S. Park, Z. J. Reitmeier, and R. F. Davis. Comparison of the microstructure and chemistry of GaN(0001) films grown using trimethylgallium and triethylgallium on AIN/SiC substrates. *Physica Status Solidi C: Conferences*, 2(7):2166–2169, 2005.

[67] A. Ishibashi, H. Takeishi, M. Mannoh, Y. Yabuuchi, and Y. Ban. Residual impurities in GaN/Al2O3 grown by metalorganic vapor phase epitaxy. *Journal of Electronic Materials*, 25(5):799–803, 1996.

[68] D. D. Koleske, A. E. Wickenden, R. L. Henry, and M. E. Twigg. Influence of MOVPE growth conditions on carbon and silicon concentrations in GaN. *Journal of Crystal Growth*, 242(1-2):55–69, 2002.

[69] S. Nakamura, T. Mukai, and M. Senoh. Si- and Ge-Doped GaN Films Grown with GaN Buffer Layers. *Japanese Journal of Applied Physics*, 31(9 R):2883–2888, 1992.

[70] W. Götz, N. M. Johnson, J. Walker, D. P. Bour, and R. A. Street. Activation of acceptors in Mg-doped GaN grown by metalorganic chemical vapor deposition. *Applied Physics Letters*, 667(November 1995):667, 1995.

[71] H. Murakami, T. Asahi, H. Amano, K. Hiramatsu, N. Sawaki, and I. Akasaki. Growth of Si-doped AlxGa1-xN on (0001) sapphire substrate by metalorganic vapor phase epitaxy. *Journal of Crystal Growth*, 115(1-4):648–651, 1991.

[72] S. Fritze, A. Dadgar, H. Witte, M. Bügler, A. Rohrbeck, J. Bläsing, A. Hoffmann, and A. Krost. High Si and Ge n-type doping of GaN doping - Limits and impact on stress. *Applied Physics Letters*, 100(12), 2012.

[73] D. J. Kim, D. Y. Ryu, N. A. Bojarczuk, J. Karasinski, S. Guha, S. H. Lee, and J. H. Lee. Thermal activation energies of Mg in GaN:Mg measured by the Hall effect and admittance spectroscopy. *Journal of Applied Physics*, 88(5):2564–2569, 2000.

[74] H. Obloh, K. H. Bachem, U. Kaufmann, M. Kunzer, M. Maier, A. Ramakrishnan, and P. Schlotter. Self-compensation in Mg doped p-type GaN grown by MOCVD. *Journal of Crystal Growth*, 195(1-4):270–273, 1998.

[75] G. Miceli and A. Pasquarello. Self-compensation due to point defects in Mg-doped GaN. *Physical Review B*, 93(16):1–11, 2016.

[76] W. Götz, N. M. Johnson, J. Walker, D. P. Bour, H. Amano, and I. Akasaki. Hydrogen passivation of Mg acceptors in GaN grown by metalorganic chemical vapor deposition. *Applied Physics Letters*, 67(August 1995):2666, 1995.

[77] S. Nakamura, M. Senoh, and T. Mukai. Highly p-typed mg-doped gan films grown with gan buffer layers. *Japanese Journal of Applied Physics*, 30(10A):L1708–L1711, 1991.

[78] A. Koukitu, T. Taki, N. Takahashi, and H. Seki. Thermodynamic study on the role of hydrogen during the MOVPE growth of group III nitrides. *Journal of Crystal Growth*, 197(1-2):99–105, 1999.

[79] E. L. Piner, M. K. Behbehani, N. A. El-Masry, F. G. McIntosh, J. C. Roberts, K. S. Boutros, and S. M. Bedair. Effect of hydrogen on the indium incorporation in InGaN epitaxial films. *Applied Physics Letters*, 70(4):461–463, jan 1997.

[80] M. Bosi and R. Fornari. A study of Indium incorporation efficiency in InGaN grown by MOVPE. *Journal of Crystal Growth*, 265(3-4):434–439, 2004.

[81] R. Czernecki, S. Kret, P. Kempisty, E. Grzanka, J. Plesiewicz, G. Targowski, S. Grzanka, M. Bilska, J. Smalc-Koziorowska, S. Krukowski, T. Suski, P. Perlin, and M. Leszczynski. Influence of hydrogen and TMIn on indium incorporation in MOVPE growth of InGaN layers. *Journal of Crystal Growth*, 402:330–336, 2014.

[82] H. Morkoç. *Nitride Semiconductor Devices : Principles and Simulation Properties of Group-IV , III-V and II-VI Semiconductors Nitride Semiconductors*. 2008.

[83] I. Hsiu Ho and G. B. Stringfellow. Solid phase immiscibility in GaInN. *Applied Physics Letters*, 69(18):2701–2703, 1996.

[84] S. Y. Karpov. Suppression of phase separation in InGaN due to elastic strain. *MRS Internet Journal of Nitride Semiconductor Research*, 3(January 1998):e16, jun 1998.

[85] L. Teles, J. Furthmüller, L. Scolfaro, J. Leite, and F. Bechstedt. First-principles calculations of the thermodynamic and structural properties of strained and alloys. *Physical Review B - Condensed Matter and Materials Physics*, 62(4):2475–2485, 2000.

[86] F. C. P. Massabuau, M. J. Davies, W. E. Blenkhorn, S. Hammersley, M. J. Kappers, C. J. Humphreys, P. Dawson, and R. A. Oliver. Investigation of unintentional indium incorporation into GaN barriers of InGaN/GaN quantum well structures. *Physica Status Solidi (B) Basic Research*, 252(5):928–935, 2015.

[87] S. Freytag, M. Feneberg, C. Berger, J. Bläsing, A. Dadgar, G. Callsen, F. Nippert, A. Hoffmann, P. Y. Bokov, and R. Goldhahn. Unintentional indium incorporation into barriers of InGaN/GaN multiple quantum wells studied by photoreflectance and photoluminescence excitation spectroscopy. *Journal of Applied Physics*, 120(1), 2016.

[88] V. Potin, E. Hahn, A. Rosenauer, D. Gerthsen, B. Kuhn, F. Scholz, A. Dussaigne, B. Damilano, and N. Grandjean. Comparison of the In distribution in InGaN/GaN quantum well structures grown by molecular beam epitaxy and metalorganic vapor phase epitaxy. *Journal of Crystal Growth*, 262(1-4):145–150, 2004.

[89] K. Muraki, S. Fukatsu, Y. Shiraki, and R. Ito. Surface segregation of in atoms during molecular beam epitaxy and its influence on the energy levels in InGaAs/GaAs quantum wells. *Applied Physics Letters*, 61(5):557–559, 1992.

[90] J. R. Arthur and J. J. LePore. GaAs, GaP, and GaAsxP1âˆ'x Epitaxial Films Grown by Molecular Beam Deposition. *Journal of Vacuum Science and Technology*, 6(4):545–548, jul 1969.

[91] H. Conrads and M. Schmidt. Plasma generation and plasma sources. *Plasma Sources Science and Technology*, 9(4):441–454, 2000.

[92] B. M. McSkimming, F. Wu, T. Huault, C. Chaix, and J. S. Speck. Plasma assisted molecular beam epitaxy of GaN with growth rates >2.6 μm/h. *Journal of Crystal Growth*, 386(December 2017):168–174, 2014.

[93] J. Neugebauer, T. K. Zywietz, M. Scheffler, J. E. Northrup, H. Chen, and R. M. Feenstra. Adatom Kinetics On and Below the Surface: The Existence of a New Diffusion Channel. *Physical Review Letters*, 90(5):4, 2003.

[94] E. J. Tarsa, B. Heying, X. H. Wu, P. Fini, S. P. DenBaars, and J. S. Speck. Homoepitaxial growth of GaN under Ga-stable and N-stable conditions by plasma-assisted molecular beam epitaxy. *Journal of Applied Physics*, 82(11):5472–5479, 1997.

[95] G. Koblmüller, F. Wu, T. Mates, J. S. Speck, S. Fernández-Garrido, and E. Calleja. High electron mobility GaN grown under N-rich conditions by plasma-assisted molecular beam epitaxy. *Applied Physics Letters*, 91(22):5–8, 2007.

[96] B. M. McSkimming, C. Chaix, and J. S. Speck. High active nitrogen flux growth of GaN by plasma assisted molecular beam epitaxy. *Journal of Vacuum Science & Technology A: Vacuum, Surfaces, and Films*, 33(5):05E128, 2015.

[97] S. G. Tomlin. Optical reflection and transmission formulae for thin films. *Journal of Physics D: Applied Physics*, 1(12):1667–1671, 1968.

[98] T. Langer, H. G. Pietscher, F. A. Ketzer, H. Jönen, H. Bremers, U. Rossow, D. Menzel, and A. Hangleiter. S shape in polar GaInN/GaN quantum wells: Piezoelectric-field-induced blue shift driven by onset of nonradiative recombination. *Physical Review B - Condensed Matter and Materials Physics*, 90(20):1–9, 2014.

[99] M. A. Moram and M. E. Vickers. X-ray diffraction of III-nitrides. *Reports on Progress in Physics*, 72(3), 2009.

[100] T. M. Smeeton, M. J. Kappers, J. S. Barnard, M. E. Vickers, and C. J. Humphreys. Analysis of InGaN/GaN single quantum wells by X-ray scattering and transmission electron microscopy. *Physica Status Solidi (B) Basic Research*, 240(2):297–300, 2003.

[101] A. Krost, J. Bläsing, M. Lünenbürger, H. Protzmann, and M. Heuken. Evaluation of strain and In content in (InGaN/GaN) multiquantum wells by X-ray analysis. *Applied Physics Letters*, 75(5):689–691, 1999.

[102] M. E. Vickers, M. J. Kappers, T. M. Smeeton, E. J. Thrush, J. S. Barnard, and C. J. Humphreys. Determination of the indium content and layer thicknesses in InGaN/GaN quantum wells by x-ray scattering. *Journal of Applied Physics*, 94(3):1565–1574, 2003.

[103] See www.tiberlab.com for TiberCAD software.

[104] M. Povolotskyi and A. Di Carlo. Elasticity theory of pseudomorphic heterostructures grown on substrates of arbitrary thickness. *Journal of Applied Physics*, 100(6), 2006.

[105] F. Bernardini, V. Fiorentini, and D. Vanderbilt. Spontaneous polarization and piezoelectric constants of III-V nitrides. *Physical Review B - Condensed Matter and Materials Physics*, 56(16):R10024–R10027, 1997.

[106] P. Harrison and A. Valavanis. *Quantum Wells, Wires and Dots*. Wiley, 4th edition, 2016.

[107] I. Vurgaftman and J. R. Meyer. Band parameters for nitrogen-containing semiconductors. *Journal of Applied Physics*, 94(6):3675–3696, 2003.

[108] C. E. Dreyer, A. Janotti, C. G. Van de Walle, and D. Vanderbilt. Correct implementation of polarization constants in wurtzite materials and impact on III-nitrides. *Physical Review X*, 6(2):1–11, 2016.

[109] Y. H. Li, A. Walsh, S. Chen, W. J. Yin, J. H. Yang, J. Li, J. L.F. Da Silva, X. G. Gong, and S. H. Wei. Revised ab initio natural band offsets of all group IV, II-VI, and III-V semiconductors. *Applied Physics Letters*, 94(21):1–4, 2009.

[110] R. R. Pelá, C. Caetano, M. Marques, L. G. Ferreira, J. Furthmüller, and L. K. Teles. Accurate band gaps of AlGaN, InGaN, and AlInN alloys calculations based on LDA-1/2 approach. *Applied Physics Letters*, 98(15), 2011.

[111] P. G. Moses, M. Miao, Q. Yan, and C. G. Van De Walle. Hybrid functional investigations of band gaps and band alignments for AlN, GaN, InN, and InGaN. *Journal of Chemical Physics*, 134(8), 2011.

[112] R. E. Jones, R. Broesler, K. M. Yu, J. W. Ager, E. E. Haller, W. Walukiewicz, X. Chen, and W. J. Schaff. Band gap bowing parameter of In1-xAlxN. *Journal of Applied Physics*, 104(12), 2008.

[113] I. Vurgaftman, J. R. Meyer, and L. R. Ram-Mohan. Band parameters for III-V compound semiconductors and their alloys. *Journal of Applied Physics*, 89(11 I):5815–5875, 2001.

[114] K. Ohkawa, T. Watanabe, M. Sakamoto, A. Hirako, and M. Deura. 740-nm emission from InGaN-based LEDs on c-plane sapphire substrates by MOVPE. *Journal of Crystal Growth*, 343(1):13–16, 2012.

[115] E. V. Yakovlev, A. S. Segal, K. A. Bulashevich, S. Y. Karpov, and R. A. Talalaev Ã. Correlations between Epitaxy Recipe , Characteristics , and Performance of Nitride Light Emitting Diode Structures Correlations between Epitaxy Recipe , Characteristics , and Performance of Nitride Light Emitting Diode Structures. 15:13–16, 2013.

[116] T. L. Tsai, C. S. Chang, T. P. Chen, and K. H. Huang. Effect of barrier thickness and barrier doping on the properties of InGaN/GaN multiple-quantum-well structure light emitting diode. *Physica Status Solidi C: Conferences*, 266(1):263–266, 2002.

[117] G. B. Lin, D. Y. Kim, Q. Shan, J. Cho, E. F. Schubert, H. Shim, C. Sone, and J. K. Kim. Effect of quantum barrier thickness in the multiple-quantum-well active region of GaInN/GaN light-emitting diodes. *IEEE Photonics Journal*, 5(4):1600207, 2013.

[118] H. M. Lu and G. X. Chen. Design strategies for mitigating the influence of polarization effects on GaN-based multiple quantum well light-emitting diodes. *Journal of Applied Physics*, 109(9), 2011.

[119] W. W. de Abney. On the change in hue of spectrum colours by dilution with white light. *Proceedings of the Royal Society of London. Series A, Containing Papers of a Mathematical and Physical Character*, 83(560):120–127, 1909.

[120] Y. Mizokami, J. S. Werner, M. A. Crognale, and M. A. Webster. Nonlinearities in color coding: Compensating color appearance for the eye's spectral sensitivity. *Journal of Vision*, 6(9):996–1007, 2006.

[121] T. Mukai, M. Yamada, and S. Nakamura. Characteristics of InGaN-based UV/blue/green/amber/red light-emitting diodes. *Japanese Journal of Applied Physics, Part 1: Regular Papers and Short Notes and Review Papers*, 38(7 B):3976–3981, 1999.

[122] N. A.K. Kaufmann, L. Lahourcade, B. Hourahine, D. Martin, and N. Grandjean. Critical impact of Ehrlich-Schwöbel barrier on GaN surface morphology during homoepitaxial growth. *Journal of Crystal Growth*, 433:36–42, 2016.

[123] S. Vichi, Y. Robin, S. Sanguinetti, M. Pristovsek, and H. Amano. Increasing the efficiency of long wavelengths InGaN LEDs by electric field engineering using AlGaN capping layer In G a N / A lG a N. *Physical Review Applied*, 10(1):1–5, 2020.

[124] W. Sun, S. A. Al Muyeed, R. Song, J. J. Wierer, and N. Tansu. Integrating AlInN interlayers into InGaN/GaN multiple quantum wells for enhanced green emission. *Applied Physics Letters*, 112(20), 2018.

[125] M. H. Crawford. LEDs for solid-state lighting: Performance challenges and recent advances. *IEEE Journal on Selected Topics in Quantum Electronics*, 15(4):1028–1040, 2009.

[126] M. Pristovsek, A. Bao, R. A. Oliver, T. Badcock, M. Ali, and A. Shields. Effects of Wavelength and Defect Density on the Efficiency of (In,Ga)N-Based Light-Emitting Diodes. *Physical Review Applied*, 7(6):1–10, 2017.

[127] T. Langer, H. Jönen, A. Kruse, H. Bremers, U. Rossow, and A. Hangleiter. Strain-induced defects as nonradiative recombination centers in green-emitting GaInN/GaN quantum well structures. *Applied Physics Letters*, 103(2), 2013.

[128] C. Netzel, V. Hoffmann, T. Wernicke, A. Knauer, M. Weyers, M. Kneissl, and N. Szabo. Temperature and excitation power dependent photoluminescence intensity of GaInN quantum wells with varying charge carrier wave function overlap. *Journal of Applied Physics*, 107(3), 2010.

[129] P. G. Eliseev, P. Perlin, J. Lee, and M. Osiński. Blue temperature-induced shift and band-tail emission in InGaN-based light sources. *Applied Physics Letters*, 71(5):569–571, 1997.

[130] P. G. Eliseev. The red $\sigma 2/kT$ spectral shift in partially disordered semiconductors. *Journal of Applied Physics*, 93(9):5404–5415, 2003.